

UNIVERSITÄT ULM, INSTITUT FÜR ANATOMIE UND
ZELLBIOLOGIE

ÄRZTLICHER DIREKTOR: PROF. DR. TOBIAS BÖCKERS

„Investigation of synaptic ultrastructure in
ProSAP/Shank mutant mice“

Dissertation zur Erlangung des Doktorgrades
der Medizin der Medizinischen Fakultät
der Universität Ulm

Constantin Mett

Bad Saulgau

2015

Amtierender Dekan: Prof. Dr. T. Wirth

1. Berichterstatter: Prof. Dr. T. Böckers

2. Berichterstatter: apl. Prof. Dr. C. von Arnim

Tag der Promotion: 15.12.2016

To my family

“The more one finds out about properties of different synapses, the less grows one's inclination to make general statements about their mode of action!”

Bernard Katz, 1966

Table of content

TABLE OF CONTENT	I
ABBREVIATIONS	III
1. INTRODUCTION	1
1.1 AUTISM SPECTRUM DISORDERS – ASD	1
1.1.1 OVERVIEW	1
1.1.2 SYNDROMIC FORMS OF ASD	3
1.1.2.1 Fragile X syndrome	3
1.1.2.2 Rett syndrome	4
1.1.2.3 Phelan-McDermid syndrome	4
1.2 THE SYNAPSE	6
1.2.1 OVERVIEW	6
1.2.2 ELECTRON MICROSCOPIC VIEW ON THE SYNAPSE	9
1.2.3 MORPHOLOGY OF DENDRITIC SPINES	11
1.3 THE POSTSYNAPTIC DENSITY	12
1.4 THE PROSAP/SHANK FAMILY	14
1.4.1 OVERVIEW	14
1.4.2 SHANK MUTANT MICE	17
1.4.2.1 Shank1 mutant mice	17
1.4.2.2 Shank2 mutant mice	18
1.4.2.3 Shank3 mutant mice	19
1.5 GOALS OF THIS WORK	21
2. MATERIAL AND METHODS	22
2.1 MATERIAL	22
2.1.1 CHEMICALS	22
2.1.2 ANALYSED MOUSE STRAINS	22
2.1.3 INVESTIGATED MICE	23
2.1.5 EQUIPMENT	24
2.1.6 SOFTWARE	24
2.2. METHODS	25
2.2.1 TISSUE PREPARATION	25
2.2.2 ELECTRON MICROSCOPY	26
2.2.3 STATISTICAL ANALYSIS	27
2.2.4 ANALYSED BRAIN REGIONS	28
2.2.4.1 Striatum	28
2.2.4.2 Hippocampus CA1	30
2.2.4.3 Hippocampus CA3	31
2.2.4.4 Molecular and granular layer of the cerebellum	33

3. RESULTS	35
3.1 PSD ULTRASTRUCTURE IN DISTINCT BRAIN REGIONS OF <i>ProSAP1/Shank2</i> AND <i>ProSAP2/Shank3</i> DOUBLE-KNOCKOUT MICE COMPARED TO WILD-TYPE LITTERMATE CONTROLS	35
3.1.1 DORSOMEDIAL STRIATUM	35
3.1.1.1 Pooled sexes	35
3.1.1.2 Male and female DKO mice compared to WT mice	38
3.1.2 DORSOLATERAL STRIATUM	40
3.1.2.1 Pooled sexes	40
3.1.2.2 Male and female DKO mice compared to WT mice	43
3.1.3 HIPPOCAMPUS CA1	45
3.1.3.1 Pooled sexes	45
3.1.3.2 Male and female DKO mice compared to WT mice	48
3.1.4 HIPPOCAMPUS CA3	50
3.1.4.1 Pooled sexes	50
3.1.4.2 Male and female DKO mice compared to WT mice	53
3.1.5 MOLECULAR LAYER CEREBELLUM	55
3.1.5.1 Pooled sexes	55
3.1.5.2 Male and female DKO mice compared to WT mice	58
3.1.6 GRANULAR LAYER CEREBELLUM	60
3.1.6.1 Pooled sexes	60
3.1.6.2 Male and female DKO mice compared to WT mice	63
3.1.7 DKO SYNOPSIS	65
3.2 PSD ULTRASTRUCTURE OF <i>ProSAP1/Shank2</i> KNOCKOUT MICE COMPARED TO WILD-TYPE MICE IN THE DORSOLATERAL STRIATUM	66
3.2.2 <i>ProSAP1/Shank2</i> SYNOPSIS	69
4. DISCUSSION	70
4.1 ALTERATIONS OF THE CORTICO-STRIATAL SYNAPSE IN THE DORSOMEDIAL AND DORSOLATERAL STRIATUM OF DKO MICE	70
4.2 REDUCED PSD LENGTH IN HIPPOCAMPAL CA1 SYNAPSE OF DKO MICE	73
4.3 NO SIGNIFICANT ALTERATIONS IN CA3 PSDs OF MOSSY FIBERS IN DKO MICE	75
4.4 NO OBSERVED ALTERATIONS IN THE CEREBELLAR MOLECULAR LAYER OF DKO MICE	77
4.5 NO ULTRASTRUCTURAL ALTERATIONS IN THE GRANULAR LAYER OF THE CEREBELLUM IN DKO MICE	79
4.6 CONCLUSIONS	81
5. SUMMARY	83
6. REFERENCES	85
7. ACKNOWLEDGEMENTS	97

Abbreviations

°C	centigrade
ADHD	attention-deficit and hyperactivity disorder
AMPA	α -amino-3-hydroxy-5-methyl-4-isoxazolepropionic acid receptor
Ank	ankyrin repeats
ASD	autism spectrum disorder
CA1	Cornu Ammonis 1
Ca ²⁺	calcium ion
CA3	Cornu Ammonis 3
CNS	central nervous system
CO ₂	carbon dioxide
DG	dentate gyrus
DKO	double knockout
DLS	dorsolateral striatum
DMS	dorsomedial striatum
DSM	Diagnostic and Statistical Manual of Mental Disorders
Fmr1	Fragile-X-mental-retardation-protein-1
fMRI	functional magnetic resonance imaging
FMRP	Fragile X mental retardation protein
FXS	Fragile X syndrome
GABA	gamma amino butyric acid
GKAP	guanylate-kinase-associated protein
GLC	glomerular layer cerebellum
GluA1	AMPA subunit A1
GluA2	AMPA subunit A2
GluN1	NMDAR subunit N1
GluN2A	NMDAR subunit N2A
GluR	glutamate receptor
GRIP	GluR interacting protein
Hbs	Homer binding site
iGluR	ionotropic glutamate receptor
IQ	intelligence quotient

KO	knockout
kV	kilovolts
MECP2	methyl CpG binding protein 2
mGluR	metabotropic glutamate receptor
min	minute
ml	millilitre
MLC	molecular layer cerebellum
mRNA	messenger ribonucleid acid
nm	nanometer
NMDAR	N-Methyl-D-aspartic acid receptor
PBS	phosphate buffered saline
PDZ	PSD-95/DLG/ZO-1
PMS	Phelan-McDermid syndrome
ProSAP	Proline rich synapse associated protein
PrR	Proline-rich region
PSD	Postsynaptic density
PSD-95	Postsynaptic density protein-95
RNA	ribonucleic acid
SAM	sterile alpha motif
SH3	Src homology 3
stlm	stratum lacunosum et moleculare
sto	stratum oriens
stp	stratum pyramidale
str	stratum radiatum
WT	wild-type
µm	micrometre

1. Introduction

1.1 Autism spectrum disorders – ASD

1.1.1 Overview

Autism spectrum disorders (ASD), initially described as autism by Leo Kanner in 1968 [63], encompass a broad variety of syndromes, that all share two core features defined by the Diagnostic and Statistical Manual of Mental Disorders (DSM-5): i. deficits in reciprocal social interaction and ii. restricted or stereotypical behaviour [63,23,47].

With an estimated prevalence of 0.7-1.1 % [3,8,23,55,71,119,123] ASD is generally diagnosed in early childhood and was found to affect males more frequently than females, with a ratio of 4:1, in particular. Yet, the diagnosis of this early-onset neurodevelopmental disorder can only be made upon the occurrence of the core features, which, however, can broadly vary in their severity [11,55,106]. In addition to these defining features, many patients exhibit several co-morbid neurological disorders including mental retardation with an IQ below 70 in about 70 % of the patients, seizures in approximately 30 % [11], attention-deficit and hyperactivity disorder (ADHD), anxiety and mood disorders. Sleep disturbances and aggressive traits are also commonly mentioned symptoms in patients with ASD [3,33,55,119].

Due to this highly variable manifestation of the disease, the term ASD comprises a whole spectrum of syndromes, including Asperger's disease, Fragile X syndrome, Rett syndrome, Prader-Willi syndrome, Angelman syndrome, Tuberous sclerosis, Neurofibromatosis type 1 and Phelan-McDermid syndrome, to name just a few [23,55,109].

Similar to the heterogeneous manifestation, a high diversity of risk factors can contribute to ASD. Common risk factors include advanced age of the parents, *in utero* infections or prenatal stress [14,39,84]. Additionally, in approximately 20-25 % of the patients diagnosed for ASD, the formation of the disease has a genetic cause, especially a combination of genetic variations, are demonstrated [1,23,33,55]. Yet, more than 200 genes are known to be susceptible for mutations

finally causing ASD. Most of these genes regulate synaptic homeostasis, hence, an alteration of synaptic protein synthesis could lead to the phenotypes connected to ASD patients and thereby it is shown that synaptic homeostasis is crucial for normal brain development [8,23].

Furthermore, there are also single-gene disorders causing autism like Fragile X syndrome, Rett syndrome, Tuberous sclerosis, Neurofibromatosis type 1 and Phelan-McDermid syndrome. Since there is such a diversity of mutations linked to ASD, these disorders have to be diagnosed clinically in respect to the appearance of core symptoms, but for the majority of cases, the underlying mechanisms of the disease remain unknown [33].

Once appeared, the disorder maintains throughout the entire life and is mostly detected in early childhood. Up to an age of six months, 25-40 % of the children develop almost normally [3,32]. Children between 18 and 24 months of age evolve autistic-like behaviours and developmental delays, initially seen by their parents. In parallel to the occurrence of the first symptoms, a loss of intellectual skills is frequently observed and might be explained by the highly vulnerable state of the developing brain, since especially synaptogenesis takes place within this age [71]. However, on average, ASD is often not diagnosed until three years of age [23,33,71,109].

Since premorbid signs point toward ASD already in early postnatal stages [33], several attempts of ASD research focus on a categorization of children based on anatomical differences between normal developing children and children later diagnosed for ASD. A noticeable parameter measured in many children later diagnosed for ASD is the altered head circumference occurring in early postnatal life of pre-diagnosed children. Having normal or slightly reduced head circumferences at birth, there is an abnormally enhanced head growth within the first year of life in the patients [23]. This circumstance leads to macrocephaly accompanied with a reduction in neuron sizes, specifically Purkinje cells, and a decrease of the volume in the caudate nuclei by 10 % measured by fMRI (functional magnetic resonance imaging) [29,30,71]. Intriguingly, this reduction correlates with the severity of stereotypical, repetitive behaviours [54]. Moreover, structural changes in the hippocampus as well as an increase in its volume are described. By this means, even different forms of ASD can be distinguished [31,99]. Beside the alterations of those brain regions, a general increase of white

matter is observed in some autistic individuals [3]. This overgrowth leading to macrocephaly is observed in approximately 20 % of the individuals diagnosed with ASD. However, this abnormally enhanced head growth stagnates after 12 months of life [32].

1.1.2 Syndromic forms of ASD

In contrast to the broad variety of susceptibility genes of ASD, a subcategory of autism spectrum disorders is caused by defined single gene mutations. These distinct mutations induce diseases like Fragile X syndrome, Rett syndrome or Phelan-McDermid syndrome, that all share autistic traits as one of their symptoms.

1.1.2.1 Fragile X syndrome

Fragile X syndrome (FXS) is the most common genetic form of mental retardation. With a prevalence of 1 in 5000 males it causes 2-3 % of all patients diagnosed for ASD [9,15]. This disorder is caused by mutations of the X-chromosomal *FMR1*, leading to a hypermethylation of a trinucleotide (CGG) repeat in the promoter region of the *FMR1* gene, ending up in an incorrect expression and lower production of the fragile X mental retardation protein (FMRP). FMRP, an RNA-binding protein, required for the regulation of proper protein synthesis in dendritic spines, is reduced or absent in the dendritic spines of patients suffering from FXS. The loss of this protein manifests in symptoms like hyperactivity, anxiety, mood disorders, growth abnormalities, cranio-facial dysmorphies and macroorchidism [12,15,69,121]. Apart from the behavioural manifestation, mice lacking *FMR1* displayed morphological alterations expressed by longer and thinner dendritic spines [5,57].

Given that a mutation in a single gene, expressing a protein needed for synaptic homeostasis, leads to one form of autism, the main cause of ASDs is seen in a disorder within this homeostasis called synaptopathy [15,123].

1.1.2.2 Rett syndrome

In 1966, Andreas Rett described the Rett syndrome, a single gene defect leading to ASD with a prevalence of 1 in 10000 females and very rarely diagnosed in males. Rett syndrome is not inherited and is caused by a *de novo* germ cell mutation in the X-linked *MECP2* (methyl CpG binding protein 2) gene [10]. The absence of the gene product, required for neuronal stabilization and maintenance of neuronal maturity, leads to a delayed onset of symptoms at the age of 6 to 18 months [33]. After normal development, the patients develop a typical autistic-like phenotype including mental retardation, seizures, stereotypical behaviour, severe language delays and breathing abnormalities [10,123]. Interestingly, restoration of the gene in *Mecp2* knock-out mice leads to a normalisation of several symptoms [48]. In similarity to FXS, the Rett syndrome mouse model, with a knock-out of *Mecp2*, also shows morphological alterations within neuronal networks. Mice with a deletion of *Mecp2* are characterized by thinner cortical layers, decreased dendritic branching and reduced spine density, as well as reduced spine head size and elongated spine necks especially in the CA1 (Cornu Ammonis 1) area of the hippocampus [13,66].

1.1.2.3 Phelan-McDermid syndrome

Heterozygous deletions or translocations of the 22q13 locus elicit the Phelan-McDermid syndrome (PMS), also known as 22q13 deletion syndrome. The disruption of the *SHANK3* gene, which is coding for a synaptic scaffold protein at excitatory, glutamatergic synapses has proven to be the responsible cause of PMS [22]. In 80-85 % of PMS patients, a haploinsufficiency due to a *de novo* mutation of paternal origin (70 %) is responsible for the manifestation of PMS [89]. The Shank3 protein normally acts as scaffold protein in the postsynaptic density, which stabilizes receptor complexes and connects them to the cytoskeleton [95]. Approximately 2-3 % of all ASD patients carry mutations within this gene [55], leading to communication deficits and impairment of social interaction [36]. Further symptoms observed in PMS patients are developmental delay, neonatal hypotonia and mild cranio-facial dysmorphism [22,89,123]. The ultrastructural correlates of

murine tissues are displayed by a decrease of the spine density especially in the hippocampus as well as a reduced length and thickness of striatal postsynaptic densities [85,89].

Condensed, the genetic origins of autism are multifarious. However, mutations in many forms of ASD converge at dysfunctional synaptic homeostasis, predominantly in excitatory, glutamatergic synapses. Therefore, the pathology of these disorders represented by synaptic dysfunction, altered synaptic morphology and altered neuronal circuits suggest the synapse to be the key player in autism spectrum disorders [55].

1.2 The synapse

1.2.1 Overview

The term “synapse” was first noted and characterized by Charles Scott Sherrington in 1897 [105]. This neuronal structure, representing the functional unit of the nervous system, is essential for transmitting integrated signals between neurons in a chemical way. The classical synapse is located at the end of an axon, the so-called end-foot or bouton terminaux and the dendrite of another neuron, thus connecting two neurons or non-neuronal tissue with each other [80,91].

Within the central nervous system, the transmission of information occurs in different ways including i) axospinous, describing the transmission of information from an axon of a neuron to a dendritic spine of a subsequent neuron, ii) axodendritic, where information is transmitted by an axon to a following dendrite, iii) axoaxonal, where signals are directly transmitted from one to another axon and as a last variant of synaptic junctions in the central nervous system iv) axosomatic, which functions through a direct connection of an axon with the soma of another neuron [115]. Nevertheless, all those synapses go along with the same architectural structure [80].

The synapse is a polarized junction between neurons to transmit impulses from one neuron to another [80]. Precisely, the synapse consists of the presynapse, the postsynapse and the intervening synaptic cleft. The presynapse emerges of the membrane of the telodendron, the last axonal collateral, and unlike the axon or telodendron, there are no myelin sheaths at presynapses. As well as the presynapse, there are also specialisations in the postsynapse of the receptor cell, for excitatory synapses embodied by dendritic spines [80].

Until the 1950s, synapses were described by studies using only light microscopes. In 1956 Palay established „synaptolemma“ as a new term for synaptic components. This term included the presynaptic membrane, the postsynaptic membrane and the synaptic cleft [80,110]. Central components like the postsynaptic density (PSD), vesicles as well as the spine apparatus, however, were not mentioned. Beyond this nomenclature, Palay emphasized that those membranes never merge [80].

Interestingly, in the 1950s it was already known, even despite the low magnification of light microscopes at that time, that vesicles are present in the presynapse. The heterogeneous group of vesicles was further subclassified by the variable size of presynaptic vesicles and later, very large vesicles were noted as “multivesicular bodies” [83,88,110]. With a size range indicated by 24-52 nanometers (nm), these presynaptic organelles were considered to be storages of neurotransmitters. This was presumed by De Robertis and Bennett as the “synaptic vesicle theory” and was supported by many scientists in the late 1950s [82,115].

Further essential structures of the presynapse were the mitochondria. These organelles highlight the enormous energy demand of the synaptic machinery and thereby mitochondria are responsible for the electrical phenomenon appearing in here [80].

In addition to the postsynaptic membrane, the postsynaptic side further contains a dense patch or thickened region of postsynaptic membrane, which was later termed postsynaptic density (PSD) and is explained in the next chapter.

In contrast to the presynaptic part of the synapse, where vesicles and mitochondria are abundant, this is the only ultrastructural obtrusiveness of the postsynapse beside a sometimes existing “spine apparatus” [43,44,80,115].

The third entity of the synapse represents the synaptic cleft, which should not only be seen as intercellular space. According to the presynaptic and postsynaptic side, it has to be considered as a further highly organized synaptic specialisation. Although the technique of visualising synapses in the central nervous system has been established in 1959, published by E. G. Gray, it is astonishing how accurately the morphology of the synapse and its synaptic cleft had already been explored until then [44]. Even in studies using light microscopes, the synaptic cleft has been investigated. In 1956, Palay et al. measured an average width of the synaptic cleft of 20 nm [80]. More often the synaptic cleft is wider than randomly spaced axons or other processes [45,110]. The cleft is further described to contain an extracellular matrix, which is likely to stabilize this junction. Therefore, the synaptic cleft is a special appliance of the intercellular space. What would later turn out to be intermembranous adhesion molecules, e.g. Neuroligins/ Neurexins

or Ephrin/ EphR [53], has been described by De Robertis 1961 as "intersynaptic filaments". The role of those filaments was presumed i. to maintain the mechanical and geometrical stability, ii. to be responsible for a controlled transmitter diffusion or iii. to be involved in distinct communication procedures beside the chemical information transfer [27].

Long before the establishment of electron microscopes, it was already known that synapses are "one-way" conductions. Unlike the axon, neurotransmitters can only be released into the synaptic cleft at this specialisation, whereas axons are capable to carry neurotransmitters in a retrograde manner. This unidirectional character is substantive for the proper transmission of information. Already in the 1960s, it was presumed that each neuron uses only a single kind of transmitter [115]. Only a complex of more than one end-foot raising from more than one neuron, makes it possible to have more than one kind of transmitter in the synaptic cleft. These complexes can lead to even more controlled and fine-tuned information transmission. Soon after the release, the transmitters are degraded enzymatically, destroyed or recycled into the presynapse [35]. Nevertheless, not only presynaptically released transmitters are responsible for the entire signal transmission. As free floating substances, glutamate as well as GABA (gamma amino butyric acid) are supposed to sensitize postsynaptic receptors as "moderators or conditioners" [115]. Nowadays it is commonly known that this mechanism is managed by NMDARs (N-methyl-D-aspartate receptor) and long-term-potential (LTP).

1.2.2 Electron microscopic view on the synapse

The very first images of synapses on the electron microscope were made in 1953 and finally 6 years later, in 1959, E. G. Gray established the electron microscopy for visualizing cells of the central nervous system [44]. For the first time, synapses could be described in a more detailed view and a nomenclature for different types of synapses was established by E. G. Gray, which is still used today. Firstly, Gray described two types of synapses: the type I synapses and the type II synapses. The type I synapse is characterized by its thin presynaptic membrane and its distinctly thicker postsynaptic membrane. Since the great abundance of this type in the central nervous system, this type was termed foremost. In 88 % of type I synapses, the postsynaptic thickening contains 70-100 % of the entire postsynaptic specialisation of the synapse [43]. Some years later, in 1963, Van der Loos recognized that this specialisation was not a thickening of the membrane, but a highly organized cytoplasmic entity. He therefore recommended to replace the term “membrane thickening” into “postsynaptic membrane plus subsynaptic organelle”. Even De Robertis used the term “subsynaptic web” [27,110]. Finally, these terms merged and were included in what we nowadays entitle postsynaptic density (PSD), as described below.

In contrast to type I synapses, Gray’s type II synapses reveal no substantive morphological differences of the postsynapses compared to presynapses [43]. Since the width of the synaptic cleft does not differ much from non-synaptic contacts between axons, it was much more difficult to recognize type II synapses in light microscopic observations. Hence, electron microscopy brought crucial progress into the examination of type II synapses and synaptic junctions could now be distinguished from tight lying neural processes [87]. This circumstance was a trivial reason why this type of synapse was titled type II synapse [43,115].

Beside this nomenclature, there was a potentially improved designation by Colonnier, who established the terms “asymmetric type” and “symmetric type” of synapses [27]. This subdivision allowed a better classification of two extremes of a single continuum. Gray did not mention this continuum, which was the reason why he often has been criticized [27,110]. Despite this morphological difference, Van

der Loos even suspected a functional divergence of this basically same entity, which was finally proven later [110].

In addition to the postsynaptic density, there is another conspicuousness in the dendritic protrusion of the postsynapse, the “spine apparatus”. This structure is localized in the cytoplasm of spines of cerebral synapses [62] and consists of three or four annealed sacs with dense plaques in between [43–46,83,88,115]. This formation is in close connection to the smooth endoplasmic reticulum, situated in the cytoplasm of dendrites. Although this structure is localized in the range of dendrites, it is nevertheless termed “spine” apparatus. Intriguingly, those formations have not been found in cerebellar synapses or synapses in the spinal cord. Further, the spine apparatus is rarely found in non-spiny synapses and axodendritic junctions [62]. Until the late 1970s the role of the spine apparatus remained uncertain. In 1961, Rosenbluth considered the spine apparatus to be a form of membrane storage [92]. In 1979, Tarrant and Routtenberg hypothesized the spine apparatus to take part in the synaptic transmission and regulation of the postsynaptic membrane. For this, the spine had the possibility to change its shape, for instance to enlarge in order to react on increased use or to shrink in order to compensate non-use [107]. One year later, in 1980, a new theory of Westrum, Jones, Gray and Barron was proposed [114]. The previously stated condition, that there were no microtubules in spines, was disproved and a direct connection between those new found microtubules and the spine apparatus was mentioned. This new theory then lead to the presumption that the spine apparatus is a leading structure for microtubules, which thereby can get in contact with the postsynaptic membrane [114].

1.2.3 Morphology of dendritic spines

Dendritic spines are specialized protuberances of dendrites and serve as a basis for synaptic contact points. Studies on light microscopic correlates firstly supposed the spines to be “nutritive expansions” of neurons, since mitochondria were also reported to be present in dendritic spines [111]. In electron microscopic studies, at later times, these spines were further characterized as special platforms for synaptic contacts [17,44]. In the late 1960s, Jones and Powell published common attributes of the shape and size of dendritic spines, especially focussing on spine heads [62]. Great spine heads are predominantly localized at small dendrites, whereas small spine heads are mainly found at bigger dendrites. In addition to bigger spine heads, the spine stalks also appear to be larger in these spines [62] and Wilson et al. described a direct correlation within this phenomenon [116]. An increased spine head volume leads to an increase of the length of the spine stalk [62,116]. This correlation, however, was disproven in a more recent study of Arellano et al. in 2007 [7], so that only a relationship of the spine head volume and the PSD area can be postulated [97]. In particular, the PSD is considered to take 10-15 % of the entire spine head membrane [26]. Interestingly, Nusser et al. described a direct correlation between the PSD area and the amount of postsynaptic receptors [79].

Generally, it is believed that the morphology of dendritic spines has a crucial influence on synaptic function and stability and thus, considering a correlation of spine volume, PSD area and postsynaptic receptor concentration, the spine head volume determines its synaptic strength [7].

Basically, three different forms of dendritic spines are yet described: i. thick, short “stubby spines”, ii. “mushroom-shaped spines”, which are characterized by thicker spine stalks and great spine heads and iii. thin, “filopodial-like spines”, which are characterized by thin spine stalks and heads. But this conception, as well as the types of synapses, were extremes of a continuum, in which the single forms fluently merge [88]. At least for the cerebral cortex Arellano et al. could not find evidence for this classification, since the transition of single forms was fluently [7]. Notwithstanding, to date, this classification is still in use.

1.3 The postsynaptic density

The postsynaptic density (PSD) is an electron dense, disc-like structure located at the tip of a spine or dendritic shaft adjacent to the postsynaptic membrane. This postsynaptic formation comprises huge protein complexes, that mediate transsynaptic signaling, postsynaptic downstream effects as well as the ultrastructural organization of spines [21,101]. Based on various proteins, the PSD is displayed as a distinguishable circumscribed disc-like patch under the electron microscope, being the basic for the term asymmetric type of a synapse [27,44].

The proteins of the PSD can be subdivided into five groups; i. cell-adhesion molecules, ii. postsynaptic receptors, ion channels and G-proteins, iii. scaffold proteins, iv. adapter proteins and v. signaling proteins. These proteins fulfill numerous functions, including the stabilization of the synapse, the mediation of chemical signals to the subsequent neuron and the morphological organization of the dendritic spine [102] .

The diameter of a PSD varies between 300-400 nm with an average thickness of approximately 30-50 nm [101]. Within the entire thickness, the PSD is organized in three layers (Figure 1). The outer layer, representing proteins within the postsynaptic membrane, contains cell-adhesion molecules, as neuroligins, that link the postsynaptic membrane to the opposite presynaptic site via their interaction with neurexins, and different subtypes of glutamate receptors. The ionotropic N-methyl-D-aspartate receptors (NMDARs) are supposed to be localized in the center, whereas the ionotropic α -amino-3-hydroxy-5-methyl-4-isoxazolepropionic acid receptors (AMPAARs) together with metabotropic glutamate receptor (mGluR) are described to emerge at peripheral sites of the postsynaptic membrane. These glutamate receptors fulfill the cardinal function of excitatory synapses [21,102,112].

The subsequent, deeper layer comprises adapter proteins like PSD-95 (Postsynaptic density protein 95) and GKAP (Guanylate-kinase-associated protein). These proteins link NMDAR subunits to the third layer and control AMPARs at synapses. Additionally, GRIP (glutamate receptor interacting protein) and Homer link AMPARs and mGluRs, respectively, to downstream components in the third layer [21,25,101,102].

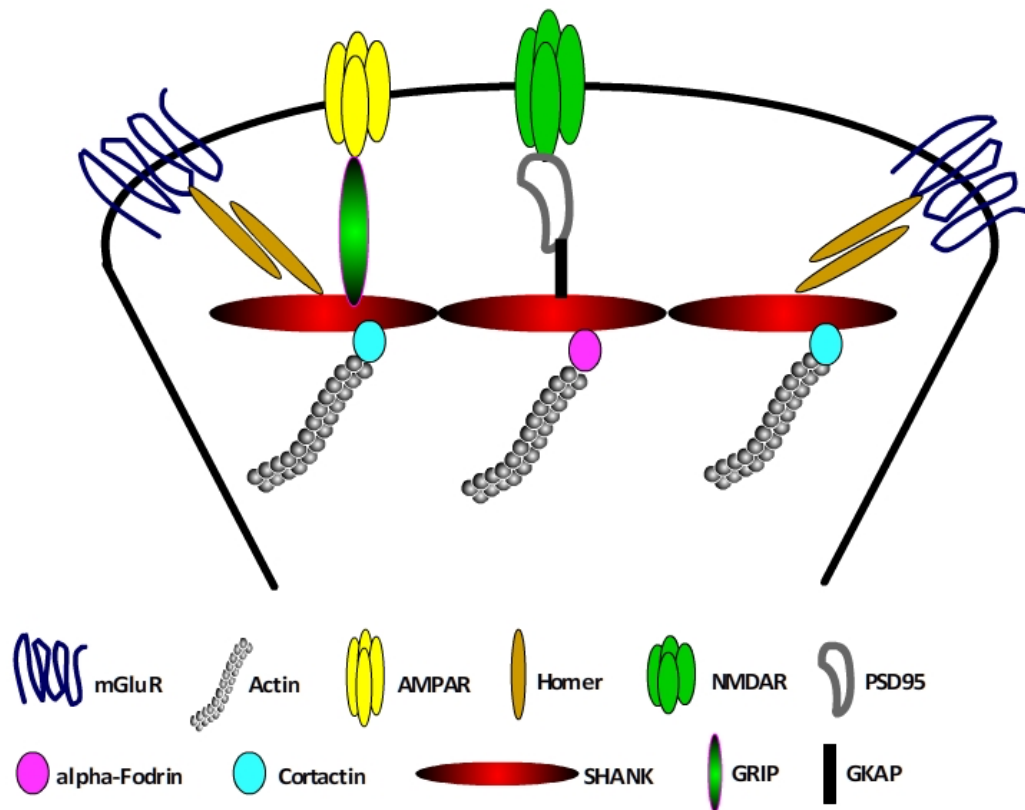


Figure 1: Scheme of the postsynaptic density (PSD). The outer layer of the postsynaptic density comprises glutamate receptors, including NMDAR (N-methyl-D-aspartic acid receptors), AMPAR (α -amino-3-hydroxy-5-methyl-4-isoxazolepropionic acid receptors) and mGluR (metabotropic glutamate receptors). These transmembrane receptors are bound to adapter proteins such as GRIP (GluR interacting protein), Homer, PSD95 (postsynaptic density protein-95) and GKAP (guanylate-kinase-associated protein), which are themselves connected to other cytoplasmic proteins like Shank proteins as well as the actin cytoskeleton interacting proteins, alpha-Fodrin and Cortactin.

The third and deepest layer comprises the ProSAP/Shank proteins, which lastly interact with the actin-based cytoskeleton, and thus stabilize synapses and spines and ensure proper spine maturation [95,101].

Taken together, the PSD with its hierarchically structured appearance is a dynamic and tightly-controlled construction, which is able to change its shape, size and assembly during maturation and in order to react on stimuli like synaptic activity. Hence, it is not surprising that the size of the PSD is directly correlated with the amount of receptors and thus a proportional correlation of PSD and synaptic strength can be observed [64,79,101]. Therefore, powerful excitatory synapses are accompanied with larger PSDs, including higher total PSD protein levels in particular of PSD 95 and AMPARs [102].

1.4 The ProSAP/Shank family

1.4.1 Overview

The ProSAP/Shank protein family includes three members, ProSAP1/Shank2, ProSAP2/Shank3 and Shank1 (further referred to as Shank2, Shank3 and Shank1, respectively), which all are highly enriched in the postsynaptic density (PSD). These proteins are described to link membranous receptors, that are integrated into the postsynaptic membrane, to the cytoskeletal network at excitatory, glutamatergic synapses [18,19,103]. Therefore, Shank proteins are localized in the inner layer of the PSD, situated between N-methyl-D-aspartic acid receptors (NMDAR), α -amino-3-hydroxy-5-methyl-4-isoxazolepropionic acid receptors (AMPA), as well as metabotropic glutamate receptors (mGluRs) and the actin cytoskeleton [95]. Shank proteins are mainly found within the central nervous system (CNS), but they can also be detected in non-neuronal tissues, as thymus, liver, kidney, pancreas as well as testicular germ cells [72,90].

All members of the Shank family, Shank1, Shank2 and Shank3 are presumed to act as master scaffolding proteins within the PSD, thereby organising and stabilizing this subsynaptic network [36,103].

For implementing this purpose, the Shank proteins share several protein domains. At the N-terminal end five ankyrin repeats are located, followed by an SH3 (src homology 3) domain and a PDZ (PSD-95/DLG/ZO-1) domain. Additionally, a SAM domain (sterile alpha motif) and Proline rich clusters are situated at the C-terminal end of the proteins (Figure 2). These protein domains are shared among the three Shank proteins with an amino acid identity of 63-87 % [18,103]. Beside linking glutamate receptors and their signalling to the cytoskeleton, the described protein domains are necessary for protein-protein interactions. To date, there are over 30 proteins known to interact with members of the Shank proteins family [61]. Furthermore, Shanks are able to form homodimers via zinc through nearly all domains [94,40,41]. The most important interacting partners are the Homer family, conjoining Shanks with mGluRs, and the PSD-95 family, which affiliate ionotropic glutamate receptors (iGluRs) like AMPAR and NMDAR to Shanks [78]. In this way, Shanks form a kind of relay station to interconnect iGluRs with mGluRs. Further

decisive interacting proteins are Cortactin and α -Fodrin regulating the connection between Shank proteins and the actin cytoskeleton, and thus finally linking glutamate receptors and their respective signalling components throughout the whole PSD to the actin based cytoskeleton [19,108].

Shank proteins are also able to contribute to presynaptic signalling by interacting with proteins of the neuroligin family, which are linked to the presynaptic membrane via neuroligins [36,106].

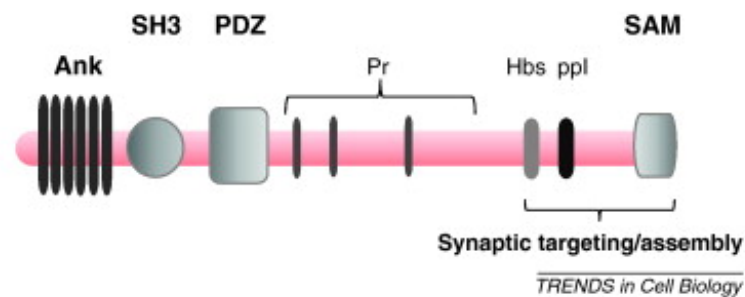


Figure 2: Scheme of protein-protein interaction domains of ProSAP/Shank family members, including N-terminal ankyrin repeats (Ank), Src homology 3 domain (SH3), PSD-95/DLG/ZO-1 domain (PDZ), proline-rich region (PrR), Homer binding site (Hbs), cortactin-binding domain (ppl) ending in the C-terminal sterile alpha motif (SAM). Reprinted from [41] with permission from Elsevier.

The Shank family members are widely present in the brain with different expression patterns. Particularly in the hippocampus and the cerebral cortex all three family members are highly present, with the peculiarity that *Shank3* is mainly expressed in the CA3 (Cornu Ammonis 3) region. In Purkinje cell dendrites within the molecular layer of the cerebellar cortex only *Shank1* and *Shank2* are found, whereas in granule cells, in the cerebellar granular layer, only *Shank3* and *Shank1* are expressed [18,19]. The striatal expression of *Shank* genes also shows a distinct pattern, with *Shank3* as the predominant member, *Shank2* with the second most abundance and *Shank1* as the least expressed [85]. In the hypothalamus, however, *Shank1* is the only present member of the Shank family (Table 1) [20].

Table 1: Shank expression in different brain regions [85,98]

CA1 (hippocampal Cornu Ammonis 1), CA3 (hippocampal Cornu Ammonis 3), MLC (molecular layer cerebellum), GLC (granular layer cerebellum); --- (no expression) +++ (strong expression)

	ProSAP1/Shank2	ProSAP2/Shank3	Shank1
Striatum	+	+++	(+)
CA1	++	+	+++
CA3	++	+++	+++
MLC	+++	---	++
GLC	---	+++	+

Moreover, Shank proteins appear in very early stages of development. At the first postnatal day, Shank1 and Shank2 mRNA is already detectable within dendritic spines, increasing during the first week and culminating at three to four weeks of life [19,20,108]. These changes in expression suggest that Shank proteins are crucial for early synaptogenesis and development of spines [61,94], since these processes also occur within this time [19]. Additionally, it is presumed that Shanks are not only important for early synaptogenesis, but also for the reorganisation of dendritic spines [18], promoted by an enlargement of spine heads [95], since overexpression trials of recombinant Shank2 and Shank3 fusion proteins were reported to lead to an increased establishment of excitatory synapses as well [40,41,94].

Finally, Shank proteins form giant platforms within the PSD of glutamatergic synapses in the aforementioned brain regions, enabling various proteins to lastly interact with numerous components of the synapse either in a direct or indirect manner. Therefore, these proteins are thought to be crucial for synaptic homeostasis as well as growth and maturation of spines.

1.4.2 *Shank* mutant mice

To investigate the individual function of each Shank family member within the synaptic network and synaptic homeostasis, knock-out and knock-in models of particular members of the Shank family were created [56,85,98,104,113,117,118]. Analysis of these models has already provided promising results in defining the precise roles of the distinct Shank proteins.

1.4.2.1 *Shank1* mutant mice

Shank1 mutant mice exhibit a deletion of exon 14-15 of the *Shank1* gene, encoding the PDZ domain. Since the PDZ domain is present in all Shank1 isoforms, this model is designed to eliminate all isoforms.

Since it is known, that mutations in the *Shank1* gene in humans can lead to ASD [96], an already existing mouse model was investigated thereupon [56,117].

Apart from slightly reduced body weight, *Shank1* mutant mice do not show any other alterations in general appearance, compared to wild-type littermates [117]. On the morphological level, however, convincing consequences of the deletion are observed. Mice lacking Shank1 show altered synapse morphology, expressed by smaller dendritic spines and lower synaptic strength. In parallel to the reduced spine size, the PSD thickness is decreased in the Cornu Ammonis 1 (CA1) area of the hippocampus [56]. Table 2 represents a morphological synopsis of the *Shank1* knockout mouse.

Interestingly, Homer proteins, coupling mGluRs to Shanks, are also reduced and thereby it is comprehensible that *Shank1* mutant mice suffer from impaired glutamatergic synaptic signalling [56].

Beside the morphological obtrusiveness, behavioural outcomes are conspicuous and represent behavioural patterns including the core features of autism. *Shank1* mutants, particularly pups, unveil alterations of communication, displayed by the disturbed cardinal forms of murine communication, ultrasonic vocalisation and scent marking [6,28]. Moreover, these mice display an anxiety-like phenotype with

lesser neuromuscular strength, an overall hypoactivity, but augmented spatial learning. However, social interaction skills were not impaired [104].

Table 2: Morphological changes in Shank1 knockout mice

CA1 (Cornu Ammonis 1), PSD (Postsynaptic density)

	spine density	spine length	spine head width	PSD length	PSD thickness
CA1 [56]	slightly reduced	slightly reduced	slightly reduced	reduced by 10 %	reduced by 5 %

1.4.2.2 *Shank2* mutant mice

Up to now there are two mouse models lacking all isoforms of *Shank2*, described by Schmeisser et al. 2012 and Won et al. 2012 [98,118]. *Shank2* deficient mice showed autistic-like behaviours in all its facets. These mice showed deficits in communication, measured by ultrasonic vocalisation. In addition to this, the social interactions skills were reduced and the last defining feature, repetitive and stereotypical behaviour became manifested in enhanced jumping comportment and slightly increased time spent with self-grooming [98,118]. Furthermore both mouse models exhibited an anxiety-like phenotype and hyperactive traits and the mouse model of Won et al. showed impaired spatial learning as well [118].

Consistent with other *ProSAP/Shank* mutants, synaptic protein compositions are altered in *Shank2* knock-out mice described by Schmeisser et al. [98]. Investigations of hippocampal protein levels revealed an increase of the NMDAR subunit GluN2B, whereas striatal measurements showed an enrichment of the GluN1 and GluN2A subunits as well as the AMPAR subunit GluA2. A compensatory upregulation of Shank3 was further described in the striatum [98]. In contrast to these findings, for the mouse model described by Won et al., a reduction of NMDAR function was supposed. Within the same model NMDA glutamate receptor agonists partially regained normal NMDAR function as well as social interaction skills. These results point towards a contribution of the NMDAR to the development of autistic-like phenotypes [118].

The morphological analysis of the knockout mouse model, examined by Schmeisser et al. 2012, revealed only some alterations showing a reduced overall spine density in the hippocampal CA1 area [72,98]. In the mouse model observed by Won et al. 2012, however, no alteration, neither in spine density, nor on ultrastructural investigations of PSD parameters, PSD length and PSD thickness, within the hippocampal CA1 area could be shown [118].

In table 3, a morphological synopsis of the *Shank2* knockout mouse models is shown.

Table 3: Morphological changes in Shank2 knockout mice

CA1 (Cornu Ammonis 1), PSD (Postsynaptic density), EM (electron microscopy), --- (no data available)

	spine density	spine length	spine head width	PSD length	PSD thickness
CA1 [118]	no change EM method	---	---	no change	no change
CA1 [98]	reduced Golgi method	---	---	no change	no change

1.4.2.3 *Shank3* mutant mice

In 2007, Durand et al. first mentioned an association of *SHANK3* mutations and autism in humans [36], serving as a basis for *Shank3* mutant models in the field of ASD research. To date, five mouse models exist, with each disrupting distinct isoforms of the Shank3 protein [67,85,98,113,122]. All five mouse models display autistic-like behaviour, compulsive behaviour, excessive self-injurious self-grooming, as well as impaired social interaction [67,85,98,113,122].

Similar to *Shank1* and *Shank2* mutant mice, synapses of *Shank3* mutant mice also display morphological alterations compared to wild-type littermates. These changes include reduced spine density in the CA1 area of the hippocampus and the striatum [85] and a reduction of PSD thickness and PSD length in the striatum [113]. In table 4, a morphological synopsis of the *Shank3* knockout mouse models is shown.

Interestingly, in the *Shank3* mutant model examined by Schmeisser et al. 2012, a compensatory upregulation of *Shank2* was observed [98].

On the molecular level, *Shank3* knockout mice of Schmeisser et al. revealed an upregulation of the NMDA subunit GluN2B and Shank2, whereas *Shank3* mutant mice of Peça et al. and Wang et al. showed a downregulation of glutamate receptor binding proteins, specifically Homer1, as well as NMDAR and AMPAR subunits [85,113,122]. Consistent with these findings, a reduction of cortico-striatal, glutamatergic transmission has been examined by Peça et al. [85], whereas Wang et al. observed a decrease in AMPAR signalling in the CA1 area of the hippocampus [122].

Shank3 seems to have a different impact on different brain regions, with the striatum being the most affected region. This finding is consistent with a high abundance of Shank3 in the wild-type striatum, thus, a *Shank3* knockout might have the most deleterious effects within this region [86].

Table 4: Morphological changes in Shank3 knockout mice

CA1 (Cornu Ammonis 1), PSD (Postsynaptic density), --- (no data available)

	spine density	spine length	spine head width	PSD length	PSD thickness
DLS [85]	reduced	no change	no change	reduced	reduced
CA1 [98]	no change	---	---	no change	no change
CA1 [113]	no change	Increased by 60 %	---	no change	no change
CA1 [67]	no change	---	---	---	---

1.5 Goals of this work

So far, only minor morphological alterations of synaptic parameters have been identified in *ProSAP/Shank* single mutants. In addition morphological characterization has been done only in a limited number of brain regions. Thus, it is suggested, that the newly described *ProSAP1/Shank2-ProSAP2/Shank3* double-knockout mice (Schmeisser et al. unpublished) suffer from even major ultrastructural changes.

Further aims of this study were to specifically delineate the brain regions, and sub-regions, in which these proposed ultrastructural alterations are present. This was implemented by electron microscopical screening of distinct brain regions, associated with ASD. In particular, ultrastructural analysis was performed in the dorsomedial and dorsolateral striatum, the hippocampal sub-regions CA1 and CA3 and the molecular and granular layer of the cerebellum.

2. Material and Methods

2.1 Material

2.1.1 Chemicals

Chemicals for experiments were purchased from following companies, unless indicated otherwise:

Table 5: Chemicals used for the experiments

Substance	Company
Sodium chloride	Merck
Chloral hydrate	Sigma
Heparin	Braun
Paraformaldehyde	Merck
25 % Glutaraldehyde	Agar Scientific
Saccharose	Roth
Cacodylic acid	Merck
Osmium tetroxide	Chempur
Uranyl acetate	Merck
Lead citrate	Plano
Epon	Fluka

2.1.2 Analysed mouse strains

All of the experiments documented in this thesis were performed with *ProSAP1/Shank2^{-/-}* knockout mice (KO) and *ProSAP1/Shank2^{-/-} - ProSAP2/Shank3^{-/-}* double-knockout mice (DKO), while wild type littermates (WT) served as controls. All KO and DKO mice were generated in house (Tierforschungszentrum Ulm) by cross-breeding as listed in table 6 below. Breeding of *ProSAP1/Shank2^{-/-}* and *ProSAP2/Shank3^{-/-}* mutant mice was kindly supervised by Jürgen Bockmann, Universität Ulm, and described earlier by Schmeisser et al. 2012 [98].

Single knockout, double-knockout and wild-type mice were investigated at defined postnatal stages (P70-P120). All littermate pairs were sex and age matched.

Table 6: Breeding scheme of analysed Shank2 KO (knockout) and Shank2/Shank3 DKO (double knockout) mice

Mutant line genotype	Breeding scheme
Shank2 KO	Shank2 ^{+/-} x Shank2 ^{+/-}
Shank2/Shank3 DKO	Shank2 ^{+/-} /Shank3 ^{-/-} x Shank2 ^{+/-} /Shank3 ^{-/-}

2.1.3 Investigated mice

All Investigated mice are listed as follows:

Table 7: Data of investigated double-knockout (DKO), single-knockout (KO) and mice and wild-type (WT) mice at distinct postnatal days (P)

mouse number	birth date	Gender	PCR result	Perfusion (age)
2483	198/12	♂	WT	P92
2497	202/12	♂	WT	P109
2191	336/12	♀	WT	P72
0018	358/12	♂	WT	P100
0030	9/13	♀	WT	P83
0036	16/13	♀	WT	P76
0071	59/13	♀	WT	P89
0269	162/14	♂	WT	P83
1996	198/12	♂	DKO	P92
2019	221/12	♂	DKO	P90
2196	338/12	♀	DKO	P70
2240	45/13	♀	DKO	P103
2267	67/13	♀	DKO	P81
0132	96/14	♂	DKO	P107
0016	346/12	♀	Shank2 KO	P112
0017	346/12	♀	Shank2 KO	P119
0021	352/12	♂	Shank2 KO	P106
0065	58/13	♀	Shank2 KO	P89

2.1.5 Equipment

Table 8: Equipment used in this study

Hardware	Company
Microm HM 650 V Vibration microtome	Thermo Scientific
Microscope Slides	Roth
Stereo microscope Stemi 2000	Zeiss
Ultracut UCT Ultramicrotome	Leica
Primo Star light microscope	Zeiss
Grids 300 Mesh Copper 3.05 mm	Agar Scientific
JEM 1400 transmission electron microscope	Jeol

2.1.6 Software

Table 9: Software used for analysis

Software	Company
iTEM Platform	Olympus Soft Imaging Solution GmbH
Graph Pad Prism 5.0.a	GraphPad, Software Inc.
ImageJ	National Institutes of Health, USA
Microsoft Word 2011	Microsoft Corporations

2.2. Methods

2.2.1 Tissue preparation

Postnatal mice at the age of P70-P120 were prepared, always processing one WT mouse and one mutant (DKO or *Shank2* KO respectively) in parallel. The mice were first stunned with CO₂ followed by an injection of 0.5 ml chloral hydrate-solution (25 %) to obtain deep anaesthesia. This procedure was done by a technician, specially trained for this purpose, being mentioned in the ethics approval.

Before the perfusion, the mouse chest was cut open in the median to expose the heart. The right atrium was then opened to remove the blood and a cannula was placed into the left ventricle. By means of a syringe pump, the animals were now perfused with 20 ml of solution 1 followed by 50 ml of solution 2 (listed in table 10 below) for three minutes. After perfusion, mouse brains were dissected and postfixed in solution 3 at 4 °C over night.

Table 10: Perfusion solutions

Contents of solutions	
solution 1	0.5 % heparinized saline solution
solution 2	2 % PFA (paraformaldehyde) 2.5 % GA (glutaraldehyd) 1 % saccharose in 0.1 cacodylate phosphate buffer at pH 7.4
solution 3	2 % GA 1 % saccharose in 0.1 M cacodylate buffered saline

After the completion of the postfixation process, frontal sections in the size of 200 µm were cut with the vibratome. The regions of interest, which are the dorsomedial striatum (DMS) and the dorsolateral striatum (DLS), Cornu Ammonis area 1 (CA1) and Cornu Ammonis area 3 (CA3) of the hippocampus as well as the molecular and granular layer of the cerebellar cortex (MLC and GLC), were dissected in 1 mm² pieces using a stereo microscope and then stored in cacodylate buffer solution. Further on, the specimens were washed in 0.1 M phosphate buffered saline (PBS), postfixed with 2 % osmium tetroxide for one

hour and dehydrated with ascending propanol series (30 %, 50 %, 70 %, 90 %; each 2-3 min). Additionally, uranyl acetate, diluted in denatured ethanol, was used to contrast the specimens for 30 minutes at 37 °C. The samples were then treated with 100 % propanol (3 x 30 minutes). Propaline oxide treatment (2 x 5 minutes) finished the dehydration process and hereafter the specimens were embedded in Epon.

The embedded specimens were cut into 0.5 µm section with the ultratome to create semi-thin sections and further stained with toluidine blue. Within these semi-thin sections, the sub-regions of the above aforementioned regions were selected using a light microscope. Moreover the defined sub-region were cropped in the Epon-embedded pieces, cut to ultrathin sections (70-80 nm) and collected on 300 mesh copper grids.

2.2.2 Electron microscopy

All analysed specimens were investigated on a Jeol JEM 1400 transmission electron microscope at 120 kV. For this purpose the software Olympus Soft Imaging Solution was used. Pictures were all taken with a side-mounted CCD TEM camera Olympus Valeta with 2k x 2k pixels. In all brain regions analysed, two distinct magnifications were selected to address the following aims. A magnification of 25.000x was chosen to study the density of postsynaptic densities (PSDs) within the image section. Generally, synapses were counted within a whole picture with an area of 35.8 µm², whereas in the hippocampal CA3 area, as well as in the granular layer of the cerebellum, all synapses were exclusively counted at a single mossy fiber bouton. A magnification of 80.000x was further applied for measuring the PSD length and thickness as well as the width of the synaptic cleft of the axon terminals.

Images were randomly taken in the given areas. All pictures were taken with an exposure time of 1000 milliseconds. After all the images were saved in 8 bit TIFF format files with a resolution of 4 megapixels (2048 x 2048).

2.2.3 Statistical analysis

The software ImageJ (National Institutes of Health, USA) was used to determine the length and thickness of PSDs as well as the width of the synaptic cleft (Figure 3a) by an observer blinded for the genotypes of the specimens. All statistics were performed with GraphPad Prism.

Since asymmetrical, type I synapses are described to have a width of the synaptic cleft of about 20 nm, this parameter was determined as control parameter. On this account only synapses with a throughout constant width of the synaptic cleft of about 20 nm were included into the study, to only investigate synapses being cut in the centre. Furthermore symmetrical, type II synapses have narrower widths of the synaptic cleft of about 12 nm [45,110], which could therefore be excluded.

The PSD volume was calculated by means of the PSD length and thickness (calculation indicated in Figure 3b).

The data is presented as cumulative frequency plot. This type of diagram reveals the number of a distinct phenomenon with its smallest and largest values as well as the values in between. The values are presented as relative sum frequency as well.

Furthermore, the data is presented as frequency distribution in a separate bar graph. This representation reveals the frequency of individual readings. A Gaussian curve represents the normal distribution of each parameter. This procedure was used in order to evaluate the PSD length, thickness and volume as well as the width of the synaptic cleft.

The calculation of the overall mean values of each group, presented as column bar as mean \pm s.e.m., was based on the individual mean values of each animal.

To assess the significance of obtained differences between two groups, an unpaired t-test was accomplished with a significance level set to 5 % and a confidence interval of 95 %.

As a first part, the data for all PSD parameters is shown in a pooled section, where all animals are included, regardless of gender. In the second section, the PSD density, length and thickness are shown divided by gender. Within the latter part,

the wild-type mice data comprise male and female mice, since the results showed equal outcomes.

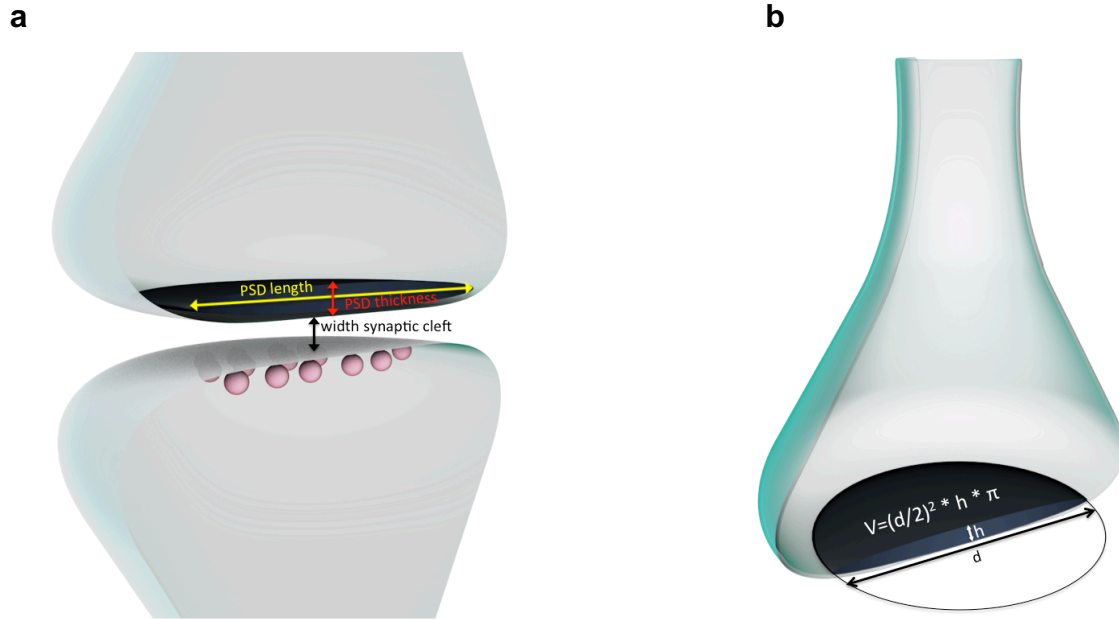


Figure 3: Three-dimensional images of a synapse with the postsynaptic density (PSD) displayed in black, presynaptic vesicles in red. The measurement of PSD length and thickness as well as the width of the synaptic cleft is schematically illustrated in **a**. The procedure to calculate the PSD volume is depicted in **b**. V (volume), d (diameter), h (height), π (pi).

2.2.4 Analysed brain regions

Within this thesis, the following brain regions which are described to be affected in autism were analysed: dorsomedial striatum (DMS), dorsolateral striatum (DLS), Cornu Ammonis 1 and 3 region of the hippocampus (CA1 and CA3), as well as the molecular and granular layer of the cerebellar cortex (MLC, GLC).

2.2.4.1 Striatum

The semi-thin sections of the dorsomedial and the dorsolateral striatum were prepared for electron microscopy (Figure 4), as described above and accordingly adjusted in the electron microscope (Figure 5). Unlike the human striatum, the striatum of the mouse, is not as strictly separated by the capsula interna into the caudate nucleus and the putamen. The fibers processing through this region are

arranged in patches. Pictures were only taken in areas free of fiber patches and preferably free of cell bodies or other processes as dendrites. In a magnification of 25.000x the PSD density was measured. For measuring the PSD parameters, width of the synaptic cleft, PSD length and thickness as well as the PSD volume, pictures were taken in a magnification of 80.000x.

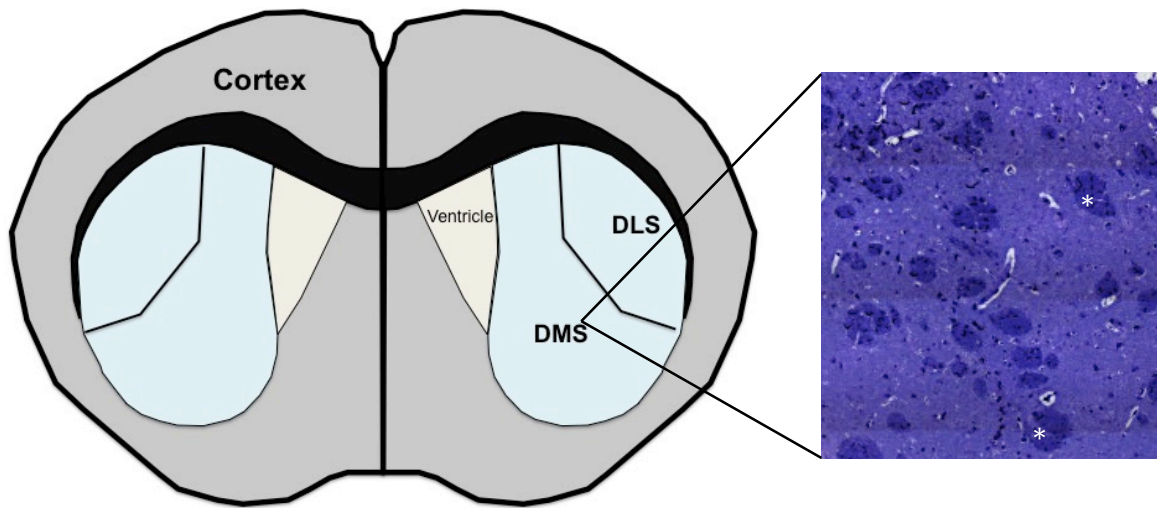


Figure 4: Image modified from Kreitzer 2009 [68]. Left side: schematical illustration of a frontal section of a mouse brain. Blue region represents the striatum, divided in dorsomedial striatum (DMS) and dorsolateral striatum (DLS). Right side: semi-thin section of the investigated sub-region DMS. Asterisks: axon fiber patches processing through this region.

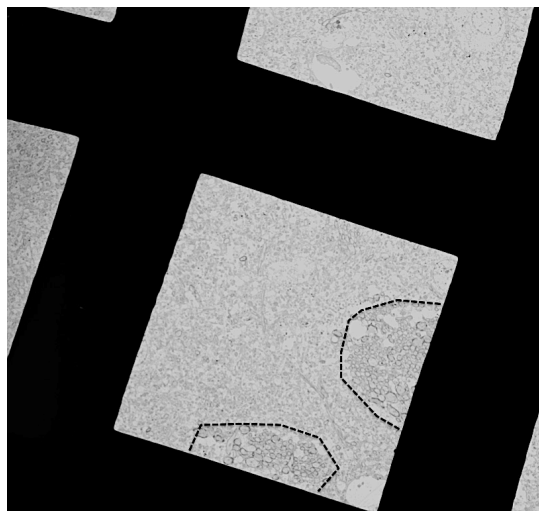


Figure 5: Electron micrograph representing a part of the dorsomedial striatum; dashed lines: axon fiber patches running through this region.

2.2.4.2 Hippocampus CA1

Before evaluation, the CA1 region of the hippocampus was localized in the semi-thin sections (Figure 6), and only synapses, occurring in the radial layer, were investigated (Figure 7).

For recognizing this region in the electron microscope, the pyramidal layer, containing the cell apparent cell bodies as well as the alveus, served as point of orientation. Distinct axons, being located certain micrometres beyond the cell bodies, represent the alveus, embodied by axons running through. In front of the pyramidal layer, the radial layer of CA1 is characterized by radial oriented dendrites, which are finally ending in “Schaffer collateral” synapses, the synapses of interest within this thesis. In a magnification of 25.000x the PSD density was measured. Similar to the examination of the striatum, only pictures of fiber and cell body free regions were taken for the analysis. For measuring the PSD parameters, width of the synaptic cleft, PSD length and thickness as well as the PSD volume, pictures were taken in a magnification of 80.000x.

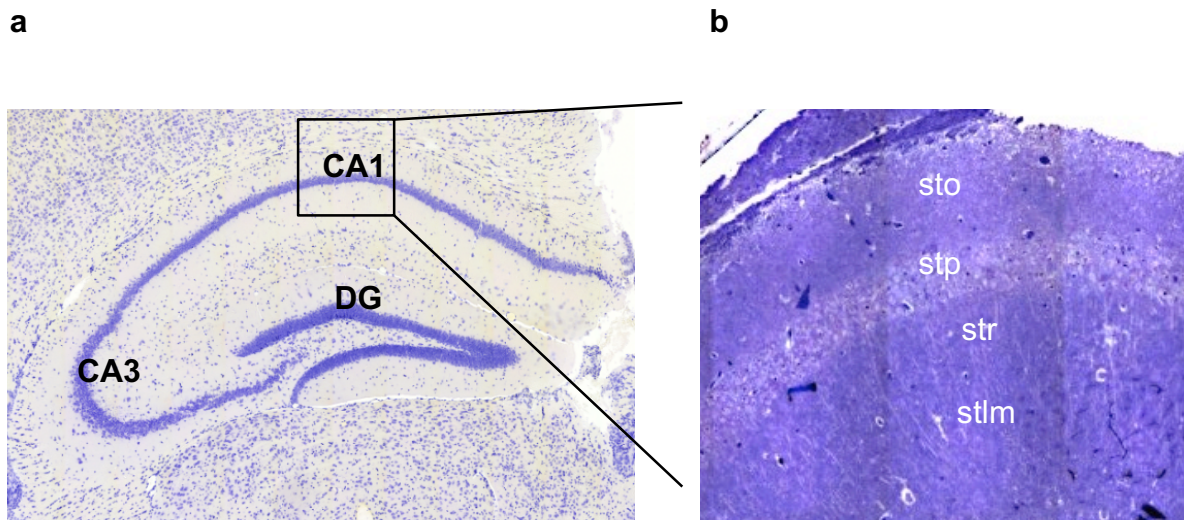


Figure 6: **a** Frontal section of the hippocampus with marked sub-regions, Cornu Ammonis area 1 (CA1), Cornu Ammonis area 3 (CA3) and dentate gyrus (DG). **b** Semi-thin section of the CA1 area; stratum oriens (sto), stratum pyramidale (stp), stratum radiatum (str), stratum lacunosum et moleculare (stlm)

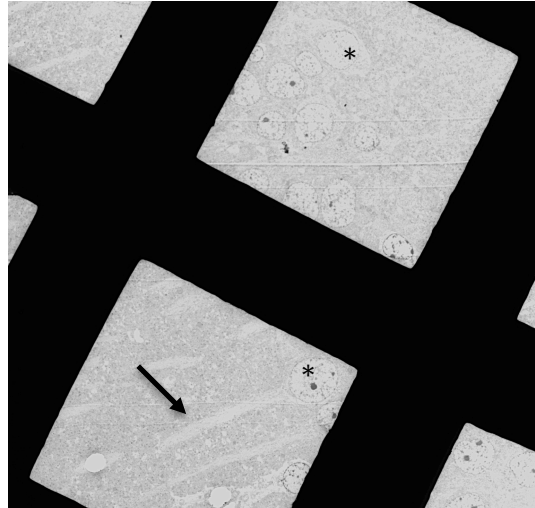


Figure 7: Electron micrograph representing a section of the CA1 area. Asterisks: pyramidal neurons within the pyramidal layer of this area; arrow: dendritic protrusion of a pyramidal neuron in the radial layer.

2.2.4.3 Hippocampus CA3

The CA3 region of the hippocampus was localized in the semi-thin sections (Figure 8). Within this region the synapses of mossy fibers were investigated (Figure 9). This asymmetrical type of synapses, localized in the stratum radiatum, is characterized by their giant presynaptic boutons, originating from granule cells of the dentate gyrus, which contain large amounts of vesicles. In general, the axon terminals of granule cells and dendrites of the pyramidal cells of the CA3 region are reported to form a plenty of synapses.

Characterizing the synapses of mossy fiber boutons according to these conditions, the synapse number and PSD parameters, width of the synaptic cleft, PSD length and thickness as well as the PSD volume, were assessed in a magnification of 25.000x, 80.000x respectively.

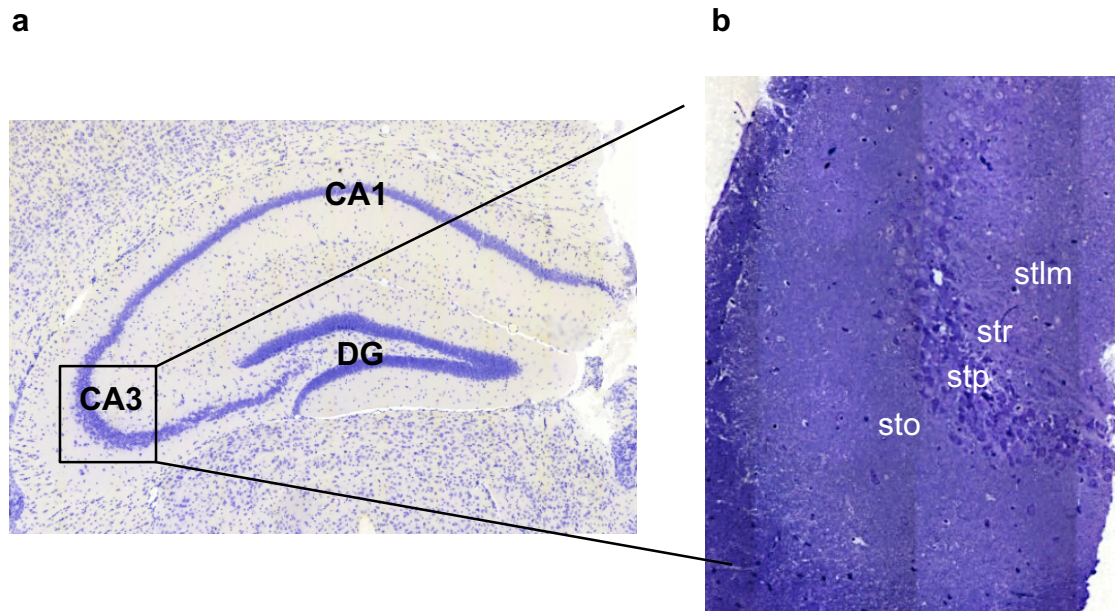


Figure 8: **a** Frontal section of the hippocampus containing Cornu Ammonis area 1 (CA1), Cornu Ammonis area 3 (CA3) and dentate gyrus (DG). **b** Semi-thin section of the CA3 area; stratum oriens (sto), stratum pyramidale (stp), stratum radiatum (str), stratum lacunosum et moleculare (stlm),

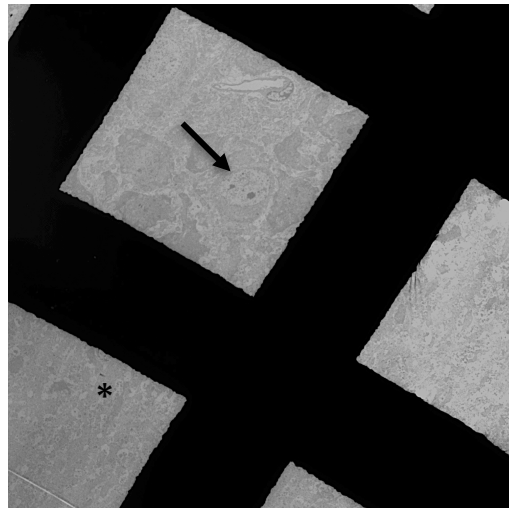


Figure 9: Electron micrograph representing a part of the Cornu Ammonis area 3 (CA3). Arrow: pyramidal cell of the pyramidal layer. Asterisk: stratum radiatum containing mossy fibers.

2.2.4.4 Molecular and granular layer of the cerebellum

The cerebellar cortex is characterized by three layers. These layers comprise the inner granular layer typified by granule cells sending parallel fibers into the molecular layer, the middle Purkinje cell layer consisting of large Purkinje cells with their characteristic dendritic arborisation expanding into the third layer, described as the molecular layer (Figure 10 and 11).

Synaptic parameters were evaluated in asymmetric synapses in the molecular layer and in the granular layer of the cerebellum (ml and gl in Figure 10). These synapses comprise climbing and parallel fiber synapses in the molecular layer and mossy fiber synapses in the granular layer.

The spines of Purkinje cell dendrites are described to be sphere-like and to contain an electron dense material in the core of the spine head [70]. Thus, only synapses with a clear black mass in the corresponding spine head were included into the analysis within the molecular layer.

In the granular layer, synapses of mossy fiber boutons were evaluated. These synapses are organized in the so-called glomeruli cerebellares, where giant mossy fiber boutons are surrounded and connected to granule cell dendrites.

For evaluating the PSD density, a magnification of 25.000x was chosen. The PSD parameters, width of the synaptic cleft, PSD length and thickness as well as PSD volume, were again assessed with a magnification of 80.000x.

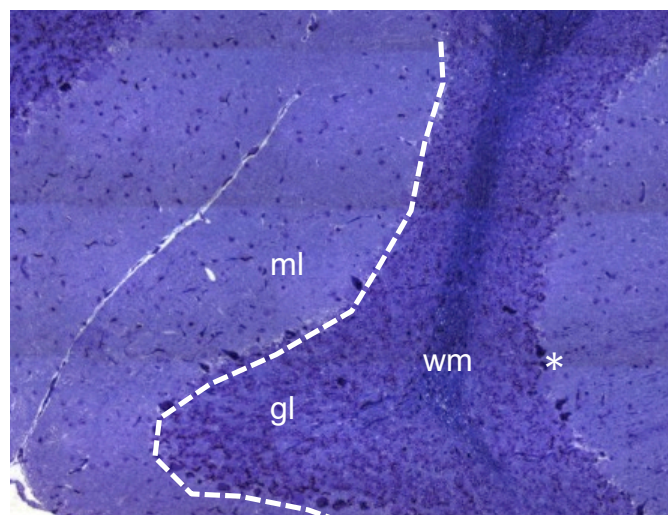


Figure 10: Semi-thin section of the cerebellar cortex: white matter (wm), granular layer (gl), molecular layer (ml), asterisk situated next to a Purkinje cell; dashed line: Purkinje cell layer.

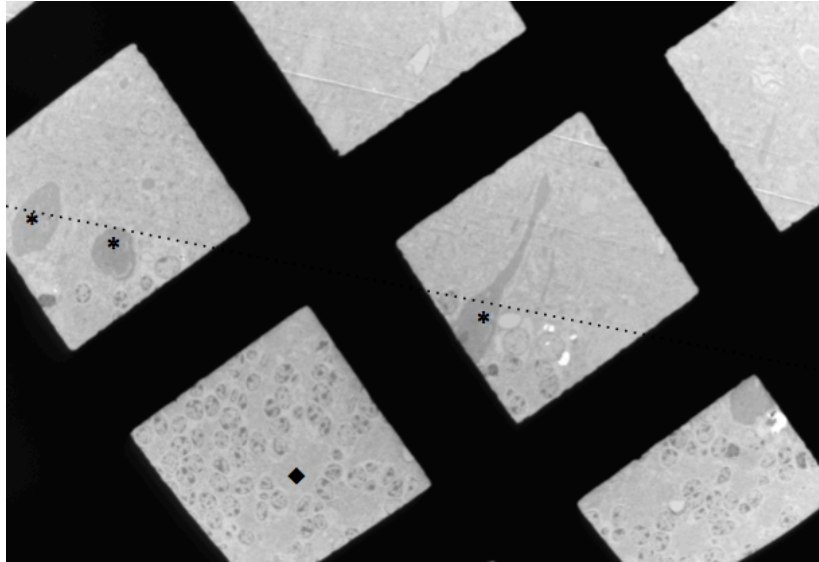


Figure 11: Electron micrograph representing parts of all three layers building the cerebellar cortex. Rhombus: glomerulus cerebellaris in the granular layer; asterisks: Purkinje cell bodies within the Purkinje cell layer penetrating the molecular layer; spotted line: border between the Purkinje cell layer and the molecular layer of the cerebellar cortex

3. Results

3.1 PSD ultrastructure in distinct brain regions of *ProSAP1/Shank2* and *ProSAP2/Shank3* double-knockout mice compared to wild-type littermate controls

The following section contains the results of the electron microscopic ultrastructural analysis of *ProSAP1/Shank2* and *ProSAP2/Shank3* double-knockout mice (DKO). PSD ultrastructure was analyzed in different brain regions, in particular dorsomedial and dorsolateral striatum, CA1 and CA3 area of the hippocampus as well as the molecular and the granular layer of the cerebellum. All analyzed parameters were compared to wild-type mice (WT). Measured parameters include PSD density, width of the synaptic cleft and PSD length, thickness and volume. PSD volumes were calculated by the means of PSD length and thickness.

3.1.1 Dorsomedial Striatum

3.1.1.1 Pooled sexes

The PSD ultrastructure was analyzed in the dorsomedial striatum (DMS) of *ProSAP1/Shank2* and *ProSAP2/Shank3* double-knockout mice and age-matched wild-type controls.

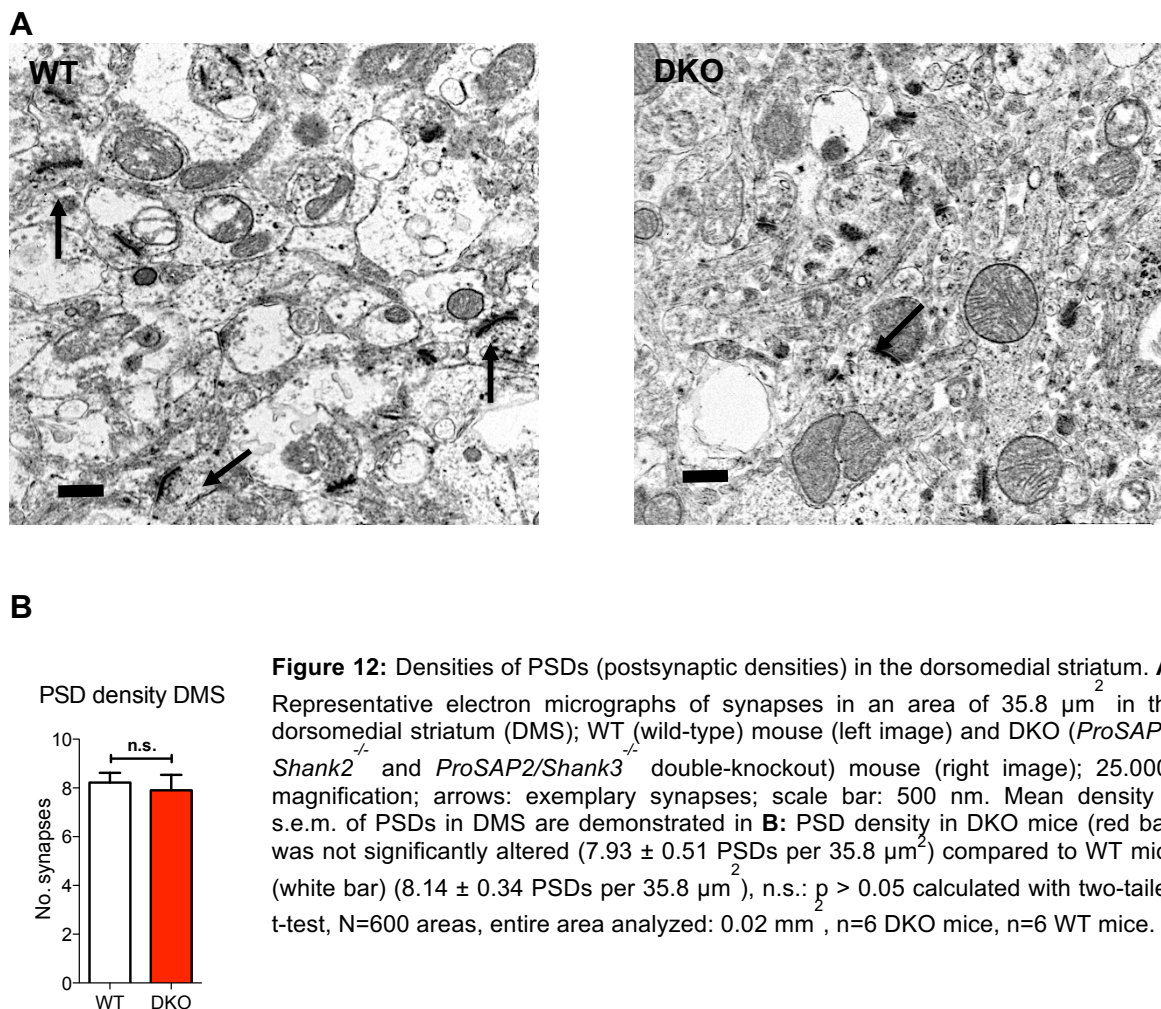
The PSD density was measured in a low magnification of 25.000x. In an area of 35.8 μm^2 , 7.9 synapses were detected in DKO mice and 8.1 synapses in WT mice. No significant alteration of the overall amount of PSDs between the two genotypes was observed ($p=0.73$) (Figure 12).

The width of the synaptic cleft, PSD length and thickness were measured with a greater magnification of 80.000x. In both genotypes, the width of the synaptic cleft ranged between 15 and 25 nm, with a mean value of 20 nm (Figure 13 B). The width of the synaptic cleft was not significantly altered in DKO mice ($p=0.20$).

Significant alterations of the PSD structure, however, were found in the PSD size, which showed a highly significant length reduction of 22.3 % in DKO compared to WT mice ($p < 0.0001$). DKO mice showed a mean PSD length of 209.7 nm (Figure 13 C a and b) ranging between 107 nm and 401 nm, whereas in WT mice, a mean PSD length of 270.2 nm was measured with values ranging between 110 and 702 nm.

The PSD thickness did not significantly differ between both strains ($p = 0.91$) and ranged between 16 and 45 nm with a mean of 29.0 nm in DKO mice. The PSD thickness in WT mice was situated between 17 and 48 nm, with a mean of 29.2 nm (Figure 13 D a and b).

The calculation of the PSD volume by means of PSD length and thickness revealed a highly significant reduction of 41.4 % in DKO mice ($p = 0.0005$) (Figure 13 E a and b).



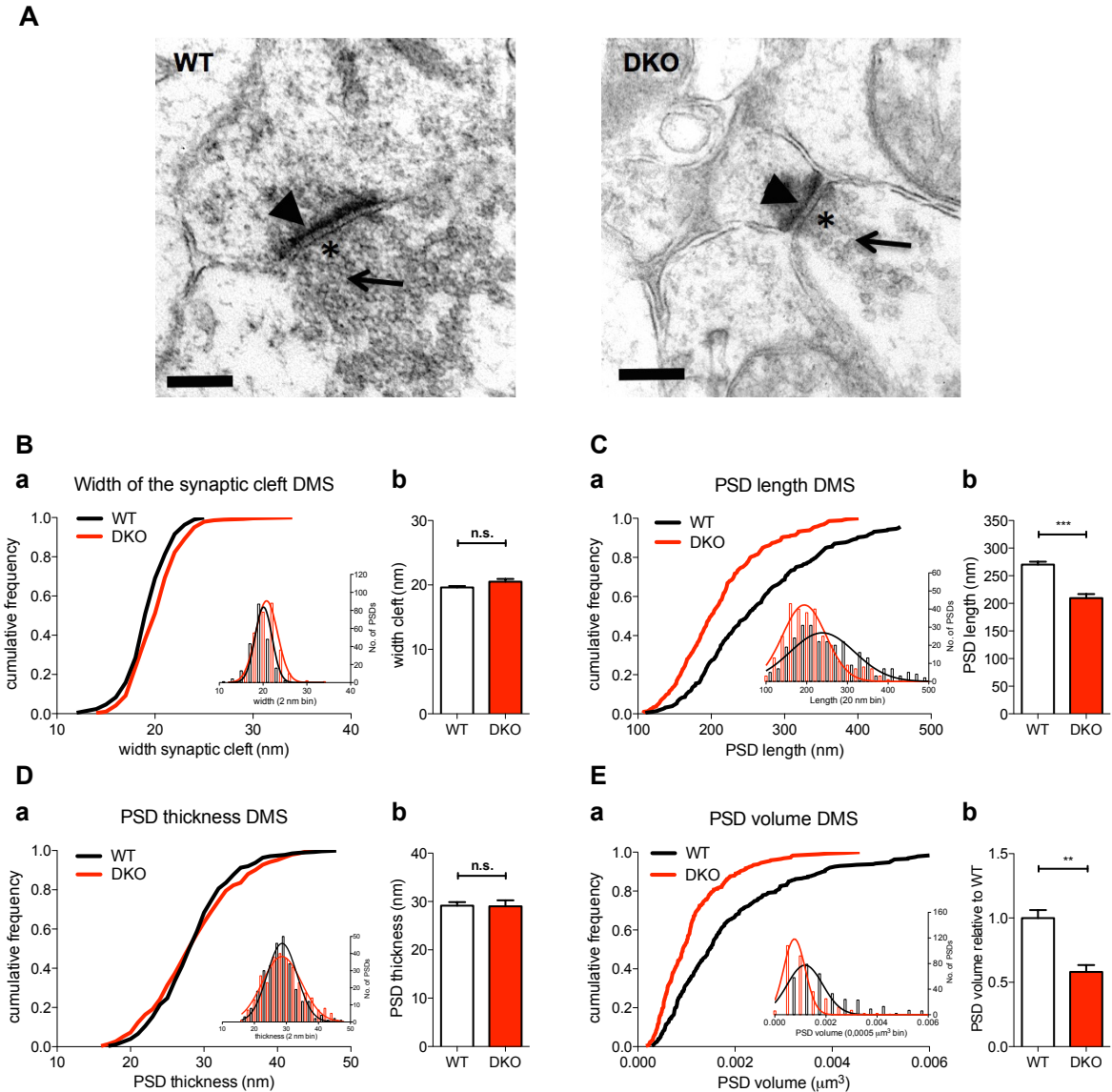


Figure 13: PSD parameters in DMS

A: Representative electron micrographs of synapses in the dorsomedial striatum (DMS); wild-type mice (WT) (left image) and DKO mice (*ProSAP1/Shank2*^{-/-} and *ProSAP2/Shank3*^{-/-} double-knockout) (right image); 80.000x magnification; arrowheads: PSDs; arrows: presynaptic vesicles; asterisks: active zone; scale bar: 200 nm.

B: Width of the synaptic cleft **a:** Data is presented as cumulative frequency plot; inset reveals the frequency distribution with Gaussian curves of the data. The plot presents the distribution of the width of the synaptic cleft of all measured synapses in the DMS; N=570 synapses, n=6 wild-type mice (WT), n=6 DKO mice; Data in **b:** Mean width of synaptic cleft + s.e.m.; n=6 WT mice (white bar) 19.60 nm ± 0.25 nm and n=6 DKO mice (red bar) 20.40 nm ± 0.51 nm. The width of synaptic cleft of DKO mice revealed no significant alteration compared to WT mice; n.s.: p > 0.05 calculated with two-tailed t-test.

C, D and E: PSD length, thickness and volume **a:** Data are presented as cumulative frequency plots; insets reveal the frequency distributions with Gaussian curves of the data; **b:** Mean + s.e.m of the data. **C a:** PSD length distribution of synapses in the DMS; N=570 PSDs, n=6 WT (black line), n=6 DKO (red line). **b:** Mean + s.e.m of the PSD length, WT: 270.20 nm ± 5.33 nm (white bar), DKO: 209.70 nm ± 7.25 nm (red bar). The PSD length in DKO mice was significantly reduced; ***p < 0.001 calculated with two-tailed t-test. **D a:** PSD thickness distribution of synapses in the DMS, N=567 PSDs, n=6 WT (black line), n=6 DKO (red line). **b:** Mean + s.e.m of the PSD thickness, WT: 29.17 nm ± 0.70 nm (white bar), DKO: 29.00 nm ± 1.27 nm (red bar). There were no significant changes in PSD thickness in the DMS; n.s.: p > 0.05 calculated with two-tailed t-test. **E a:** PSD volume distribution of synapses in the DMS, N=570 PSDs, n=6 WT, n=6 DKO mice. Data in **b:** Mean PSD volume + s.e.m. of all measured synapses relative to WT; n=6 WT (black bar) mice and n=6 DKO mice (red bar). PSD volumes were significantly reduced in DKO mice; **p < 0.001 calculated with two-tailed t-test.

3.1.1.2 Male and female DKO mice compared to WT mice

In this section, the results of ultrastructural parameters in the DMS of male and female DKO mice are shown.

Within this area the PSD density was analysed and equal to the pooled data, no significant changes of the overall amount of PSDs was observed between WT mice (8.1 synapses per $35.8 \mu\text{m}^2$), male DKO (8.1 synapses per $35.8 \mu\text{m}^2$) and female DKO mice (7.8 synapses per $35.8 \mu\text{m}^2$) (Figure 14).

The analysis of the PSD length of male and female DKO mice yielded a slight difference in the PSD length. The PSD length of male DKO mice ranged between 107 and 381 nm with a mean length of 201.7 nm. Female DKO mice showed a mean PSD length of 217.7 nm, with values ranging between 108 nm and 401 nm. While female DKO mice showed a reduction in the PSD length of 20 % ($p=0.008$), the PSD length in male DKO mice was reduced by 24 % compared to pooled WT animals ($p=0.0096$) (Figure 15 B a and b).

Equivalent to the results obtained from the pooled analysis, the PSD thickness did not significantly differ between WT, male DKO ($p=0.78$) and female DKO mice ($p=0.86$). While the values in all genotypes ranged between 17 nm and 42 nm, a mean PSD thickness of 27.6 nm in male DKO mice and 30.3 nm in female DKO mice was measured (Figure 15 C a and b).

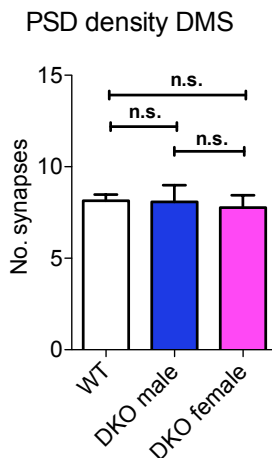


Figure 14: Mean density + s.e.m. of PSDs (postsynaptic density) in the dorsomedial striatum (DMS) of male and female DKO mice (*ProSAP1/Shank2*^{-/-} *-ProSAP2/Shank3*^{-/-} double-knockout) in an area of $35.8 \mu\text{m}^2$. No significant alteration was observed in PSD density of male DKO mice (blue bar) (8.09 ± 0.91 PSDs per $35.8 \mu\text{m}^2$) and female DKO mice (magenta bar) (7.77 ± 0.68 PSDs per $35.8 \mu\text{m}^2$) compared to pooled WT mice (wild-type) (white bar) (8.14 ± 0.34 PSDs per $35.8 \mu\text{m}^2$), n.s.: $p > 0.05$ two-tailed t-test, N=600 areas, entire area 0.02 mm^2 , n=6 WT mice, n=3 male DKO mice, n=3 female DKO mice.

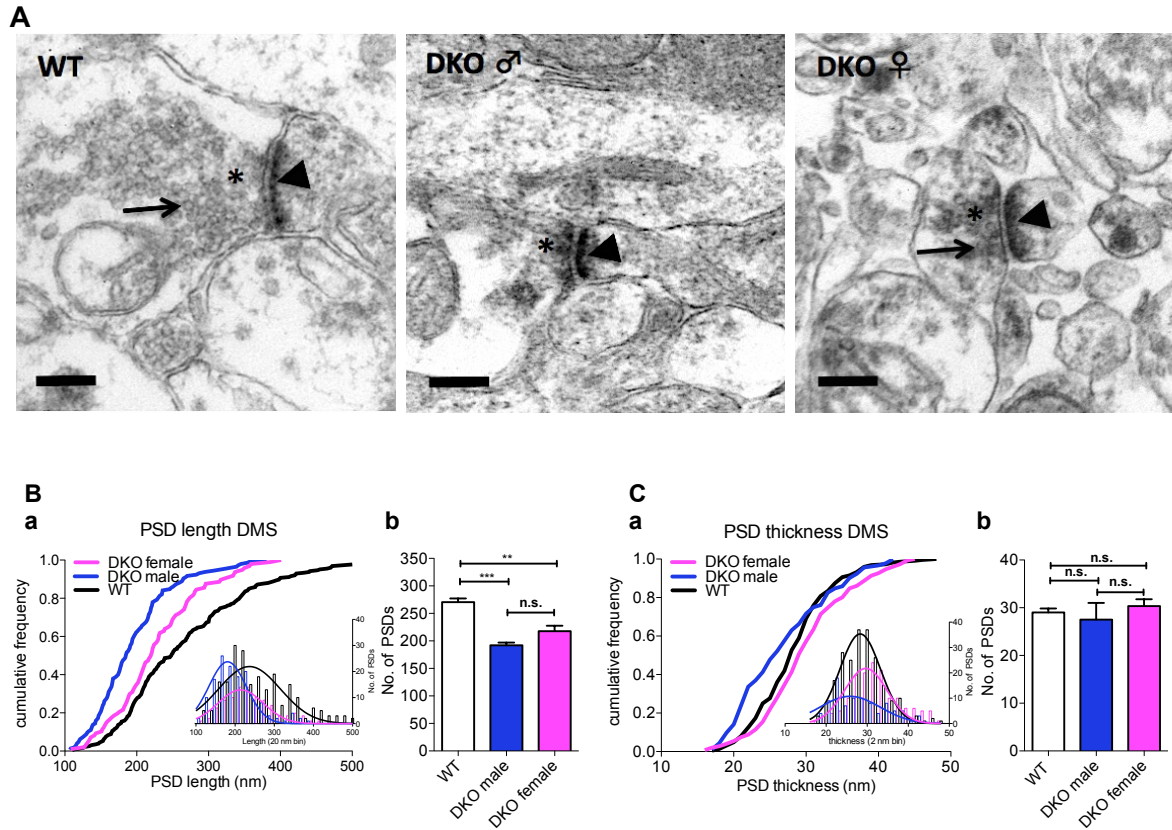


Figure 15: PSD parameters in DMS divided by gender

A: Representative electron micrographs of synapses in the dorsomedial striatum (DMS) of WT (wild-type) (left image) and DKO (*ProSAP1/Shank2*^{-/-}*ProSAP2/Shank3*^{-/-} double-knockout) mice; male (middle image) female (right image); 80.000x magnification; arrowheads: PSDs; arrows: presynaptic vesicles; asterisks: active zone; scale bar: 200 nm.

B and C: PSD (postsynaptic density) length and thickness in the DMS divided by gender **a** Data are presented as cumulative frequency plots; insets reveal Gaussian curves of the data; **b:** Mean + s.e.m of the data. **B a:** PSD length distribution of synapses in DMS; N=570 PSDs, n=6 WT mice (black line), n=3 male DKO mice (blue line), n=3 female DKO mice (magenta line). **b** mean + s.e.m of the PSD length. The PSD length was significantly reduced in male DKO mice; ***p < 0.001 calculated with two-tailed t-test; significant reduction of PSD length in female DKO mice compared to WT mice; **p < 0.01 calculated with two-tailed t-test. White bar: WT mice: 270.20 nm ± 5.33 nm, blue bar: male DKO mice: 201.70 nm ± 10.09 nm and magenta bar: female DKO mice: 217.70 nm ± 9.87 nm; **C a:** PSD thickness distribution of synapses in the DMS; N=567 PSDs, n=6 WT mice (black line), n=3 male DKO mice (blue line), n=3 female DKO mice (magenta line). **b:** mean + s.e.m of the PSD thickness. White bar: WT mice: 29.17 nm ± 0.70 nm, blue bar: male DKO mice: 27.67 nm ± 2.03 nm and magenta bar: female DKO mice: 30.33 nm ± 1.45 nm. No significant changes in PSD thickness neither between WT mice and male DKO mice, nor WT mice compared to female DKO mice in the DMS; n.s.: p > 0.05 two-tailed t-test. No significant alterations between male DKO and female DKO mice neither in PSD length nor in PSD thickness were obvious.

3.1.2 Dorsolateral Striatum

3.1.2.1 Pooled sexes

The PSD ultrastructure was analyzed in the dorsolateral striatum (DLS) of *ProSAP1/Shank2* and *ProSAP2/Shank3* double-knockout (DKO) mice and age-matched wild-type controls.

In a low magnification of 25.000x the PSD density was measured. In an area of 35.8 μm^2 , an average amount of 8.5 synapses was counted in DKO mice and 7.6 synapses in WT mice (Figure 16). No significant changes of the overall amount of PSDs have been observed.

With a greater magnification of 80.000x the width of the synaptic cleft as well as the PSD length and thickness were measured. The width of the synaptic cleft of both DKO and WT mice lied in a range between 15 nm and 24 nm. The mean value of DKO mice was measured by 20.4 nm, WT mice showed a mean value of 19.6 nm. The width of the synaptic cleft was not significantly changed in DKO mice ($p=0.26$) (Figure 17 B a and b).

The size of PSDs, however, differed among the genotypes. A highly significant reduction of 24.2 % of the PSD length in DKO mice was measured ($p<0.0001$). While WT mice had an average PSD length of 282.8 nm with a value distribution between 130 nm and 710 nm, DKO mice had smaller PSDs with a mean value of 214.4 nm with the smallest PSD at 105 nm and the largest PSD at 445 nm (Figure 17 C a and b). The PSD thickness did also significantly differ in DKO mice compared to WT controls (Figure 17 D a and b) ($p=0.0064$). DKO mice showed a mean PSD thickness of 26.6 nm ranging from 12 to 43 nm, whereas WT mice revealed a mean thickness of 30.6 nm ranging in size from 20-50 nm. Furthermore the PSD volumes were reduced by 50.8 % in DKO mice (Figure 17 D a and b) ($p<0.0001$).

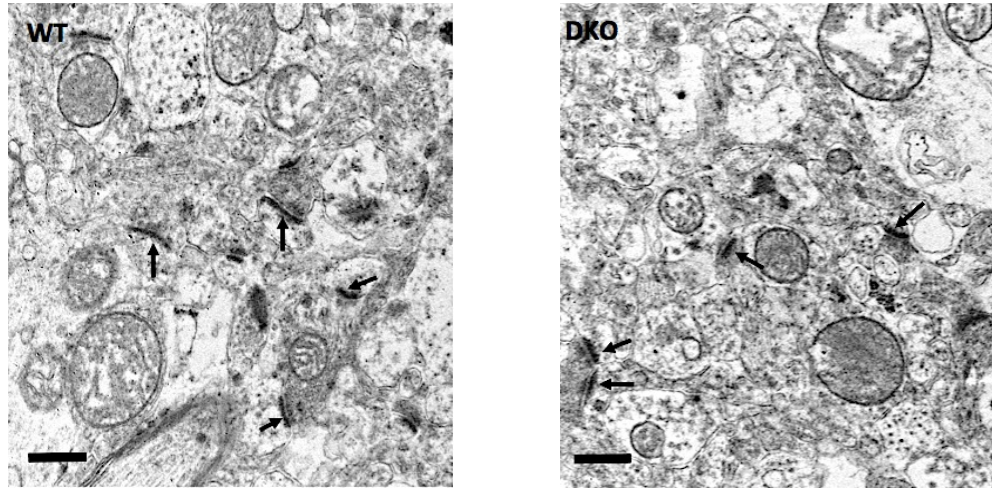
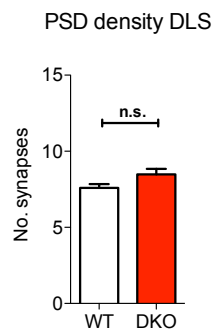
A**B**

Figure 16: PSD (postsynaptic density) density in the dorsolateral striatum. **A:** Representative electron micrographs of synapses in an area of $35.8 \mu\text{m}^2$ in the dorsolateral striatum (DLS); WT (wild-type) mouse (left image) and DKO mouse (*ProSAP1/Shank2*^{-/-} and *ProSAP2/Shank3*^{-/-} double-knockout) (right image); 25,000x magnification; arrow: exemplary synapses; scale bar: 500 nm. **B:** Mean density + s.e.m. of PSDs in the DLS; n=6 WT mice (white bar), n=6 DKO mice (red bar). No significant alteration of the PSD density observable in DKO mice (8.48 ± 0.30 PSDs per $35.8 \mu\text{m}^2$) compared to WT mice (7.59 ± 0.21 PSDs per $35.8 \mu\text{m}^2$), n.s.: $p > 0.05$ calculated with two-tailed t-test, N=600 areas, entire area analyzed: 0.02 mm^2 .

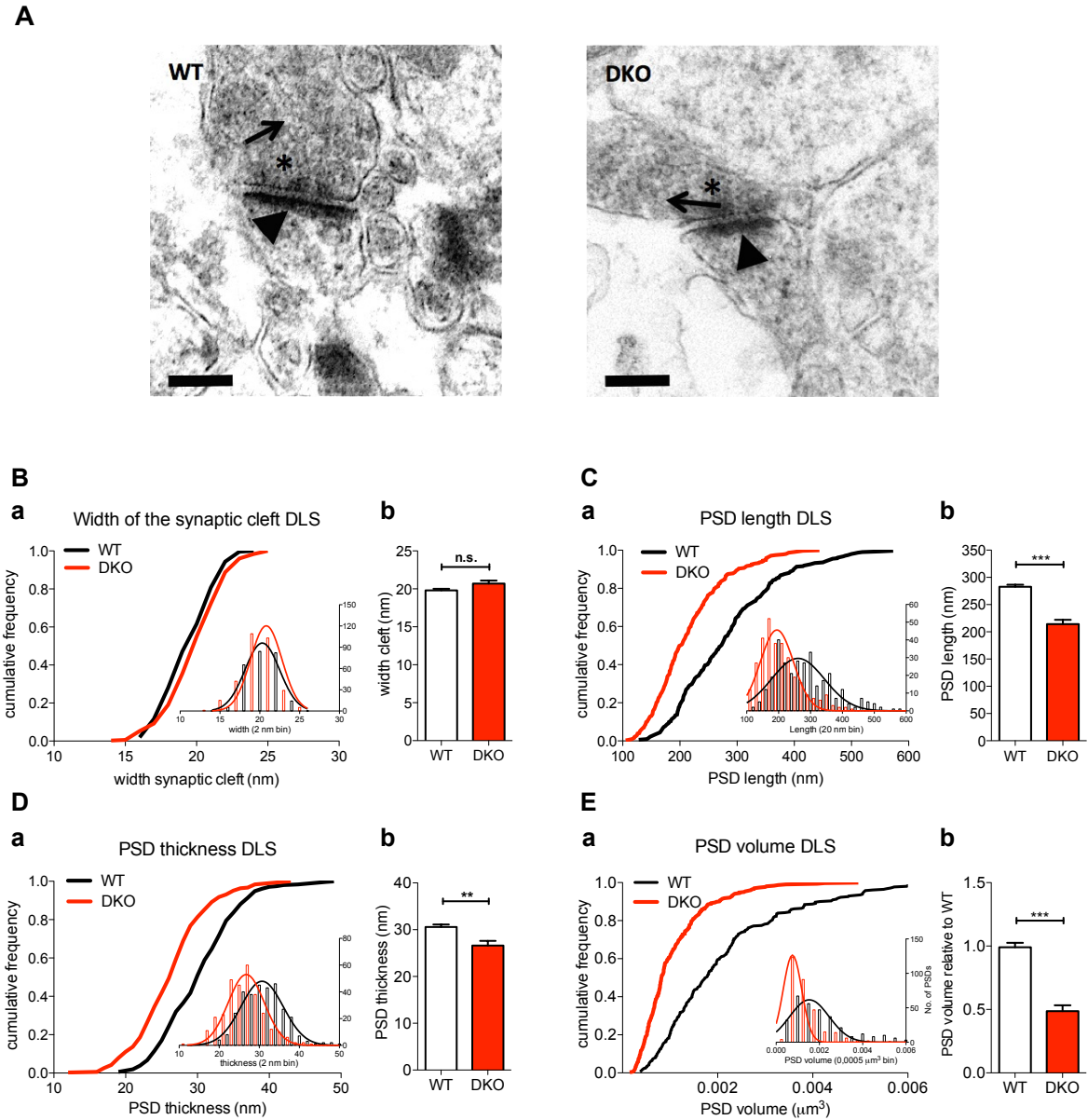


Figure 17: PSD parameters in DLS

A: Representative electron micrographs of synapses in the dorsolateral striatum (DLS); wild-type mice (WT) (left image) and DKO mice (*ProSAP1/Shank2*^{-/-} and *ProSAP2/Shank3*^{-/-} double-knockout) (right image); 80.000x magnification; arrowheads: PSDs; arrows: presynaptic vesicles; asterisks: active zone; scale bar: 200 nm.

B Width of the synaptic cleft **a:** Data is presented as cumulative frequency plot; inset reveals the frequency distribution with Gaussian curves of the data. The plot presents the distribution of the width of the synaptic cleft of all measured synapses in the DLS; N=625 synapses, n=6 wild-type mice (WT), n=6 DKO mice; Data in **b:** Mean width of synaptic cleft + s.e.m.; n=6 WT mice (white bar) 19.60 nm ± 0.25 nm and n=6 DKO mice (red bar) 20.40 nm ± 0.51 nm. The width of synaptic cleft of DKO mice revealed no significant alteration compared to WT mice; n.s.: p > 0.05 calculated with two-tailed t-test.

C, D and E: PSD length, thickness and volume **a:** Data are presented as cumulative frequency plots; insets reveal the frequency distributions with Gaussian curves of the data; **b:** Mean + s.e.m of the data. **C a:** PSD length distribution of synapses in the DLS; N=625 PSDs, n=6 WT (black line), n=6 DKO (red line). **b:** Mean + s.e.m of the PSD length, WT: 282.80 nm ± 3.65 nm (white bar), DKO: 214.40 nm ± 7.63 nm (red bar). The PSD length in DKO mice was significantly reduced; ***p < 0.0001 calculated with two-tailed t-test. **D a:** PSD thickness distribution of synapses in the DLS, N=618 PSDs, n=6 WT (black line), n=6 DKO (red line). **b:** Mean + s.e.m of the PSD thickness, WT: 30.57 nm ± 0.55 nm (white bar), DKO: 26.62 nm ± 1.01 nm (red bar). The PSD thickness was significantly reduced in DKO mice; **p < 0.0064 calculated with two-tailed t-test. **E a:** PSD volume distribution of synapses in the DLS, N=618 PSDs, n=6 WT, n=6 DKO mice. Data in **b:** Mean PSD volume + s.e.m. of all measured synapses relative to WT; n=6 WT (black bar) mice and n=6 DKO mice (red bar). A significant reduction of the PSD volume was detected in DKO mice; ***p < 0.001 calculated with two-tailed t-test.

3.1.2.2 Male and female DKO mice compared to WT mice

The PSD parameters were analyzed according by gender and revealed following results. Equal to the pooled analysis, no significant changes of the overall amount of PSDs in a defined area of $35.8 \mu\text{m}^2$ was observed between WT mice (7.7 synapses per $35.8 \mu\text{m}^2$), male DKO (7.9 synapses per $35.8 \mu\text{m}^2$) ($p=0.48$) and female DKO mice (8.6 synapses per $35.8 \mu\text{m}^2$) ($p=0.05$) could be seen (Figure 18).

Concerning the PSD parameters, both male and female DKO mice were affected similarly compared to WT mice and no gender specific effects were seen. In male DKO mice a significant PSD length reduction of 26.7% was measured ($p=0.0003$), with values ranging between 105 nm and 415 nm and a mean of 207 nm . In female DKO mice the PSD length was significantly reduced by 21.7% ($p<0.0001$), while all values lied between 116 nm and 445 nm with a mean of 221 nm (Figure 19 B a and b). No significant difference with respect to the PSD length was measured between male and female DKO mice ($p=0.41$). As described above, the PSD thickness was altered in DKO mice, this was due to a significant reduction of the PSD thickness in both sexes. While male DKO mice suffered from a significant PSD thickness reduction of 18.1% ($p=0.0036$), the PSD thickness of female DKO mice was reduced by 7.7% ($p=0.028$). Here, male DKO mice showed a value distribution of $12\text{-}42 \text{ nm}$ with a mean of 25 nm , whereas the values measured in female DKO mice ranged between 18 and 43 nm with a mean PSD thickness of 28 nm (Figure 19 C a and b). No significant changes between male and female DKO mice concerning the PSD thickness were obvious ($p=0.11$).

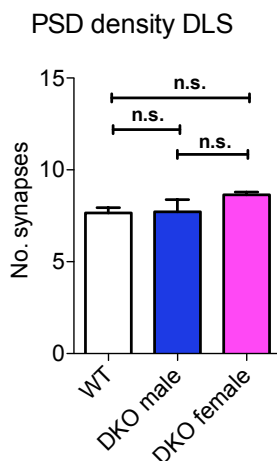


Figure 18: Mean density + s.e.m. of PSDs (postsynaptic density) in the dorsolateral striatum (DLS) of male and female DKO mice (*ProSAP1/Shank2*^{-/-}-*ProSAP2/Shank3*^{-/-} double-knockout) in an area of $35.8 \mu\text{m}^2$. No significant alteration was observable in PSD density of male DKO mice (blue bar) (7.98 ± 0.46 PSDs per $35.8 \mu\text{m}^2$) and female DKO mice (magenta bar) (8.65 ± 0.15 PSDs per $35.8 \mu\text{m}^2$) compared to WT mice (wild-type) (white bar) (7.64 ± 0.24 PSDs per $35.8 \mu\text{m}^2$), n.s.: $p > 0.05$ two-tailed t-test, $N=600$ areas, entire area 0.02 mm^2 , $n=6$ WT mice, $n=3$ male DKO mice, $n=3$ female DKO mice.

A

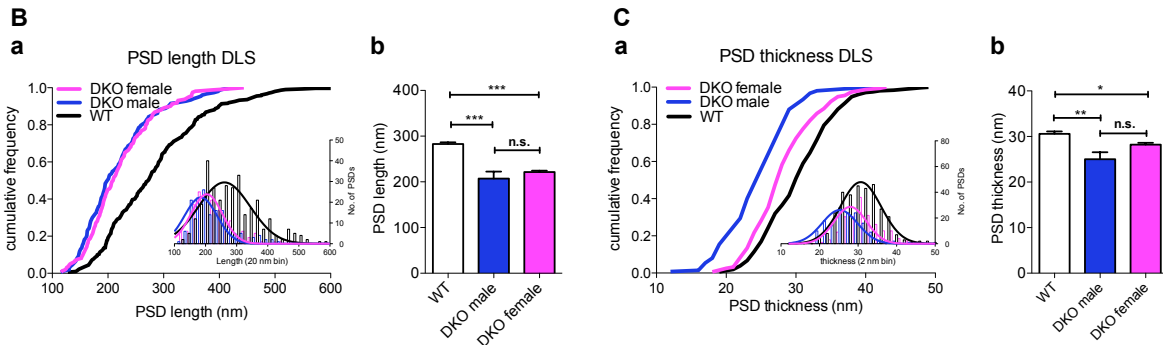
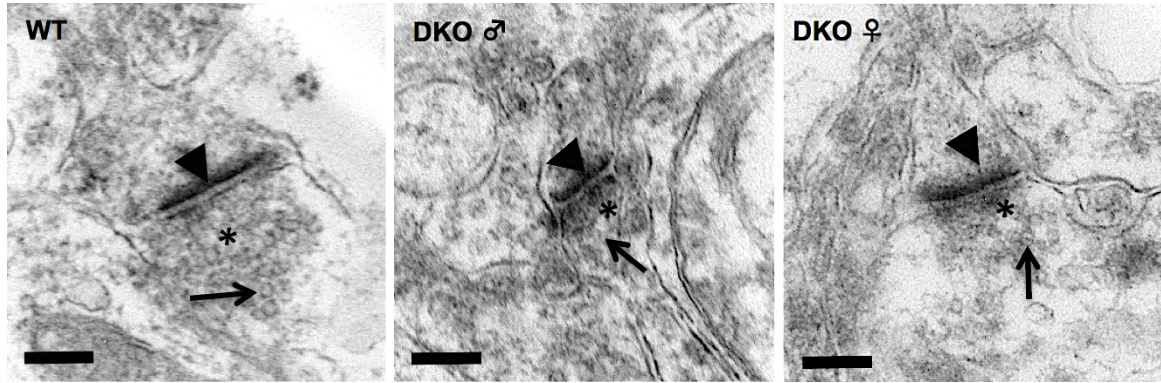


Figure 19: PSD parameters in DLS divided by gender

A: Representative electron micrographs of synapses in the dorsolateral striatum (DLS) of WT (wild-type) (left image), male (middle image) and female (right image) DKO mice (*ProSAP1/Shank2*^{-/-}*ProSAP2/Shank3*^{-/-} double-knockout); 80.000x magnification; arrowheads: PSDs; arrows: presynaptic vesicles; asterisks: active zone; scale bar: 200 nm.

B and C: PSD (postsynaptic density) length and thickness in the DLS divided by gender **a** Data in are presented as cumulative frequency plots; insets reveal Gaussian curves of the data; **b:** Mean + s.e.m of the data. **B a:** PSD length distribution of synapses in DLS; N=564 PSDs, n=6 WT mice (black line), n=3 male DKO mice (blue line), n=3 female DKO mice (magenta line). **b** mean + s.e.m of the PSD length. The PSD length was significantly reduced in male DKO mice; **p < 0.001 calculated with two-tailed t-test; significant reduction of PSD length in female DKO mice compared to WT mice; **p < 0.01 calculated with two-tailed t-test. White bar: 282.80 nm ± 3.65 nm, blue bar: male DKO mice: 207.30 nm ± 15.22 nm and magenta bar: female DKO mice: 221.40 nm ± 3.04 nm; **C a:** PSD thickness distribution of synapses in the DLS; N=618 PSDs, n=6 WT mice (black line), n=3 male DKO mice (blue line), n=3 female DKO mice (magenta line). **b:** mean + s.e.m of the PSD thickness. White bar: WT mice: 30.57 nm ± 0.55 nm, blue bar: male DKO mice: 25.03 nm ± 1.54 nm and magenta bar: female DKO mice: 28.22 nm ± 0.40 nm. The PSD thickness was significantly reduced in male DKO mice **p < 0.01 and female DKO mice *p < 0.01 calculated with two-tailed t-test.

3.1.3 Hippocampus CA1

3.1.3.1 Pooled sexes

The PSD ultrastructure was analyzed in the hippocampal CA1 region of *ProSAP1/Shank2* and *ProSAP2/Shank3* double-knockout mice and age-matched wild-type controls. The analysis showed following parameter line-up.

The PSD density was measured in a magnification of 25.000x. DKO mice showed an average count of 15.5 synapses per $35.8 \mu\text{m}^2$ and WT mice had 14.4 synapses within the same area. No significant changes of the overall amount of PSDs between DKO and WT mice were measured ($p=0.29$) (Figure 20).

The width of the synaptic cleft, PSD length and thickness were evaluated in a greater magnification of 80.000x.

The mean synaptic clefts of both genotypes were measured by 20 nm, ranging in the size from 16 – 24 nm. The width of the synaptic cleft did not significantly differ among the genotypes ($p=0.11$). (Figure 21 B a and b).

The size of the PSDs, however, varied among the strains. The evaluation revealed a highly significant alteration of the PSD length in DKO mice compared to WT mice ($p<0.0001$). While the mean PSD length in DKO mice was measured by 182.3 nm, with values ranging from 90 and 325 nm, WT mice showed an average PSD length of 224.8 nm, with values being in the range from 120 and 410 nm. DKO mice showed a PSD length reduction of 18.9 % compared to WT mice (Figure 21 C a and b).

The investigation of the PSD thickness revealed no significant alteration between DKO and WT mice ($p=0.16$). The values of both genotypes ranged between 18 nm and 45 nm, with DKO mice showing a mean of 27.2 nm and 28.1 nm in WT controls (Figure 21 D a and b).

The PSD volumes, calculated by means of the PSD length and thickness, showed a significant reduction of 37.2 % in DKO mice ($p<0.0001$) (Figure 21 E a and b).

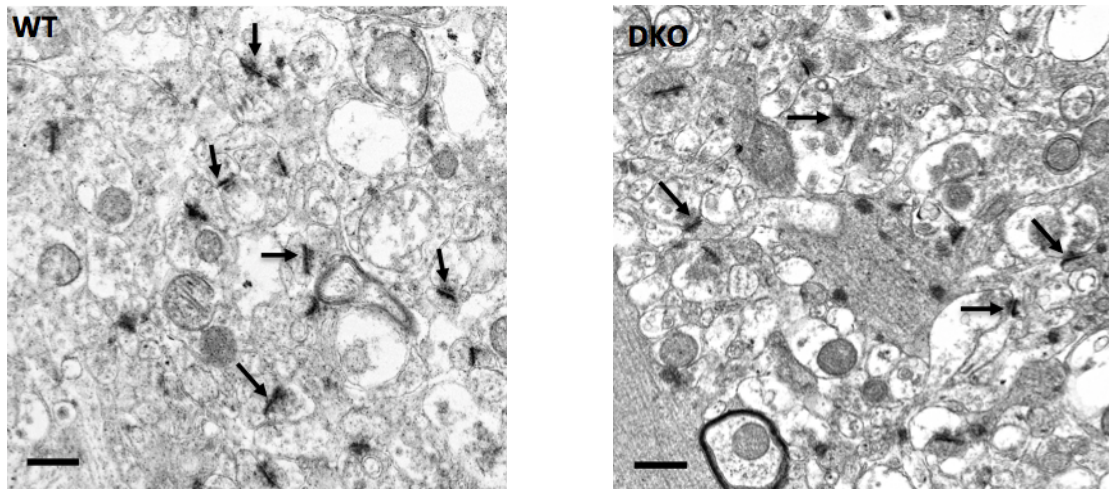
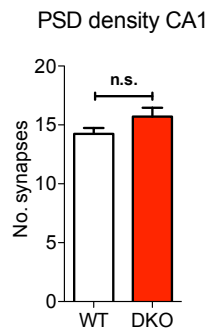
A**B**

Figure 20: PSD (postsynaptic density) density in the CA1 (Cornu Ammonis 1) area of the hippocampus. **A:** Representative electron micrographs of synapses in an area of $35.8 \mu\text{m}^2$ in the CA1 area; WT (wild-type) mouse (left image) and DKO mouse (*ProSAP1/Shank2*^{-/-} and *ProSAP2/Shank3*^{-/-} double knockout) (right image); 25.000x magnification; arrows: exemplary synapses; scale bar: 500 nm. **B:** Mean density + s.e.m. of PSDs in CA1; n=4 WT mice (white bar), n=6 DKO mice (red bar). No significant alteration was observed in the PSD density of DKO mice (15.47 ± 0.66 PSDs per $35.8 \mu\text{m}^2$) compared to WT mice (14.47 ± 0.41 PSDs per $35.8 \mu\text{m}^2$), n.s.: $p > 0.05$ calculated with two-tailed t-test, N=500 areas, entire area analyzed: 0.02 mm^2 .

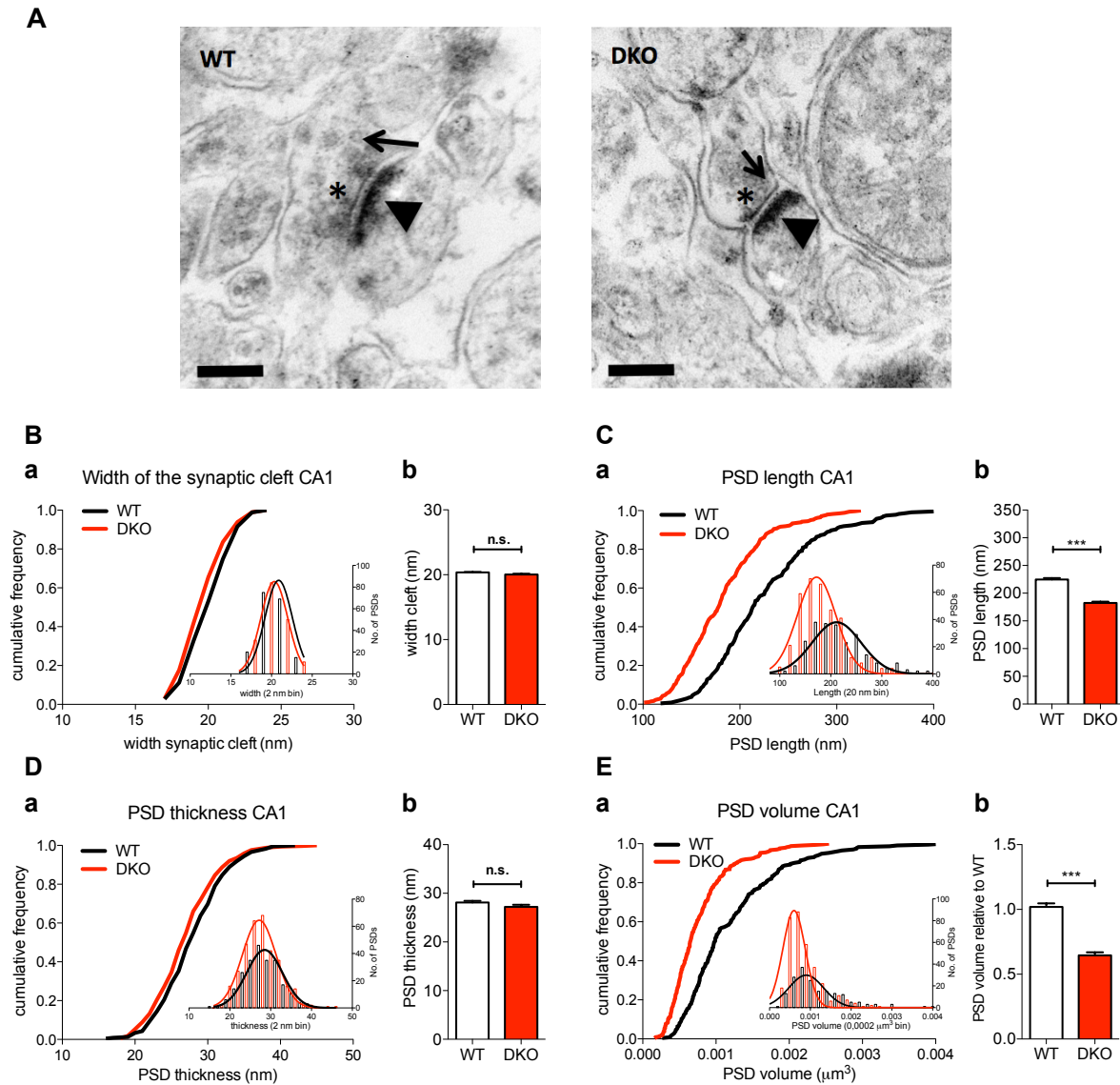


Figure 21: PSD parameters in CA1

A: Representative electron micrographs of synapses in the CA1 (Cornu Ammonis 1) area of the hippocampus; WT mouse (wild-type) (left image) and DKO mouse (*ProSAP1/Shank2^{-/-}* and *ProSAP2/Shank3^{-/-}* double-knockout) (right image); 80.000x magnification; arrowheads: PSDs; arrows: presynaptic vesicles; asterisks: active zone; scale bar: 200 nm.

B: Width of the synaptic cleft **a:** Data is presented as cumulative frequency plot; inset reveals the frequency distribution with Gaussian curves of the data. The plot presents the distribution of the width of the synaptic cleft of all measured synapses in the CA1 area; N=531 synapses, n=4 WT mice, n=6 DKO mice. **b:** Mean width of the synaptic cleft + s.e.m. of all measured synapses; WT mice (white bar) 20.36 nm ± 0.08 nm and DKO mice (red bar) 19.99 nm ± 0.06 nm. No significant alteration of the width of synaptic cleft was detected in DKO; n.s.: $p > 0.05$ calculated with two-tailed t-test.

C, D and E: PSD length and thickness **a:** Data are presented as cumulative frequency plots; insets reveal the frequency distributions with Gaussian curves of the data; **b:** Mean + s.e.m. of the data. **C a:** PSD length distribution of synapses in CA1; N=531 PSDs, n=4 WT (black line), n=6 DKO (red line). **c:** Mean + s.e.m. of the PSD length, WT: 224.80 nm ± 2.64 nm (white bar), DKO: 182.30 nm ± 2.49 nm (red bar). A significant reduction of PSD length in DKO mice was detected; *** $p < 0.001$ calculated with two-tailed t-test; **D a:** PSD thickness distribution of synapses in CA1 N=520 PSDs. **b:** Mean + s.e.m. of the PSD thickness, WT: 28.13 nm ± 0.32 nm (white bar), DKO: 27.20 nm ± 0.43 nm (red bar). The PSD thickness was not significantly altered in DKO mice; n.s.: $p > 0.05$ calculated with two-tailed t-test. **E a:** PSD volume distribution of synapses in CA1; N=520 PSDs, n=4 WT mice, n=6 DKO mice. **b:** Mean PSD volume + s.e.m. of all measured synapses relative to WT mice; n=4 WT (white bar) and n=6 DKO mice (red bar). A highly significant reduction of the PSD volume in DKO mice was found; *** $p < 0.001$ calculated with two-tailed t-test.

3.1.3.2 Male and female DKO mice compared to WT mice

The PSD ultrastructure in CA1 was further analysed by investigating differences between male and female DKO mice compared to WT mice and provided the following results.

No significant changes of the overall amount of PSDs was observed between female DKO (16.2 synapses per 35.8 μm^2) ($p=0.07$) or male DKO mice (14.7 synapses per 35.8 μm^2) ($p=0.65$) and WT mice (Figure 22).

As already ascertained in the data combining male and female animals, both male and female DKO mice were found to have smaller PSDs. The PSD lengths of female DKO mice ranged between 91 nm and 325 nm with a mean of 187.0 nm, which resulted in a significant reduction of 16.8 % compared to WT mice ($p<0.0001$). The values of male DKO mice ranged between 101 nm and 302 nm with a mean of 177.7 nm, resulting in a significant reduction of 20.1 % compared to WT mice ($p<0.0001$) (Figure 23 B a and b). However, no significant alterations of the PSD length were obvious between male DKO mice and female DKO mice ($p=0.51$).

The PSD thickness being unaffected in DKO mice in general was even confirmed by the gender based comparison. The value distribution of the PSD thickness in both male and female DKO mice offered a range between 18 and 45 nm with a mean of 27.5 nm in female DKO and 27.0 nm in male DKO mice (Figure 23 C a and b).

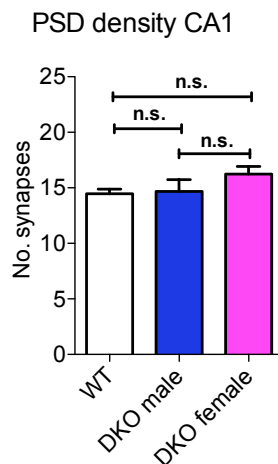


Figure 22: Mean density + s.e.m. of PSDs (postsynaptic density) in the CA1 (Cornu Ammonis 1) area of the hippocampus of male and female DKO mice (*ProSAP1/Shank2*^{-/-}-*ProSAP2/Shank3*^{-/-} double-knockout) in an area of 35.8 μm^2 . No significant alteration was observed in the PSD density of male DKO mice (blue bar) (14.69 ± 1.06 PSDs per 35.8 μm^2) and female DKO mice (magenta bar) (16.25 ± 0.68 PSDs per 35.8 μm^2) compared to WT mice (wild-type) (white bar) (14.47 ± 0.41 PSDs per 35.8 μm^2), n.s.: $p > 0.05$ two-tailed t-test, N=500 areas, entire area 0.02 mm², n=4 WT mice, n=3 male DKO mice, n=3 female DKO mice.

A

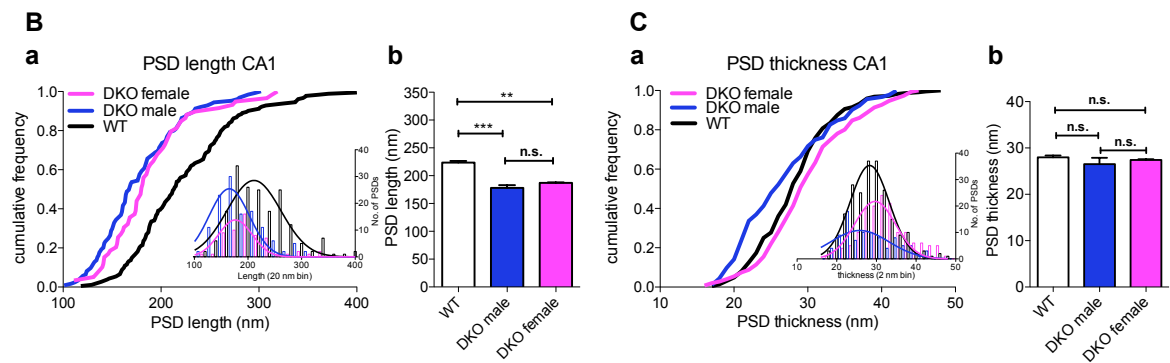
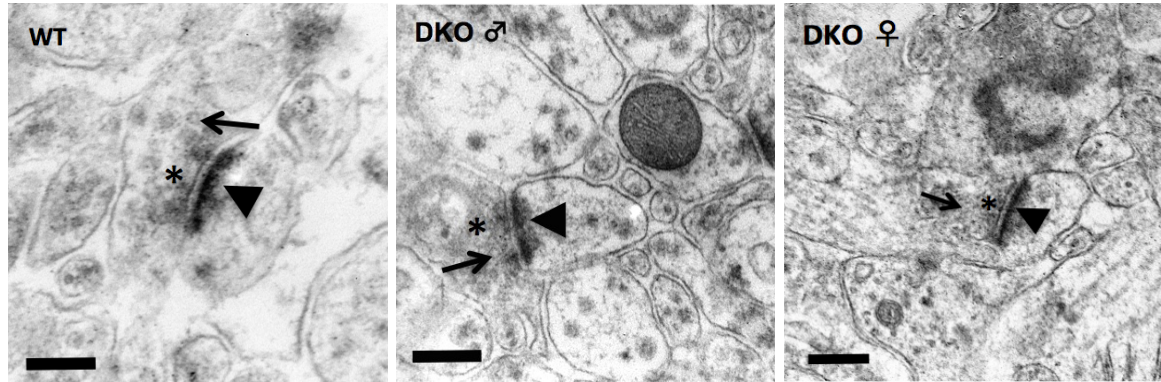


Figure 23: PSD parameters in CA1 divided by gender

A: Representative electron micrographs of synapses in the CA1 (Cornu Ammonis 1) area of the hippocampus of WT (wild-type) (left image), male (middle image) and female (right image) DKO mice (*ProSAP1/Shank2*^{-/-} - *ProSAP2/Shank3*^{-/-} double-knockout); 80.000x magnification; arrowheads: PSDs; arrows: presynaptic vesicles; asterisks: active zone; scale bar: 200 nm.

B and C: PSD (postsynaptic density) length and thickness in CA1 analysed by gender **a** Data are presented as cumulative frequency plots; insets reveal Gaussian curves of the data; **b**: Mean + s.e.m of the data. **B a:** PSD length distribution of synapses in CA1; N=531 PSDs, n=4 WT mice (black line), n=3 male DKO mice (blue line), n=3 female DKO mice (magenta line). **b** mean + s.e.m of the PSD length. The PSD length was significantly reduced in male DKO mice; ***p < 0.001 calculated with two-tailed t-test; significant reduction of PSD length in female DKO mice compared to WT mice; ***p < 0.001 calculated with two-tailed t-test. White bar: WT mice: 224.80 nm ± 2.46 nm, blue bar: male DKO mice: 177.70 nm ± 2.91 nm and magenta bar: female DKO mice: 187.70 nm ± 1.00 nm; **C a:** PSD thickness distribution of synapses in CA1; N=520 PSDs, n=4 WT mice (black line), n=3 male DKO mice (blue line), n=3 female DKO mice (magenta line). **b**: mean + s.e.m of the PSD thickness. White bar: WT mice: 28.13 nm ± 0.32 nm, blue bar: male DKO mice: 27.00 nm ± 0.93 nm and magenta bar: female DKO mice: 27.47 nm ± 0.17 nm. No significant changes in PSD thickness neither between WT mice and male DKO mice, nor between WT mice compared to female DKO mice in CA1 were found; n.s.: p > 0.05 two-tailed t-test. No significant alterations between male DKO and female DKO mice neither in PSD length nor in PSD thickness were observed.

3.1.4 Hippocampus CA3

3.1.4.1 Pooled sexes

The PSD ultrastructure was analyzed in the hippocampal CA3 region of *ProSAP1/Shank2* and *ProSAP2/Shank3* double-knockout mice and age-matched wild-type controls.

Unlike the previously analyzed brain regions, the PSDs per mossy fiber bouton, instead of the overall PSD density have been counted in the CA3 region in a magnification of 25.000x. DKO mice and WT mice showed 9.8 synapses per mossy fiber bouton. The PSD density did not significantly differ between the genotypes ($p=0.99$) (Figure 24).

With a greater magnification of 80.000x, the width of the synaptic cleft as well as the PSD length and thickness were measured.

The width of the synaptic cleft showed similar values in both DKO and WT mice, both ranging between 15 and 25 nm with a mean of 18.7 nm in DKO mice and 18.8 nm in WT mice. No significant differences were detectable ($p=0.81$) (Figure 25 B a and b).

The PSD parameters revealed not any significance for the PSD length ($p=0.10$) and the PSD thickness ($p=0.63$) between the two genotypes. The PSD length in DKO mice ranged between 49 and 359 nm with a mean value of 163.5 nm. The mean PSD length of WT mice was measured by 174.8 nm, with values ranging between 57 and 401 nm (Figure 25 C a and b).

The results for the PSD thickness showed similar, not significant, values between DKO and WT mice. The PSD thickness of DKO mice ranged between 13 and 41 nm with a mean of 25.6 nm. With a range between 14 and 40 nm and a mean of 25.4 nm, the results of WT mice showed almost equal results (Figure 25 D a and b).

Since no significant differences of the PSD length and the PSD thickness were obvious, the calculation of the PSD volume also showed no alteration among the genotypes ($p=0.19$) (Figure 25 E a and b).

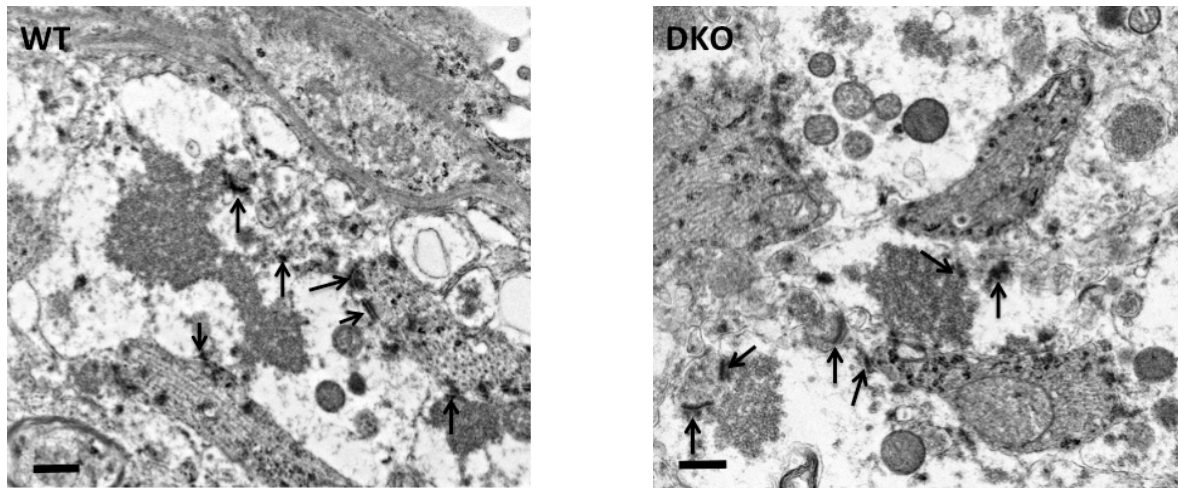
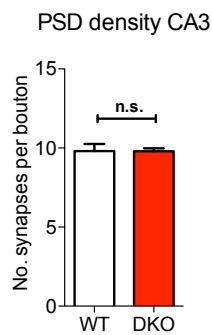
A**B**

Figure 24: PSD (postsynaptic density) density in the CA3 (Cornu Ammonis 3) area of the hippocampus. **A:** Representative electron micrographs of a mossy fiber bouton in CA3; WT mouse (wild-type) (left image) and DKO mouse (*ProSAP1/Shank2*^{-/-} and *ProSAP2/Shank3*^{-/-} double-knockout) (right image); 25.000x magnification; arrows: exemplary synapses; scale bar: 500 nm, N=500 mossy fiber boutons. **B:** Mean density + s.e.m. of PSDs of a single mossy fiber bouton. No significant alteration observable in PSD density in DKO mice (9.79 ± 0.18 PSDs per $35.8 \mu\text{m}^2$) compared to WT mice (9.80 ± 0.46 PSDs per $35.8 \mu\text{m}^2$), n.s.: $p > 0.05$ calculated with two-tailed t-test.

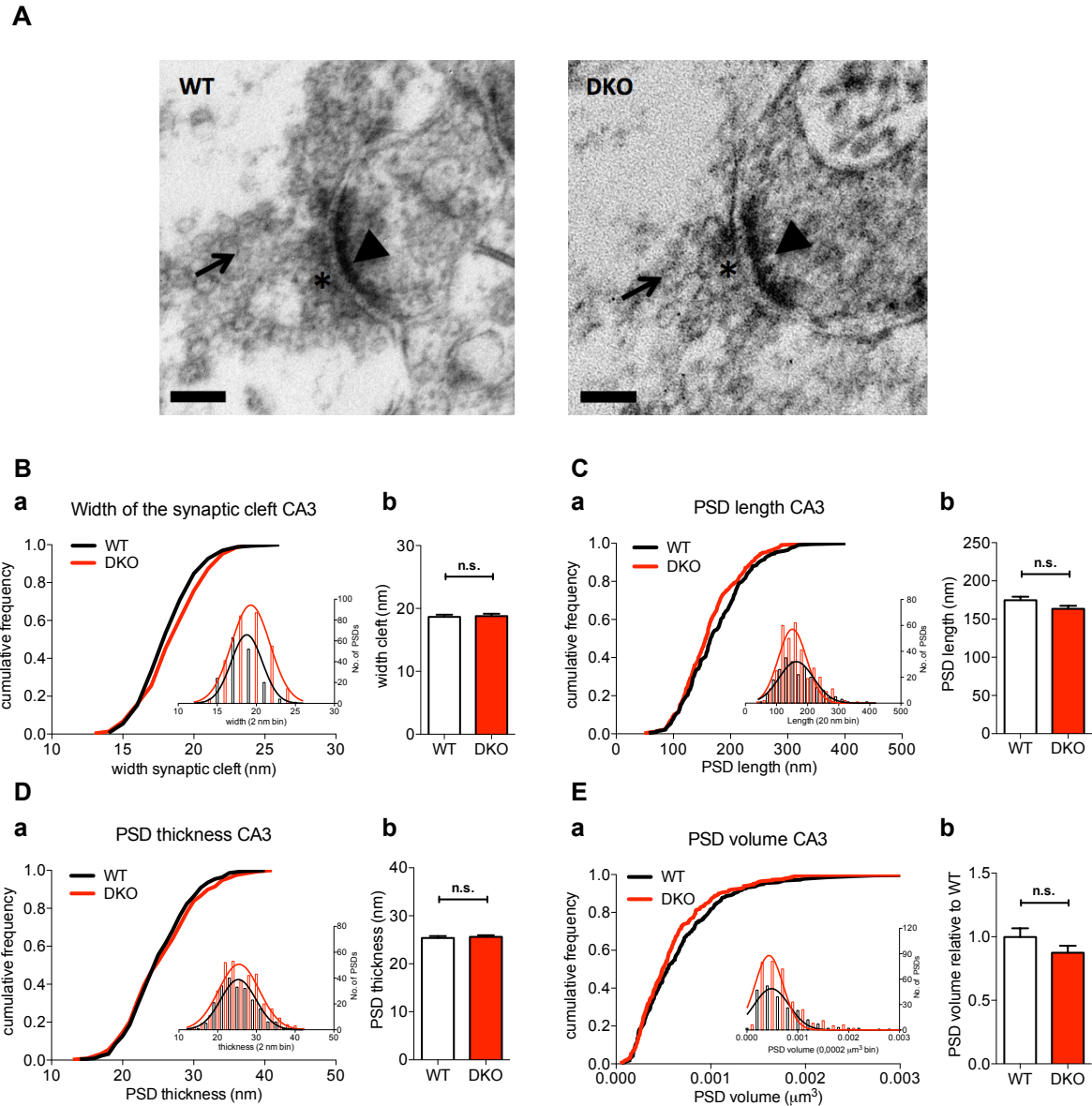


Figure 25: PSD parameters in CA3

A: Representative electron micrographs of synapses in CA3 (Cornu Ammonis 3); WT mouse (wild-type) (upper image) and DKO mouse (*ProSAP1/Shank2^{-/-}* and *ProSAP2/Shank3^{-/-}* double-knockout) (lower image); 80.000x magnification; arrowheads: PSDs; arrows: giant vesicle pool; asterisks: active zone; scale bar: 100 nm.

B: Width of the synaptic cleft density **a:** Data is presented as cumulative frequency plot; inset reveals the frequency distribution with Gaussian curves of the data. The plot presents the distribution of the width of the synaptic cleft of all measured synapses in CA3; N=566 synapses, n=4 WT mice, n=6 DKO mice. **b:** Mean width of the synaptic cleft + s.e.m. of all measured synapses, WT mice (white bar): 18.67 nm ± 0.33 nm and DKO mice (red bar): 18.80 nm ± 0.37 nm. No significant changes were detected; n.s.: p > 0.05 calculated with two-tailed t-test.

C, D, and E: PSD length, thickness and volume **a:** Data are presented as cumulative frequency plots; insets reveal the frequency distributions with Gaussian curves of the data; **b:** Mean + s.e.m of the data. **C a:** PSD length distribution of synapses in CA3; N=566 PSDs, n=4 WT (black line), n=6 DKO (red line). **b:** Mean + s.e.m of the PSD length, WT: 174.80 nm ± 4.52 nm (white bar), DKO: 163.50 nm ± 3.99 nm (red bar). PSD length was not significantly altered in DKO mice; n.s.: p > 0.05 calculated with two-tailed t-test; **D a:** PSD thickness distribution of synapses in CA3; N=549 PSDs. **b:** Mean + s.e.m of the PSD thickness, WT: 25.39 nm ± 0.38 nm (white bar), DKO: 25.63 nm ± 0.32 nm (red bar). No significant changes in PSD thickness observable; n.s.: p > 0.05 calculated with two-tailed t-test.

E a: PSD volume distribution of synapses in CA3; N=549 PSDs, n=4 WT mice, n=6 DKO mice; **b:** Mean PSD volume + s.e.m. of all measured synapses relative to WT mice; n=4 WT (white bar) and n=6 DKO mice (red bar). PSD volume was not significantly altered in DKO mice compared to WT mice; n.s.: p > 0.05 calculated with two-tailed t-test.

3.1.4.2 Male and female DKO mice compared to WT mice

The PSD parameters in the CA3 area were measured according to gender. At a single mossy fiber bouton male DKO mice possessed 10.2 synapses and female DKO mice had 9.5 synapses (Figure 26). These findings did not show any significant difference compared to WT controls (9.8 synapses per mossy fiber bouton). Furthermore, the PSD length and thickness were investigated in both male and female DKO animals. The PSD length of male DKO mice ranged between 49 and 285 nm with a mean of 159.0 nm, while the values of female DKO were in the range of 56 and 359 nm with a mean of 168.0 nm (Figure 27 B a and b). This parameter revealed no significant change in male DKO ($p=0.08$) and female DKO mice ($p=0.36$) compared to WT mice.

The PSD thickness in male DKO mice ranged between 13 and 49 nm with a mean of 25.1 nm, while female DKO mice showed a PSD thickness distribution of 15-41 nm and a mean value of 26.2 nm (Figure 27 C a and b). No significant changes were calculated between male DKO and WT mice ($p=0.62$), as well as female DKO mice and WT mice ($p=0.22$).

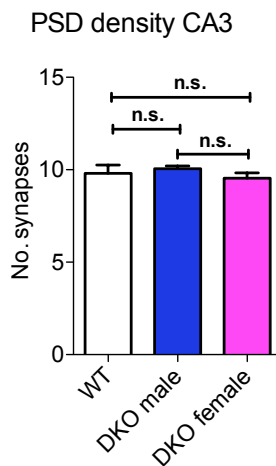


Figure 26: Mean density + s.e.m. of PSDs (postsynaptic density) in the CA3 (Cornu Ammonis 3) area of the hippocampus of male and female DKO mice (*ProSAP1/Shank2*^{-/-} *ProSAP2/Shank3*^{-/-} double-knockout) in an area of 35.8 μm^2 . No significant alteration was observed in PSD density of male DKO mice (blue bar) (10.2 ± 0.10 PSDs per 35.8 μm^2) and female DKO mice (magenta bar) (9.54 ± 0.28 PSDs per 35.8 μm^2) compared to WT mice (wild-type) (white bar) (10.4 ± 0.73 PSDs per 35.8 μm^2), n.s.: $p > 0.05$ two-tailed t-test, N=500 areas, entire area 0.02 mm², n=4 WT mice, n=3 male DKO mice, n=3 female DKO mice.

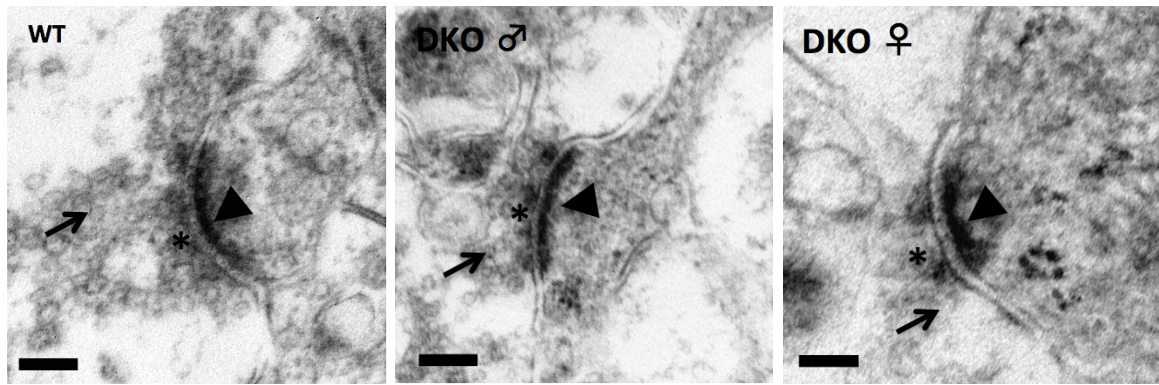
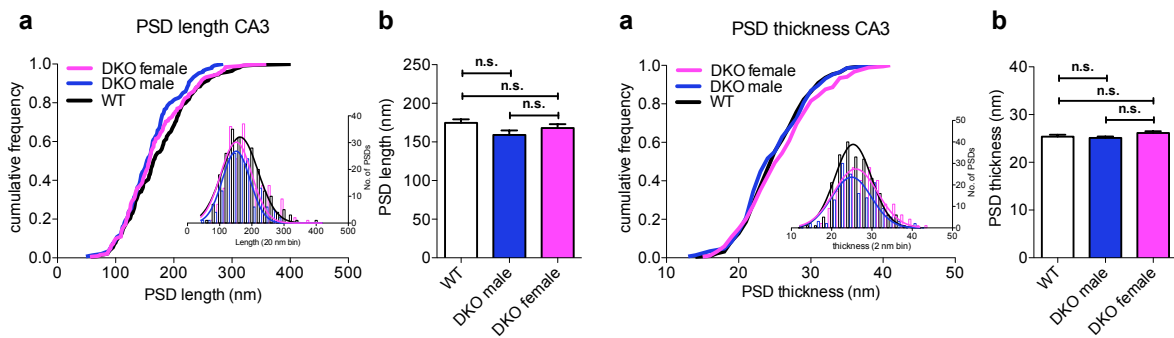
A**B**

Figure 27: Detailed analysis of PSD parameters in CA3 based on gender

A: Representative electron micrographs of synapses in the CA1 (Cornu Ammonis 3) area of the hippocampus of WT (wild-type) (left image), male (middle image) and female (right image) DKO mice (*ProSAP1/Shank2*^{-/-} - *ProSAP2/Shank3*^{-/-} double-knockout); 80.000x magnification; arrowheads: PSDs; arrows: presynaptic vesicles; asterisks: active zone; scale bar: 200 nm.

B and C: PSD (postsynaptic density) length and thickness in CA3 analysed by gender **a** Data are presented as cumulative frequency plots; insets reveal Gaussian curves of the data; **b:** Mean + s.e.m of the data. **B a:** PSD length distribution of synapses in CA3; N=566 PSDs, n=4 WT mice (black line), n=3 male DKO mice (blue line), n=3 female DKO mice (magenta line). **b** mean + s.e.m of the PSD length. The PSD length was not significantly altered in Male DKO mice; n.s. $p > 0.05$ calculated with two-tailed t-test; no significant change of PSD length in female DKO mice compared to WT mice; n.s. $p > 0.05$ calculated with two-tailed t-test. White bar: WT mice: 174.80 nm \pm 4.52 nm, blue bar: male DKO mice: 159.00 nm \pm 5.86 nm and magenta bar: female DKO mice: 168.00 nm \pm 5.00 nm; **C a:** PSD thickness distribution of synapses in CA3; N=549 PSDs, n=4 WT mice (black line), n=3 male DKO mice (blue line), n=3 female DKO mice (magenta line). **b:** mean + s.e.m of the PSD thickness. White bar: WT mice: 25.39 nm \pm 0.38 nm, blue bar: male DKO mice: 25.11 nm \pm 0.29 nm and magenta bar: female DKO mice: 26.16 nm \pm 0.38 nm. No significant changes in PSD thickness between WT mice and male DKO mice, nor between WT mice and female DKO mice in CA3; n.s.: $p > 0.05$ two-tailed t-test. No significant alterations between male DKO and female DKO mice neither in PSD length nor in PSD thickness were observed.

3.1.5 Molecular layer cerebellum

3.1.5.1 Pooled sexes

The PSD ultrastructure was analyzed in the molecular layer of the cerebellum (MLC) of *ProSAP1/Shank2* and *ProSAP2/Shank3* double-knockout mice and age-matched wild-type controls.

The PSD density was measured in a low magnification of 25.000x. In an area of 35.8 μm^2 , 8.5 PSDs were detected in DKO mice and 8.1 PSDs in WT mice. No significant alteration of the overall amount of PSDs between the two genotypes was observed ($p=0.35$) (Figure 28).

With a greater magnification of 80.000x, the PSD parameters, width of the synaptic cleft as well as the PSD length and thickness were examined.

The width of synaptic cleft of DKO mice ranged between 15 and 26 nm with a mean of 20.6 nm, similar to values measured in all brain regions examined. The width of the synaptic cleft of WT mice also ranged between 15 and 26 nm with a mean of 20.3 nm. No significant change was found, comparing the width of the synaptic cleft in DKO and WT animals ($p=0.46$) (Figure 29 B a and b).

The examination of the PSD length did not present any significance between the two genotypes ($p=0.35$). DKO mice showed a range of the PSD lengths of 114 to 575 nm with a mean of 310.3 nm. Similarly, the PSD length values of WT mice ranged between 126 and 580 nm with a mean of 313.6 nm (Figure 29 C a and b).

There were not any significant alterations of the PSD thickness in DKO compared to WT mice ($p=0.43$). The PSD thickness of DKO mice ranged in the size from 14 to 37 nm, with a mean of 22.2 nm. WT mice showed comparable results with values ranging between 10 and 37 nm and a mean of 23.3 nm (Figure 29 D a and b).

Accordingly, the calculated PSD volume was not significantly altered in DKO mice compared to WT mice ($p=0.97$) (Figure 29 E a and b).

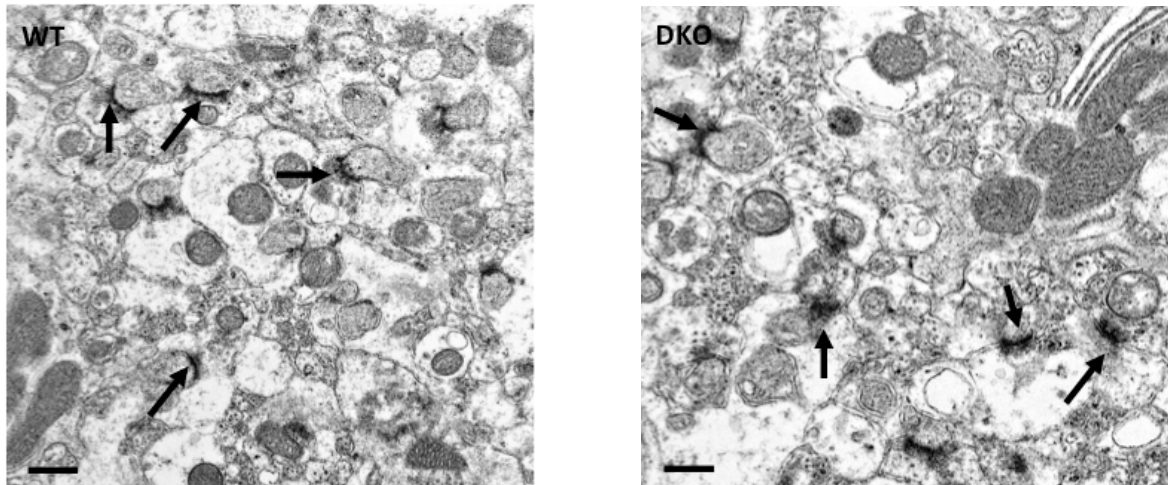
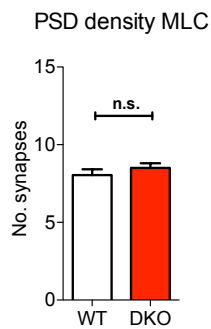
A**B**

Figure 28: PSD (postsynaptic density) density in the molecular layer of the cerebellum (MLC). **A:** Representative electron micrographs of synapses in an area of $35.8 \mu\text{m}^2$ in the MLC; WT mouse (wild-type) (left image) and DKO mouse (*ProSAP1/Shank2*^{-/-} and *ProSAP2/Shank3*^{-/-} double-knockout) (right image); 25.000x magnification; arrows: exemplary synapses; scale bar: 500 nm. **B:** Mean density + s.e.m. of PSDs in the MLC; n=6 WT mice (white bar) and n=6 DKO mice (red bar). No significant alteration observable in PSD density of DKO mice (8.50 ± 0.30 PSDs per $35.8 \mu\text{m}^2$) compared to WT mice (8.05 ± 0.37 PSDs per $35.8 \mu\text{m}^2$), n.s.: $p > 0.05$ calculated with two-tailed t-test, N=963 areas, entire area analyzed: 0.03 mm^2 .

A

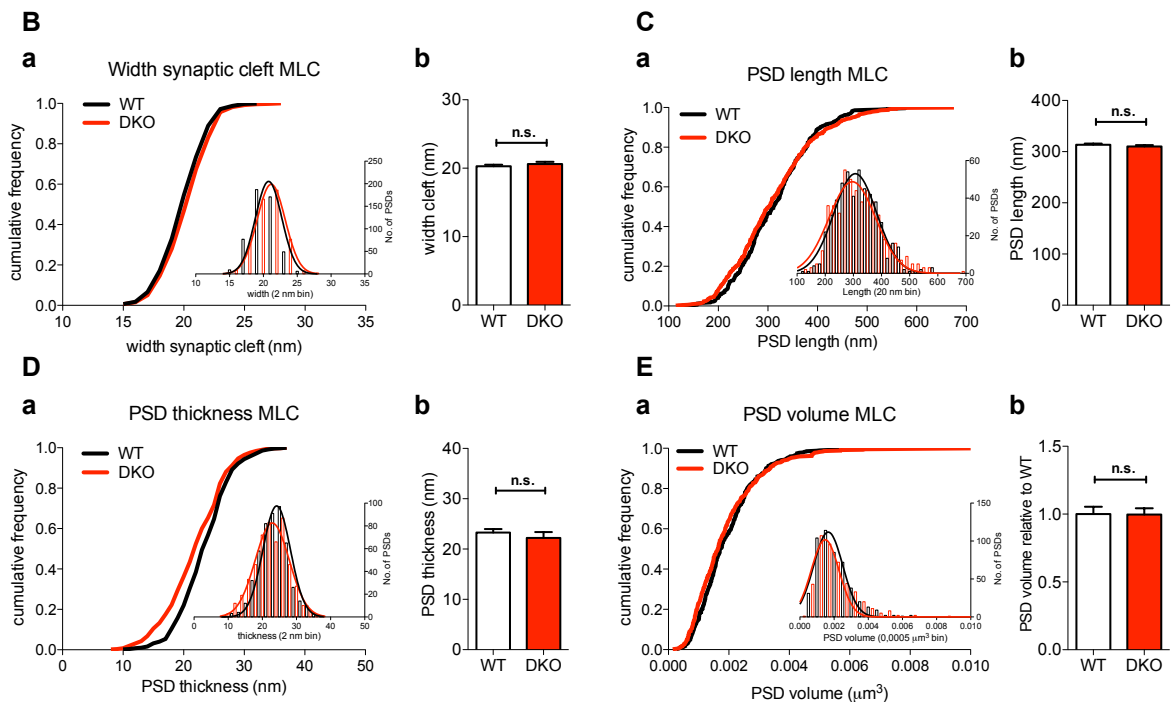
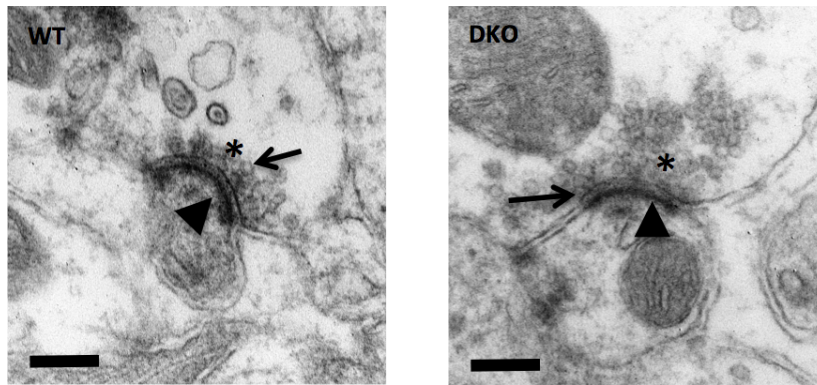


Figure 29 PSD parameters in MLC:

A: Representative electron micrographs of synapses in MLC (molecular layer of the cerebellum); WT mouse (wild-type) (upper image) and DKO mouse (*ProSAP1/Shank2*^{-/-} and *ProSAP2/Shank3*^{-/-} double-knockout) (lower image); 80,000x magnification; arrowheads: PSDs; arrows: presynaptic vesicles; asterisks: active zone; scale bar: 200 nm.

B: Width of the synaptic cleft. **a:** Data is presented as cumulative frequency plot; inset reveals the frequency distribution with Gaussian curves of the data. The plot presents the distribution of the width the synaptic cleft of all measured synapses in MLC; N=1012 synapses, n=6 WT mice, n=6 DKO mice. **b:** Mean width of the synaptic cleft + s.e.m. of all measured synapses; WT mice: 20.30 nm ± 0.21 nm (white bar) and DKO mice: 20.60 nm ± 0.34 nm (red bar). No significant alteration of the width of the synaptic cleft was observed in DKO mice; n.s.: p > 0.05 calculated with two-tailed t-test.

C, D and E: PSD length, thickness and volume. **a:** Data are presented as cumulative frequency plots; insets reveal the frequency distributions with Gaussian curves of the data; **b:** Mean + s.e.m of the data. **C a:** PSD length distribution of synapses in the MLC; N=1023 PSDs, n=6 WT (black line), n=6 DKO (red line). **b:** Mean + s.e.m of the PSD length WT: 313.60 nm ± 2.27 nm (white bar), DKO: 310.30 nm ± 8.41 nm (red bar). No significant alteration of the PSD length in DKO mice; n.s.: p > 0.05 calculated with two-tailed t-test; **D a:** PSD thickness distribution of synapses in MLC N=1008 PSDs. **b:** Mean + s.e.m of the PSD thickness, WT: 23.30 nm ± 0.67 nm (white bar), DKO: 22.20 nm ± 1.18 nm (red bar). No significant change of the PSD thickness in DKO mice; n.s.: p > 0.05 calculated with two-tailed t-test. **E a:** PSD volume distribution of synapses in MLC; N=1012 PSDs, n=6 WT mice, n=6 DKO mice. **b:** Mean PSD volume + s.e.m. of all measured synapses relative to wild-type mice; WT mice (white bar) and DKO mice (red bar). PSD volumes in DKO mice did not differ from WT mice; n.s.: p > 0.05 calculated with two-tailed t-test.

3.1.5.2 Male and female DKO mice compared to WT mice

Grouped and analysed by gender, there were no significant alterations between Male and female DKO mice compared to WT mice.

Within an area of $35.8 \mu\text{m}^2$, in male DKO mice 8.3 synapses were counted, while in female DKO mice an average of 8.6 synapses was found.

The PSD length of male DKO mice ranged between 114 nm and 568 nm with a mean of 310.2 nm. Female DKO mice showed a value distribution between 120 nm and 675 nm with a mean value of 313.6 nm. No significant alteration could be observed between male DKO and WT mice ($p=0.36$), as well as female DKO and WT mice ($p=0.99$). The corresponding PSD thickness of male DKO mice was in a range between 14 nm and 37 nm with a mean of 21.8 nm, which revealed no significant change compared to wild-type controls ($p=0.20$). The PSD thickness of female DKO mice also ranged between 14 nm and 37 nm, having a mean of 24.6 nm, showing no significant alteration ($p=0.26$). As well, no significant alterations between were found between male and female DKO mice ($p=0.05$).

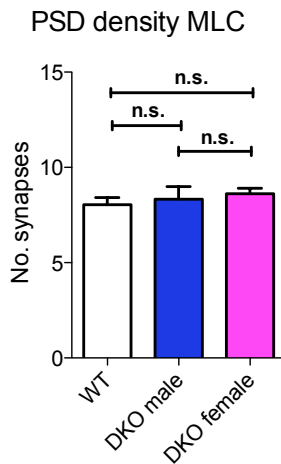
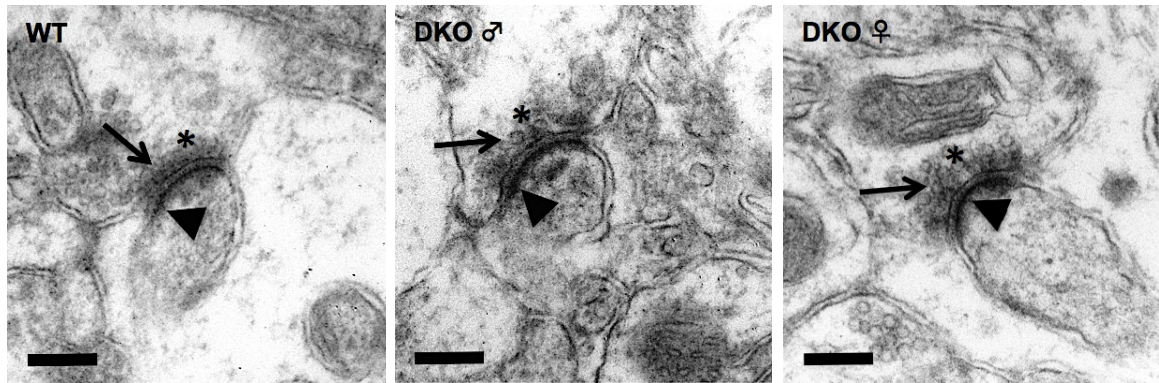
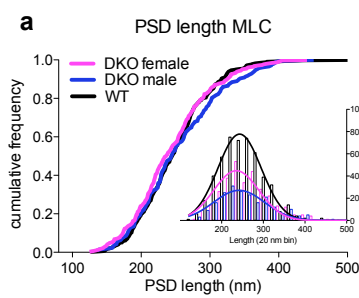
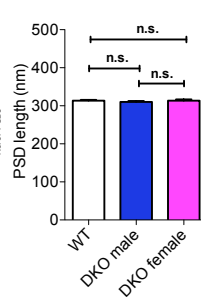
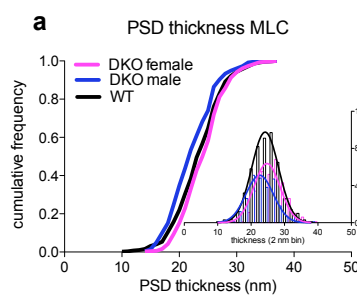
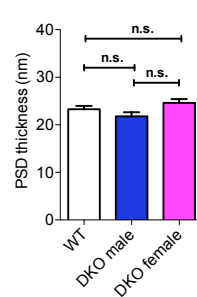


Figure 30: Mean density + s.e.m. of PSDs (postsynaptic density) in the MLC (molecular layer of the cerebellum) of male and female DKO mice (*ProSAP1/Shank2*^{-/-}-*ProSAP2/Shank3*^{-/-} double-knockout) in an area of $35.8 \mu\text{m}^2$. No significant alteration was observable in PSD density of male DKO mice (blue bar) (7.59 ± 0.75 PSDs per $35.8 \mu\text{m}^2$) and female DKO mice (magenta bar) (8.52 ± 0.55 PSDs per $35.8 \mu\text{m}^2$) compared to WT mice (wild-type) (white bar) (7.95 ± 0.64 PSDs per $35.8 \mu\text{m}^2$), n.s.: $p > 0.05$ two-tailed t-test, $N=963$ areas, entire area 0.03 mm^2 , $n=6$ WT mice, $n=3$ male DKO mice, $n=3$ female DKO mice.

A**B****b****C****b****Figure 31: PSD parameters in MLC divided by gender**

A: Representative electron micrographs of synapses in the molecular layer of the cerebellum (MLC) of WT (wild-type) (left image) and DKO (*ProSAP1/Shank2*^{-/-}-*ProSAP2/Shank3*^{-/-} double-knockout) mice; male (middle image) female (right image); 80.000x magnification; arrowheads: PSDs; arrows: presynaptic vesicles; asterisks: active zone; scale bar: 200 nm.

B and C: PSD (postsynaptic density) length and thickness in the MLC divided by gender **a** Data are presented as cumulative frequency plots; insets reveal Gaussian curves of the data; **b:** Mean + s.e.m of the data. **B a:** PSD length distribution of synapses in the MLC; N=1023 PSDs, n=6 WT mice (black line), n=3 male DKO mice (blue line), n=3 female DKO mice (magenta line). **b** mean + s.e.m of the PSD length. The PSD length was not significantly altered in male DKO mice; n.s. $p > 0.05$ calculated with two-tailed t-test; no significant change of PSD length in female DKO mice compared to WT mice; n.s. $p > 0.05$ calculated with two-tailed t-test. White bar: WT mice: 313.60 nm \pm 2.27 nm, blue bar: male DKO mice: 310.20 nm \pm 2.46 nm and magenta bar: female DKO mice: 313.60 nm \pm 3.37 nm; **C a:** PSD thickness distribution of synapses in the MLC; N=1012 PSDs, n=6 WT mice (black line), n=3 male DKO mice (blue line), n=3 female DKO mice (magenta line). **b:** mean + s.e.m of the PSD thickness. White bar: WT mice: 23.30 nm \pm 0.67 nm, blue bar: male DKO mice: 21.80 nm \pm 0.86 nm and magenta bar: female DKO mice: 24.60 nm \pm 0.81 nm. No significant changes in PSD thickness neither between WT mice and male DKO mice, nor WT mice compared to female DKO mice in the MLC; n.s.: $p > 0.05$ two-tailed t-test. No significant alterations between male DKO and female DKO mice neither in PSD length nor in PSD thickness were obvious.

3.1.6 Granular layer cerebellum

3.1.6.1 Pooled sexes

The PSD ultrastructure was analyzed in the granular layer of the cerebellum (GLC) of *ProSAP1/Shank2* and *ProSAP2/Shank3* double-knockout (DKO) mice and age-matched wild-type controls.

In a low magnification of 25.000x the PSD density of single mossy fiber boutons were counted. An average amount of 10.4 synapses was counted in DKO mice and 9.9 synapses in WT mice. No significant change of the overall amount of PSDs per mossy fiber bouton has been observed ($p=0.07$) (Figure 32).

With a greater magnification of 80.000x, the width of the synaptic cleft, as well as the PSD length and thickness were measured.

In accordance to all examined brain regions, the width of the synaptic cleft did not differ between the genotypes ($p=0.1$). DKO mice showed a distribution of 17 and 25 nm with a mean of 20.4 nm. Similarly, WT mice ranged between 16 and 25 nm with a mean of 20.6 nm (Figure 33 B a and b).

Like hippocampal mossy fiber PSDs, the cerebellar mossy fiber PSDs were smaller than PSDs in other brain regions. Ranging between 62 and 286 nm, the PSD length of DKO mice had a mean of 140.8 nm. WT mice showed a PSD length distribution between 52 and 275 nm with a mean of 140.2 nm. No significances have been found within the PSD length between DKO and WT mice ($p=0.74$) (Figure 33 C a and b).

Furthermore, the PSD thickness did not significantly alter as well among the genotypes ($p=0.39$). While the PSD thickness of DKO animals ranged between 16 and 39 nm with a mean of 25.3 nm, WT mice showed similar results with a value distribution of 17 and 45 nm and a mean of 25.9 nm (Figure 33 D a and b)

The calculation of the PSD volume revealed no significant alteration between DKO and WT mice ($p=0.45$) (Figure 33 E a and b).

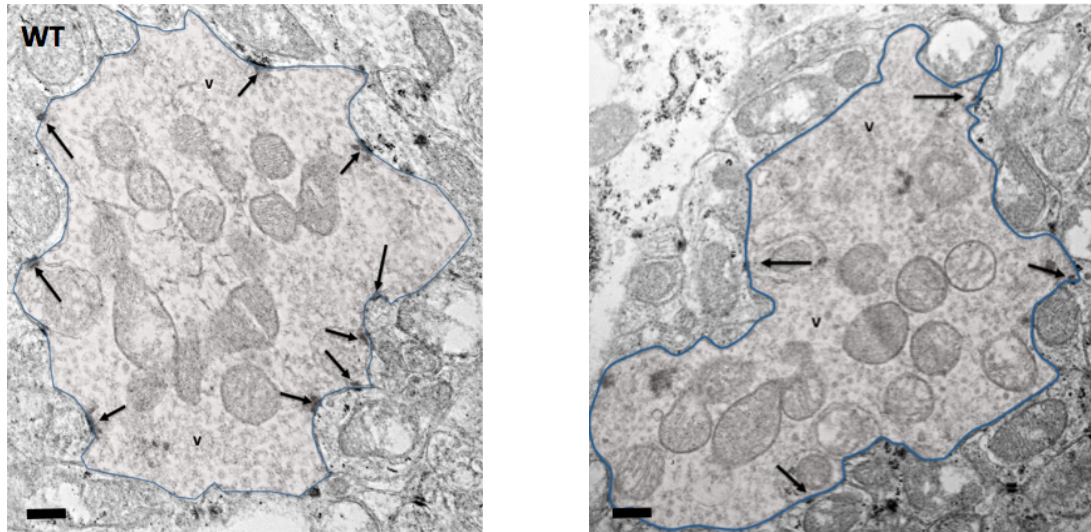
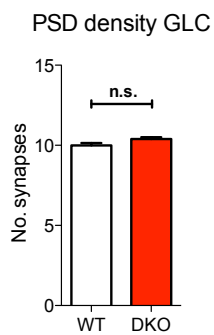
A**B**

Figure 32: PSD (postsynaptic density) density in the granular layer of the cerebellum (GLC). **A:** Representative electron micrographs of synapses in an area of $35.8 \mu\text{m}^2$ in the GLC; WT mouse (wild-type) (left image) and DKO mouse (*ProSAP1/Shank2^{-/-}* and *ProSAP2/Shank3^{-/-}* double-knockout) (right image), asterisks: PSDs, v: vesicle pool, blue line outlines a mossy fiber bouton; 25.000x magnification; arrows: exemplary synapses; scale bar: 500 nm. **B:** Mean density + s.e.m. of PSDs per mossy fiber bouton in the GLC n=6 WT (white bar) and n=6 DKO mice (red bar), N=600 boutons. No significant alteration observable in PSD density of DKO mice (10.38 ± 0.11 PSDs per mossy fiber bouton) compared to WT mice (9.99 ± 0.16 PSDs per mossy fiber bouton), n.s.: $p > 0.05$ calculated with two-tailed t-test.

A

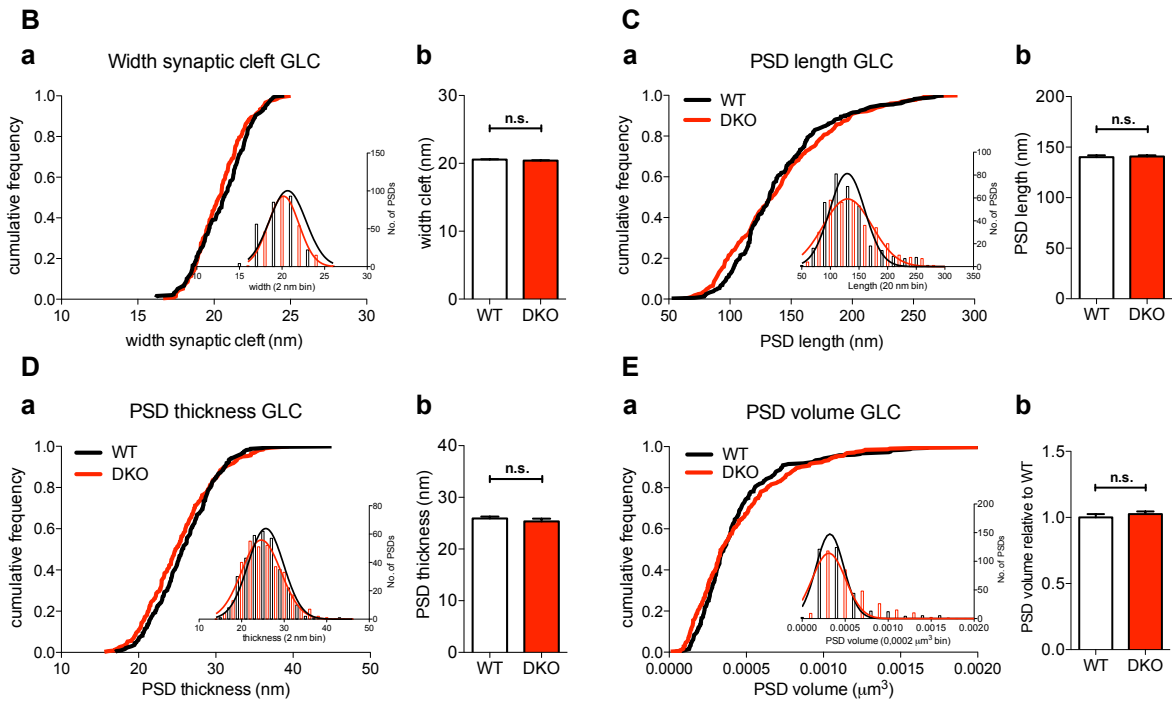
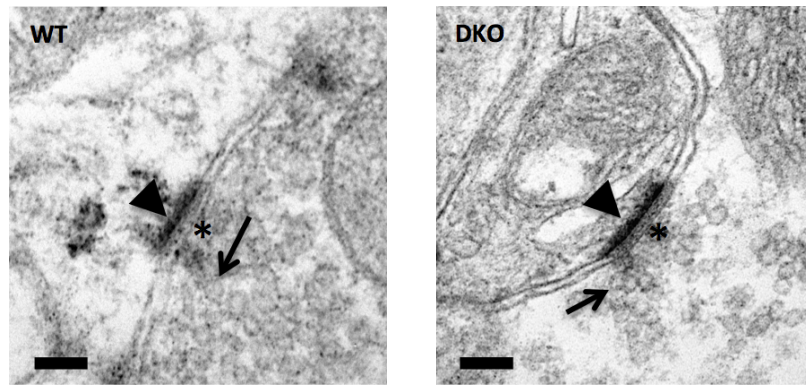


Figure 33: PSD parameters in GLC

A: Representative electron micrographs of synapses in GLC (granular layer of the cerebellum); WT mouse (wild-type) (left image) and DKO mouse (*ProSAP1/Shank2*^{-/-} and *ProSAP2/Shank3*^{-/-} double-knockout) (right image); 80,000x magnification; arrowheads: PSDs; arrows: presynaptic vesicles; asterisks: active zone; scale bar: 100 nm.

B: Width of the synaptic cleft. **a:** Data is presented as cumulative frequency plot; inset reveals the frequency distribution with Gaussian curves of the data. The plot presents the distribution of the width of the synaptic cleft of all measured synapses in GLC; N=655 synapses, n=6 WT mice, n=6 DKO mice; **b:** Mean width of the synaptic cleft + s.e.m. of all measured synapses; n=6 WT mice (white bar) 20.55 nm ± 0.05 nm and n=6 DKO mice (red bar) 20.41 nm ± 0.05 nm. No significant alteration of the width of the synaptic cleft in DKO mice; n.s.: p > 0.05 calculated with two-tailed t-test.

C, D and E: PSD length, thickness and volume. **a:** Data are presented as cumulative frequency plots; insets reveal the frequency distributions with Gaussian curves of the data; **b:** Mean + s.e.m of the data. **C a:** PSD length distribution of synapses in the GLC; N=655 PSDs, n=6 WT (black line), n=6 DKO (red line). **b:** Mean + s.e.m of the PSD length, WT: 140.20 nm ± 1.71 nm (white bar), DKO: 140.80 nm ± 1.08 nm (red bar). No significant alteration in the PSD length observed in DKO mice; n.s.: p > 0.05 calculated with two-tailed t-test; **D a:** PSD thickness distribution of synapses in GLC; N=556 PSDs. **b:** Mean + s.e.m of the PSD thickness, WT: 25.92 nm ± 0.35 nm (white bar), DKO: 25.34 nm ± 0.55 nm (red bar). No significant changes in PSD thickness in DKO mice; n.s.: p > 0.05 calculated with two-tailed t-test. **E a:** PSD thickness distribution of synapses in GLC; N=655 PSDs, n=6 WT mice, n=6 DKO mice. **b:** mean PSD volume + s.e.m. of all measured synapses relative to wild-type mice; WT mice (white bar) and DKO mice (red bar). There was no significant alteration of the PSD volume of DKO mice; n.s.: p > 0.05 calculated with two-tailed t-test.

3.1.6.2 Male and female DKO mice compared to WT mice

The PSD parameters in the GLC were further measured according to gender. A single mossy fiber bouton revealed 10.4 synapses in male DKO mice and 10.3 synapses in female DKO mice (Figure 34). These results did not show any significant alterations compared to WT animals (9.9 synapses per mossy fiber bouton). Furthermore, the PSD length and thickness were investigated in both male and female DKO animals. The PSD length of male DKO mice were in a range of 62 and 223 nm with a mean of 138.0 nm, while the values of female DKO ranged between 66 and 286 nm with a mean of 141.6 nm (Figure 35 B a and b). No significant difference was analysed in male DKO ($p=0.91$) and female DKO mice ($p=0.59$) compared to WT mice concerning this PSD parameter.

The PSD thickness in male DKO mice ranged between 16 and 39 nm with a mean of 24.7 nm, whereas female DKO mice had a PSD thickness value distribution of 17 to 39 nm and a mean value of 25.9 nm (Figure 27 C a and b). No significant differences were measured between male DKO and WT mice ($p=0.13$), as well as female DKO mice and WT mice ($p=0.93$).

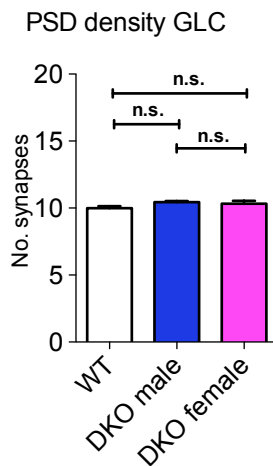
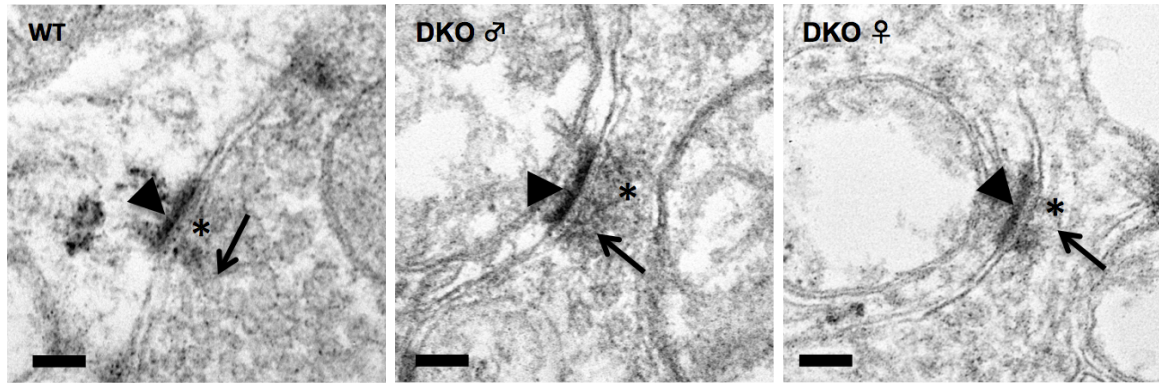
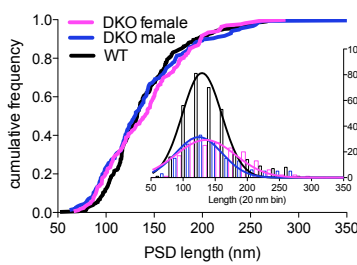
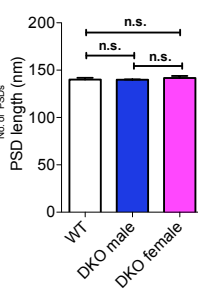
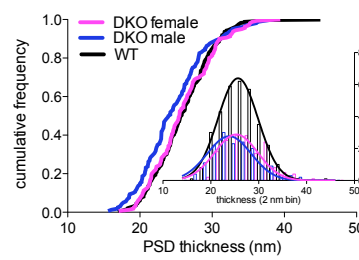
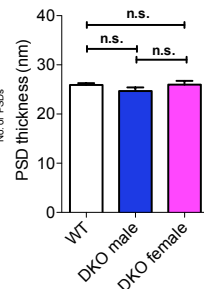


Figure 34: Mean density + s.e.m. of PSDs (postsynaptic density) in the GLC (granular layer of the cerebellum) of male and female DKO mice (*ProSAP1/Shank2*^{-/-}-*ProSAP2/Shank3*^{-/-} double-knockout) in an area of 35.8 μm^2 . No significant alteration was observable in PSD density of male DKO mice (blue bar) (10.44 ± 0.08 PSDs per 35.8 μm^2) and female DKO mice (magenta bar) (10.32 ± 0.22 PSDs per 35.8 μm^2) compared to WT mice (wild-type) (white bar) (9.99 ± 0.16 PSDs per 35.8 μm^2), n.s.: $p > 0.05$ two-tailed t-test, N=600 areas, entire area 0.02 mm², n=6 WT mice, n=3 male DKO mice, n=3 female DKO mice.

A**B****a** PSD length GLC**b****C****a** PSD thickness GLC**b****Figure 31: PSD parameters in GLC divided by gender**

A: Representative electron micrographs of synapses in the granular layer of the cerebellum (GLC) of WT (wild-type) (left image) and DKO (*ProSAP1/Shank2*^{-/-}-*ProSAP2/Shank3*^{-/-} double-knockout) mice; male (middle image) female (right image); 80.000x magnification; arrowheads: PSDs; arrows: presynaptic vesicles; asterisks: active zone; scale bar: 200 nm.

B and C: PSD (postsynaptic density) length and thickness in the GLC divided by gender **a** Data are presented as cumulative frequency plots; insets reveal Gaussian curves of the data; **b:** Mean + s.e.m of the data. **B a:** PSD length distribution of synapses in the GLC; N=655 PSDs, n=6 WT mice (black line), n=3 male DKO mice (blue line), n=3 female DKO mice (magenta line). **b** mean + s.e.m of the PSD length. The PSD length was not significantly altered in male DKO mice; n.s. $p > 0.05$ calculated with two-tailed t-test; no significant change of PSD length in female DKO mice compared to WT mice; n.s. $p > 0.05$ calculated with two-tailed t-test. White bar: WT mice: $140.20 \text{ nm} \pm 1.71$, blue bar: male DKO mice: $139.90 \text{ nm} \pm 0.45 \text{ nm}$ and magenta bar: female DKO mice: $141.80 \text{ nm} \pm 2.19 \text{ nm}$; **C a:** PSD thickness distribution of synapses in the GLC; N=655 PSDs, n=6 WT mice (black line), n=3 male DKO mice (blue line), n=3 female DKO mice (magenta line). **b:** mean + s.e.m of the PSD thickness. White bar: WT mice: $25.92 \text{ nm} \pm 0.35 \text{ nm}$, blue bar: male DKO mice: $24.69 \text{ nm} \pm 0.73 \text{ nm}$ and magenta bar: female DKO mice: $25.98 \text{ nm} \pm 0.77 \text{ nm}$. No significant changes in PSD thickness neither between WT mice and male DKO mice, nor WT mice compared to female DKO mice in the GLC; n.s.: $p > 0.05$ two-tailed t-test. No significant alterations between male DKO and female DKO mice neither in PSD length nor in PSD thickness were observed.

3.1.7 DKO synopsis

Table 11: Synopsis of evaluated brain regions. DMS (dorsomedial striatum), DLS (dorsolateral striatum), CA1 (Cornu Ammonis 1), CA3 (Cornu Ammonis 3), MLC (molecular layer cerebellum), GLC (granular layer cerebellum)
significant results printed bold; * synapses per bouton in CA3, WT (wild-type), DKO (double knockout), PSD (Postsynaptic density)

	DMS			DLS			CA1			CA3			MLC			GLC		
	WT	DKO	%	WT	DKO	%	WT	DKO	%	WT	DKO	%	WT	DKO	%	WT	DKO	%
PSD length (nm)	270,2	209,7	22,4	282,8	214,4	24,1	224,8	182,3	18,9	174,8	163,5	6,5	313,6	310,3	1,1	140,2	140,8	0,4
PSD thickness (nm)	29,2	29,0	2,4	30,6	26,6	13,1	28,1	27,2	3,2	25,4	25,6	0,8	23,3	22,2	4,9	25,8	25,3	2,3
Width synaptic cleft (nm)	19,6	20,4	4,1	19,8	20,7	4,5	20,4	20,0	2	18,7	18,8	0,5	20,3	20,6	1,5	20,5	20,4	0,5
PSD volume (relative)	1	0,586	41,4	1	0,492	50,8	1	0,645	35,5	1	0,875	12,5	1	1	0	1	1,02	2,0
PSD Density/ 35,8µm ²	8,1	7,9	2,5	7,6	8,5	10,5	11,8	15,5	10,5	9,8*	9,8*	0	8,5	8,1	4,7	10,0*	10,4*	4,0

3.2 PSD ultrastructure of *ProSAP1/Shank2* knockout mice compared to wild-type mice in the dorsolateral striatum

Unlike double-knockout mice, a single knockout of *ProSAP1/Shank2* had no consequences on the ultrastructure in *ProSAP1/Shank2* knockout mice in the dorsolateral striatum.

Within an area of $35.8 \mu\text{m}^2$ WT mice had an average amount of 8.8 synapses, in DKO mice 8.9 synapses were counted. This result had no significant effect ($p=0.91$).

The width of the synaptic cleft in DKO, as well as WT mice ranged from 15 to 25 nm with a mean of 20.0 nm in DKO mice and 20.3 nm in WT mice ($p=0.64$) (Figure 36).

Disparately to double-knockout results, the PSD length did not show any significance ($p=0.77$). In DKO mice, the PSD lengths ranged between 124 and 572 nm with a mean of 268 nm, the values of WT mice ranged in the size from 125 and 501 nm, with a mean of 271.5 nm (Figure 37 B a and b).

The PSD thickness was unaltered in DKO mice compared to WT mice ($p=0.99$). With a mean of 28.1 nm the PSD thickness ranged between 16 and 41 nm in DKO mice. Quite similar, WT showed values, which ranged in the size from 14 and 43 nm with a mean of 28.1 nm (Figure 37 C a and b).

Consequently, the PSD volume was not significantly altered between the genotypes ($p=0.75$) (Figure 37 E a and b)

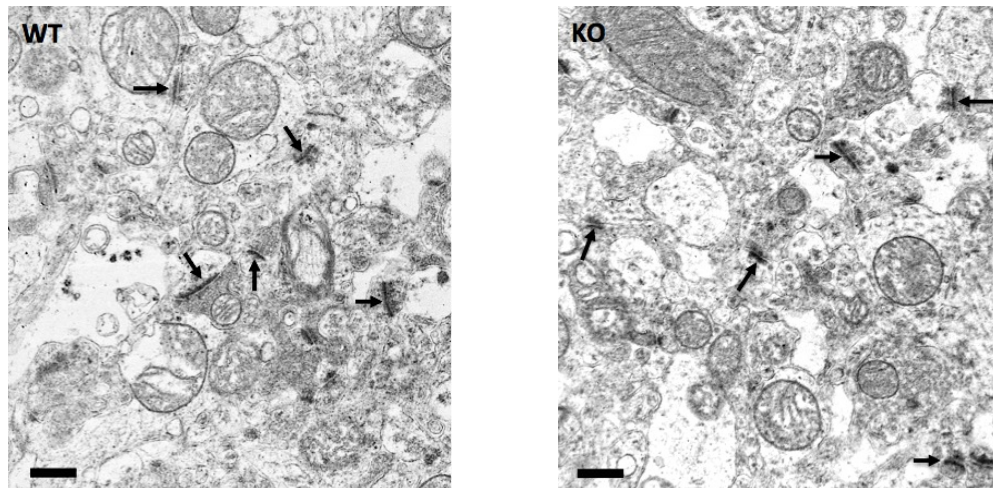
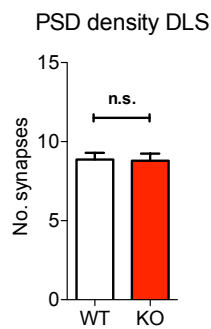
A**B**

Figure 36: PSD (postsynaptic density) density in the dorsolateral striatum (DLS). **A:** Representative electron micrographs of synapses in an area of $35.8 \mu\text{m}^2$ in the DLS; WT (wild-type) mouse (left image) and KO mouse (*ProSAP1/Shank2*^{-/-} knockout) (right image); 25.000x magnification; arrow: exemplary synapses; scale bar: 500 nm. **B:** Mean density + s.e.m. of PSDs in the DLS; n=4 WT mice (white bar), n=4 KO mice (red bar). No significant alteration observable of the PSD density in KO mice (8.79 ± 0.45 PSDs per $35.8 \mu\text{m}^2$) compared to WT mice (8.87 ± 0.42 PSDs per $35.8 \mu\text{m}^2$), n.s.: $p > 0.05$ calculated with two-tailed t-test, N=400 areas, entire area analyzed 0.02 mm^2 .

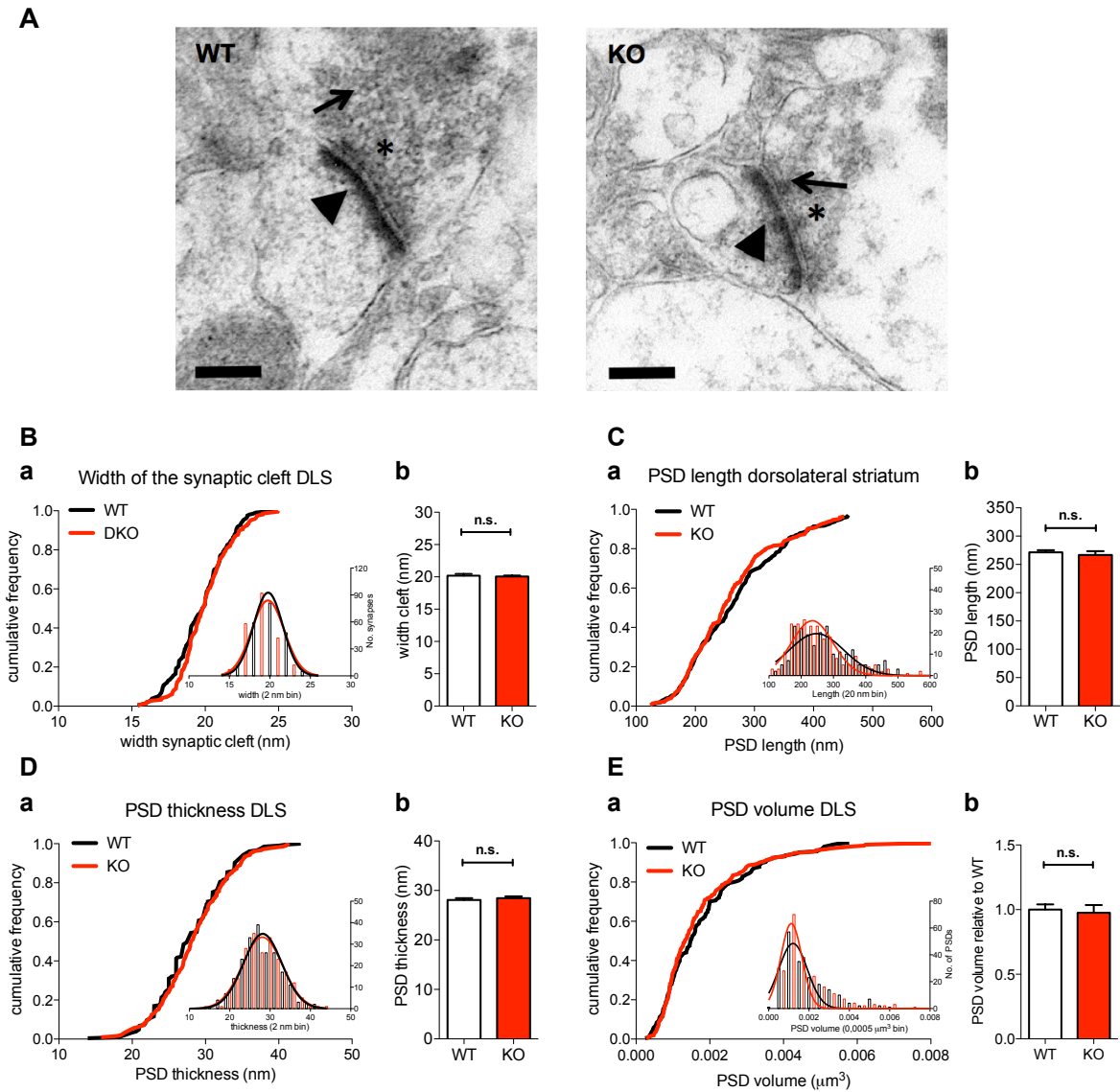


Figure 37: PSD parameters DLS

A: Representative electron micrographs of synapses in the DLS; WT (left image) and KO mice (right image); 80.000x magnification; arrowheads: PSDs; arrows: presynaptic vesicles; asterisks: active zone; scale bar: 200 nm.

B: Width of the synaptic cleft **a:** Data is presented as cumulative frequency plot; inset reveals the frequency distribution with Gaussian curves of the data. The plot presents the distribution of the width of the synaptic cleft of all measured synapses in the DLS; N=364 synapses, n=4 WT mice, n=4 KO mice; **b:** Mean width of the synaptic cleft + s.e.m.; WT mice 20.26 nm \pm 0.39 nm (white bar) and KO mice 20.04 nm \pm 0.21 nm (red bar). No significant alteration of the width of the synaptic cleft observed in KO mice compared to WT mice; n.s.: $p > 0.05$ calculated with two-tailed t-test.

C, D and E: PSD length, thickness and volume; **a** Data are presented as cumulative frequency plots; insets reveal the frequency distributions with Gaussian curves of the data; **b:** Mean + s.e.m of the data **C a:** PSD length distribution of synapses in the DLS; N=428 PSDs, n=4 WT (black line), n=4 KO (red line). **b:** Mean + s.e.m of the PSD length, WT: 271.50 nm \pm 3.59 nm (white bar), KO: 266.80 nm \pm 6.57 nm (red bar). No significant alteration of PSD length in KO mice; n.s.: $p > 0.05$ calculated with two-tailed t-test; **D a:** PSD thickness distribution in the DLS; N=416 PSDs. **b:** Mean + s.e.m of the PSD thickness, WT: 28.09 nm \pm 0.68 nm (white bar), KO: 28.44 nm \pm 0.38 nm (red bar). No significant changes in the PSD thickness of KO mice.; n.s.: $p > 0.05$ calculated with two-tailed t-test. **E a:** PSD volume distribution synapses in the DLS; N=416 PSDs, n=4 WT mice, n=4 KO mice; **b:** Mean PSD volume + s.e.m. of all measured synapses relative to WT mice; WT mice (white bar) and KO mice (red bar). No significant change of the PSD volume in KO mice compared to WT mice; n.s.: $p > 0.05$ calculated with two-tailed t-test.

3.2.2 ProSAP1/Shank2 synopsis

Table 12: Synopsis of the results evaluated in the dorsolateral striatum (DLS); PSD (postsynaptic density), WT (wild-type), KO (ProSAP1/Shank2 knockout)

	DLS		
	WT	KO	%
PSD length (nm)	271,5	266,8	1,7
PSD thickness (nm)	28,1	28,4	1,1
Width synaptic cleft (nm)	20,2	20,1	0,5
PSD volume (relative)	1	0,97	3
PSD Density/ 35,8µm ²	8,9	8,8	1,1

4. Discussion

Substantial focus in autism spectrum disorders is nowadays laid on PROSAP/SHANK due to an overall estimated mutation prevalence of 1% in this gene family in patients with ASD (autism spectrum disorders) [73]. Thus, special interest arises on synapse morphology and PSD composition of ASD-associated brain regions in *ProSAP/Shank* mutant mice. In this study, the striatum with its dorsomedial and dorsolateral part, the hippocampal CA1 and CA3 areas as well as the cortical layers of the cerebellum have been investigated. With respect to already analyzed ultrastructure in the different *ProSAP/Shank* mutant mice [56,67,85,98,113,118], the synapses of *ProSAP1/Shank2* as well as the synapses of a new mutant, *ProSAP1/Shank2–ProSAP2/Shank3*–homozygous double knockout (Schmeisser et al. unpublished), have been examined.

4.1 Alterations of the cortico-striatal synapse in the dorsomedial and dorsolateral striatum of DKO mice

The cortico-striatal synapse is the most common synapse of the neostriatum, caudate nucleus and putamen. The pyramidal cells, originating in cortical layer V, innervate medium-sized spiny neurons (MSNs) of the neostriatum. At least 90-95% of all striatal cells are MSNs [42,49]. Afferents of almost all parts of the cortex forming synapses with MSNs are of the asymmetrical, axospinous type and form the majority of all synapses within the neostriatum [60,100]. For the purpose of this study, dorsomedial synapses of the striatum were analysed in consideration of originating axons from the prefrontal and limbic circuits. These synapses were opposed to synapses with respect to the sensorimotor neocortex being localized in the dorsolateral striatum [34].

Like synapses in other brain regions, there is a direct correlation between the spine head volume and the PSD size of cortico-striatal synapses. Not only a morphological correlate, but also a functional correlate has to be seen. Hence, the geometry of the synapse is supposed to be the expression of its efficiency [7,79,97,116].

In this study the width of the synaptic cleft was analyzed in wild-type mice. Within these two striatal sub-regions, all animals revealed similar values comparable with the data in the literature, which is 20 nm [110]. Furthermore, the average synapse within the dorsomedial striatum had a PSD length of 270 nm and a PSD thickness of 29 nm. PSDs in the dorsolateral striatum showed slightly larger average PSDs with a length of 280 nm and a PSD thickness of 30 nm. Further, these two parameters together are the two-dimensional correlates of the entire PSD volume and therefore morphologically reflect the efficiency of the synapses. In an area of $35.8 \mu\text{m}^2$ approximately 8 of such synapses were located within the dorsomedial and the dorsolateral striatum, respectively.

Contributing to the most important functions of the dorsomedial striatum, behavioral versatility, mental control of comportment as well as the managing of action and consequence, it is crucial for these synapses to maintain the above measured parameters within a distinct range to allow precise control of these functions. Such a maintenance should further be found in the dorsolateral striatum, regulating its main function, the stimulus-response learning [34].

The importance of geometry and efficiency of those synapses can be demonstrated by knocking out genes, which are coding for scaffold proteins within the PSDs. In this study, both *ProSAP1/Shank2* and *ProSAP2/Shank3* were deleted. Double knockout animals show ASD-like phenotypes (Schmeisser et al. unpublished) and revealed dramatic alterations of synapses in the dorsomedial and dorsolateral striatum, which could possibly be responsible for the ASD-like phenotypes or at least contribute to these. Apart from inter-individual differences, no significant alterations were found in the overall number of PSDs in a defined area, neither in the dorsomedial, nor in the dorsolateral part of the striatum. In the dorsomedial striatum, the average PSD length was reduced by 23.3 %, while the widths of the synaptic cleft and the average thickness of the PSD did not significantly alter. By comparison, a reduction of 24.7 % of the PSD length was found in the dorsolateral striatum and the PSDs in this sub-region also showed a reduced thickness by 12.6 %, while the width of the synaptic cleft remained unchanged. Interestingly this effect was regardless of gender. Both the synapses of male and female double knockout mice had similar effects and were not significantly different. Even compared to each other, there were no significant differences.

The ultrastructural analysis of both striatal sub-regions in double knockout mice indicated a change of the synaptic morphology towards smaller synapses and dendritic spines, and thus leading to a potential loss of synaptic efficiency. Therefore it is feasible that the above-mentioned functions might not longer be fulfilled in an optimal manner. So far, as described above, it is assumed that the PSD area, and volume respectively, reflects the strength of a single synapse [7]. However, the measured data within this study might be suggestive that the proper functionality of a single synapse might presuppose a certain PSD thickness, while the PSD length on the other side might reflect the efficiency of the synapse. But this hypothesis has to be proven in further electrophysiological studies.

In addition to the *ProSAP1/Shank2* and *ProSAP2/Shank3* double knockout mouse model, in this study, the *ProSAP1/Shank2* knockout, was further analyzed with a special focus on the dorsolateral striatum. Interestingly, no significant alterations were found for neither of the measured parameters, width of the synaptic cleft, PSD density, length, thickness and volume. Considering the massive changes seen in the *ProSAP1/Shank2* and *ProSAP2/Shank3* double knockout mouse model, this raises the question, whether *ProSAP1/Shank2* proteins have a subordinate role for the geometry of synapses in the dorsolateral striatum and that, at least for the dorsolateral striatum, the ultrastructural shape of PSDs might be dependent on the presence of *ProSAP2/Shank3*. This presumption could be supported by Peça et al. in 2011, where cortico-striatal synapses in the dorsolateral striatum of *ProSAP2/Shank3* mutant mice were examined and showed a significant reduction of both PSD length and the PSD thickness [85]. Finally, in this study, no ultrastructural correlate for the autistic trait could be found in these mice, at least concerning the dorsolateral striatum

The fact that the synapses in the two striatal sub-regions, were differently affected by a *ProSAP1/Shank2* and *ProSAP2/Shank3* double knockout, suggests that this *ProSAP1/Shank2* knockout not only evokes brain region specific effects, but also unravels a sub-region specific vulnerability to altered protein levels of the synapses in the striatum of these animals.

4.2 Reduced PSD length in hippocampal CA1 synapse of DKO mice

The CA3 to CA1 Schaffer-collateral synapse, named after the Hungarian anatomist and neurologist Károly Schaffer, was a major point of focus in this study. Each CA3 pyramidal cell sends Schaffer collaterals projecting to the stratum radiatum of the CA1 region [58]. All of these axospinous connections have asymmetric synapses, which use the glutamate as neurotransmitter and are thus excitatory [50].

The size and shape of dendritic spines and their synapses underlie a broad range, including small and thin spines as well as large, mushroom-shaped spines within a single continuum [7,51]. Despite these variances, one of the parameters always remains consistent. They all share a macular shaped PSD with an average area of about $0.04 \mu\text{m}^2$ [97].

Interestingly, many correlations between spine shape, the PSD and at least the activity of the involved Schaffer-collateral synapses have been reported. Being more precise, the spine head parameters are proportional to the PSD area [53], the larger the spine head, the larger the PSD, the higher the number of included receptors, the more presynaptic vesicles and the more efficient the synapse [51,52].

Within this study, the average PSD of Schaffer-collateral synapses of wild-type mice was analysed and showed the following appearance. Like in the above-mentioned brain region, striatum, the width of the synaptic cleft is stable at approximately 20 nm. Based on the values detected in striatal synapses, the hippocampal CA1 area showed an average width of the synaptic cleft, well-fitting to the values in the literature [74]. With a total length of about 223 nm, the PSD of this type of synapse is not as large as the ones in the dorsomedial or the dorsolateral synapses. The PSDs of these synapses showed an average thickness of 28 nm, which is similar to striatal PSDs. This suggests that the general synapse has to maintain a certain thickness to ensure its survival as stated above. Compared to the dorsomedial and dorsolateral striatum, the density of PSDs in a defined area is higher within the stratum radiatum in CA1. With 14.2

synapses per $35.8 \mu\text{m}^2$ almost twice the amount of synapses within striatal regions were measured in the hippocampal CA1 region. Based on the higher amount of synapses per area, the efficiency of the entire sub-region is possibly balanced by even smaller PSDs.

The examination of this sub-region in *ProSAP1/Shank2* and *ProSAP2/Shank3* double knockout mice showed exactly an effect of the presumed morphological indicator of synaptic efficiency, the PSD length. The mean PSD length of double knockout mice was reduced by almost 20 %, while the PSD thickness remained unchanged. This leads to the assumption, that most of these synapses generally are still functional, but not as efficient as the synapses of wild-type controls. Furthermore the presumed loss of efficiency within this sub-region might also contribute to the ASD-like phenotypes observed within this mouse model (Schmeisser et al. unpublished).

With respect to a higher prevalence of ASD in male patients, possible differences between male and female double knockout mice were further investigated. Apart from higher significances of the observed alterations in double knockout male mice, there was no crucial alteration between the genders within all measured parameters. This suggests, that these parameters might probably not contribute to the bias towards males in the ASD prevalence.

Additionally, an almost significant trend towards a higher PSD density in the stratum radiatum of CA1 in double knockout animals may point towards an attempt of this sub-region to compensate the lower synaptic strength of single synapses. Thus, the amount of PSDs might be increased to potentially counteract a loss of efficiency. As well, this statement has to be proven by electrophysiological examinations.

The CA1 region with its Schaffer-collateral synapses represents the most commonly analysed sub-region of ultrastructural studies in general as well as for the analysis of *ProSAP/Shank* mutant mice, and ASD respectively. Indeed, only a change towards smaller and thinner PSDs in the *Shank1* mutant mouse measured by Hung et al. [56], but there was no ultrastructural alteration in any *ProSAP1/Shank2* knockout mouse models [98,118], fitting to the aforementioned assumption, that *ProSAP1/Shank2* itself might not be crucial for the shape of the synapse.

4.3 No significant alterations in CA3 PSDs of mossy fibers in DKO mice

In his work, “the histology of the central nervous system”, Santiago Ramón y Cajal declared the CA3 synapses as “mossy fiber” synapses, based on their morphology; “the swellings (of the end-boutons) resembled moss on trees” [37]. These synapses are known to have a strong influence on pattern recognition and information storage as well as the completion, separation and linking of patterns [16,38,91]

Mossy fiber boutons, originating from granule cells of the dentate gyrus of the hippocampus form synaptic junctions with pyramidal cell dendrites of the CA3 region in the stratum radiatum. As the second station of the tricyclic pathway [4], there is a strong divergence with up to 15 boutons rising from a single granule cell. This divergence leads to an enormous potentiation of the transmitted signal [2,4,16,37].

The mossy fibers expand sac-like with an average diameter of about 4-11 μm [2,38] and form up to 37 synaptic contacts at a single mossy fiber bouton [2,26,37]. In this context, the CA3 sub-region is described to be relatively resistant to damage [37,77].

The examination of mossy fiber PSDs of wild-type mice revealed a marked constancy of their shape. While it is already described, that these synapses, and their PSDs respectively, are relatively small [2], an average size of mossy fiber synapses was measured in this thesis with the following appearance: The width of the synaptic cleft of about 19 nm represented the classical size of this parameter in the central nervous system. The mean length of the PSDs yielded 175 nm, while a length over 300 nm was rarely seen. Compared to PSDs in the neighbouring sub-region CA1, mossy fiber PSDs were over 20 % smaller. In addition, the mean PSD thickness was slightly reduced compared to CA1 PSDs. Given, that the mossy fiber bouton forms up 37 synaptic junctions in three-dimensional examinations [26], the two-dimensional ultrastructural investigation in this study detected 10 PSDs per bouton.

Due to their described functions and the observed behavioural phenotype of *ProSAP1/Shank2* and *ProSAP2/Shank3* double knockout mice (Schmeisser et al. unpublished), the analysis of these PSDs has been included in the ultrastructural investigation of *ProSAP1/Shank2* and *ProSAP2/Shank3* double knockout mice. Intriguingly, none of the PSD parameters displayed significant differences, which might be due to the experienced resistance of this brain region and the mossy fibers respectively [37]. The large boutons with their uncountable number of vesicles, as well as their high amount of synapses appear to be neuroprotective within this sub-region. Hereby, it is conceivable, that even a knockout of crucial genes, coding for PSD scaffold proteins, might not be able to morphologically disrupt this essential part of the hippocampal circuit. On the ultrastructural level, the high amount of synapses within this hippocampal sub-region in double knockout mice might presumably be capable to compensate a weakened scaffold to potentially maintain its required efficiency and functionality.

4.4 No observed alterations in the cerebellar molecular layer of DKO mice

Based on the fact, that there is currently no data of synaptic ultrastructure in the cerebellum of *ProSAP/Shank* mutant mice, the molecular layer of the cerebellum was examined considering the locomotive dysfunction within these mice.

In this cortical layer of the cerebellum, the dendrites of Purkinje cells build up spines to form synapses with parallel and climbing fibers. An electron dense material indicates the core of such spherical spine heads of Purkinje cell dendrites, allowing to identify these synapses [70]. These spine heads, either linked to a climbing fiber or a parallel fiber, showed an average width of the synaptic cleft of 20 nm in wild-type mice. Like in all aforementioned brain regions, this value seems to be the usual width of synaptic clefts at asymmetric synapses. The average PSD of synapses on Purkinje cell dendrites had a length of 313 nm and a thickness of 23 nm. In contrast to striatal synapses, which have similar circuit modalities, as in particular the reception of glutamatergic, excitatory input, while being inhibitory on their own, the PSD length of climbing and parallel fiber synapses was 10 % increased, while the PSD thickness was 20 % lower compared to striatal PSDs.

On this account, these data suggest that every type of synapse in each of the various brain regions has its own defined and typical construction, although there are analogous circuit modalities.

Based on the fact that *ProSAP2/Shank3* is absent in the molecular layer of the cerebellum, or to be more precise in the Purkinje cells, a germline double knockout of *ProSAP1/Shank2* and *ProSAP2/Shank3* would potentially mimic a single knockout of *ProSAP1/Shank2* within this layer. Interestingly, the examination of the Purkinje cell PSD parameters, analogous to the other brain regions investigated, showed no significant differences compared to their unaffected wild-type controls. These data imply, that even though there was substantial loss of an essential scaffold protein at the tips of spines, the ultrastructure was not changed. This leads to the assumption, that i.) *ProSAP1/Shank2* is not the crucial protein for the maintenance of the geometry of this type of synapse, and PSD respectively and/ or ii.) there have to be additional, compensatory procedures maintaining a throughout consistent PSD.

Given that the Purkinje cell is the only output system of the cerebellar cortex, this system presumably underlies stricter control to preserve its cerebellar function. Hence, it would be necessary that such irreplaceable pathways, with a high amount of signal processing are pretty resistant to damage in general, or in the case of this study, that they are morphologically resistant even to a knockout of substantial genes.

4.5 No ultrastructural alterations in the granular layer of the cerebellum in DKO mice

The first step of the integration of incoming signals in the cerebellum occurs within the granular layer at mossy fiber swellings [93]. The mossy fibers do not have any direct connection to Purkinje cells, therefore their signals are transmitted indirectly via parallel fibers of granule cells [24]. The mossy fiber axons form protoplasmic islands, described as the glomeruli cerebellares, which are occupying at least one third of the entire granular layer [76,81] and establish up to 400 synapses with granule cells and Golgi cells [120]. Within this study, only the asymmetric connections between mossy fibers and granule cell dendrites have been investigated [75].

Since ProSAP1/Shank2 is generally absent in the granular layer of the cerebellum, this region was of particular interest to analyze synapses with only ProSAP2/Shank3 and Shank1 (but no ProSAP1/Shank2) expression.

Similar to mossy fiber boutons in the CA3 region, the swellings within this sub-region contained many synapses, which were smaller in their shape compared to other brain regions. An average mossy fiber swelling of wild-type mice had 10 synapses in this two-dimensional correlate. In a three-dimensional study, however, Kim et al. counted 40-240 release sites at a single mossy fiber swelling. Additionally, there is a direct correlation between the size of a mossy fiber swelling and its release sites [65].

As a first step, this region was investigated in wild-type animals. With 19 nm, the width of the synaptic cleft is comparable to other brain regions. The PSD parameters of these synapses were comparable to those in the CA3 region. Furthermore, with a PSD length of 140 nm, the ordinary PSD length was 55 % smaller than synapses in the molecular layer of the cerebellum. Interestingly, the PSD thickness had similar outcomes compared to other brain regions, 26 nm, which might again point towards this parameter being responsible for the functionality of a single synapse and that this parameter might be maintained throughout different brain regions. However, only electrophysiological studies could confirm this hypothesis.

Intriguingly, there was not any significant parameter alteration comparing wild-type and double knockout animals. The PSDs of double knockout mice had a similar appearance compared to wild-type PSDs. This might be caused by the morphology of mossy fiber swellings and their surroundings, the glomeruli cerebellares. The high amount of the overall synapses could potentially compensate the loss of one of the essential scaffold proteins, ProSAP2/Shank3. A further mechanism for compensation, might be the fact that there are no glial cells, which separate single synapses from one another, leading to an overlap of signals between neighboring release sites [120]. Additionally, the large number of vesicles, always seen in the swellings, may also contribute to the unaltered appearance of the PSDs in double knockout mice. Like in the hippocampal CA3 region, these aspects might be neuroprotective for this brain region. Due to the fact that only two afferent pathways exist in the cerebellum, the mossy fibers and the climbing fibers, it might be even more important to preserve both of these pathways for the maintenance of differentiated cerebellar functions. Although ProSAP/Shanks are substantial postsynaptic scaffold proteins, both deletions of *ProSAP1/Shank2* and *ProSAP2/Shank3* did not result in alterations of the PSD ultrastructure within the granular layer of the cerebellum in contrast to striatal and hippocampal CA1 synapses. Hence, in addition to the presumed compensational mechanisms, these data suggest, that there might be other, not yet decoded instances, leading to the unchanged ultrastructure of mossy fiber swelling PSDs. At least, one could expect, that a loss of ProSAP2/Shank3 proteins, in a sub-region, which does not contain ProSAP1/Shank2 proteins, leads to a breakdown of the PSD. Indeed, this circumstance did not take place, which might be pointing towards a further aspect, that the effects of a ProSAP1/Shank2 and ProSAP2/Shank3 double knockout in distinct brain regions is dependent on the overall amount of these proteins in the PSD within the various brain regions.

4.6 Conclusions

All these results indicate that a *ProSAP1/Shank2* and *ProSAP2/Shank3* double knockout in mice effects a brain region specific outcome, suggesting a different vulnerability of the PSDs in each brain region. In brain regions with high *ProSAP1/Shank2* and *ProSAP2/Shank3* abundance, such as the striatum, the effect of a double knockout of these proteins appeared to be the most detrimental. In brain regions with lower *ProSAP1/Shank2* and *ProSAP2/Shank3* protein levels, the effect of a double knockout of these proteins seemed to be not as impressive as the previous.

Several ultrastructural hints were observed in DKO animals, possibly explaining the ASD-like phenotype occurring in the examined mouse models. But whether the whole phenotypic appearance is brain region specific or even a sub-region specific effect has to be proven by ether cell-type specific or attenuated adenovirus-mediated sub-region specific knockout mouse models. Such approaches could shed light on knowledge on to which extend the ultrastructure is correlated to the behavioral outcome of the animals.

Referred to the literature, where the geometry of PSDs is usually stated as the ultrastructural expression of the efficiency of a synapse [7], the collected data also allows the conclusion that the geometry has to be considered separately with its two components, PSD length and PSD thickness. In particular, not the PSD itself, but the PSD length instead is supposed to be the expression of the efficiency and the PSD thickness to be the expression of the functionality of a single synapse. With this assumption, it is important to consider both parameters with respect to the corresponding brain region. That indicates that the longer the PSD, the more efficient the synapse and, the thicker the PSD, the more functional it is. Vice versa, the thinner the PSD, the less functional the synapse, potentially loosing the entire synaptic strength. There may be critical values for the PSD length but particularly for the PSD thickness, from that the synapse maintains efficient and functional and finally preserves its synaptic strength. Possibly, the fate of a single synapse is determined by defined critical values for the PSD thickness, and maybe also the PSD length, which generally allow a functional synapse or an efficient one, respectively. In addition, only exceeding these critical values might preserve

synaptic strength at all, while smaller differences within these values could further serve for precise modulation.

Condensed, the detailed characterization of the single types of synapses appears to be crucial for the analysis of synaptic ultrastructure, since only the knowledge of the ultrastructure of unaffected synapses in a distinct brain region allows the interpretation of emerging alterations.

Finally, it always has to be considered, that electron microscopic imaging is a static method, only depicting a snapshot of highly dynamic processes within the central nervous system. It was recently shown by Isshiki et al. 2014 that there was a high turnover of excitatory synapses in multiple ASD mouse models [59]. They have not yet shown, that *ProSAP/Shank* mutant mice exhibit this synaptic turnover as well, but the assumable possibility should be noticed by interpreting the data of this thesis. However, the large amount of measured PSD parameters and the highly significant results surely demonstrated the disturbed synaptic composition on the ultrastructural level, though being a non-dynamic method.

5. Summary

ProSAP/Shanks are considered to be the master organizing proteins of the postsynaptic densities (PSDs) of excitatory glutamatergic synapses in the central nervous system. Autism spectrum disorders (ASD) patient cohort studies revealed that in almost 1% of patients one of the ProSAP/Shank genes was mutated. To assess the consequences of ProSAP/Shank mutations, the PSDs of two different animal models were examined upon its morphology in different brain regions. These animal models include *ProSAP1/Shank2* knockout and *ProSAP1/Shank2-ProSAP2/Shank3* double-knockout mice.

In these mice distinct PSD parameters were analyzed for alterations, as an effect of a loss of such crucial PSD components in this highly organized scaffold. As PSD parameters, the PSD density, width of the synaptic cleft, PSD length, thickness and volume were examined.

Analyses were based on electron microscopic studies of ASD associated brain regions, particularly the dorsomedial and dorsolateral striatum, the hippocampal CA1 and CA3 (Cornu Ammonis 1 and 3) region as well as the molecular and granular layer of the cerebellum.

The most striking results were obtained in the dorsolateral striatum. Within this striatal sub-region the PSD composition was significantly altered in double-knockout mice. While the PSD length was reduced by 24% and the PSD thickness by 13%, the calculated PSD volume was even reduced to 49% of those in WT littermates. In the dorsomedial striatum, as well as in the hippocampal CA1 region a significant change of the PSD length of about 20% was obtained. The other brain regions analyzed, CA3, the cerebellar molecular and granular layer, did not show any significant alteration in neither of the measured PSD parameters in the double-knockout mutants. Furthermore, the ultrastructural analyses in *ProSAP1/Shank2* mutant mice did not reveal any significant morphological changes of the PSD.

Among the examined brain regions within this study, these findings might probably highlight the dorsomedial and dorsolateral striatum as well as the hippocampal CA1 region as key areas considering morphological aspects in autism spectrum disorders caused by *ProSAP/Shank* mutations.

Additionally, this study might possibly upgrade the existing paradigm, that the morphology of the PSD expresses the strength of its synapse. The indicated results point towards the PSD length being the expression of the efficiency and the PSD thickness being the expression of the functionality of a synapse, together reflecting synaptic strength.

This work has been performed to expand the existing knowledge of ultrastructural alterations in *ProSAP/Shank* mutants and to gain more detailed information on brain regions that have not yet been investigated in this focus. Even though, electron microscopic analyses are always snap-reading, static methods and do not include the highly dynamic processes occurring in the central nervous system. However, the large amount of measurements of the PSD parameters certainly provides important information on the disturbances occurring on the ultrastructural level in *ProSAP1/Shank2* and *ProSAP1/Shank2-ProSAP2/Shank3* double-knockout.

6. References

1. Abrahams BS, Geschwind DH: Connecting genes to brain in the autism spectrum disorders. *Arch. Neurol.* 67: 395–399 (2010)
2. Acsády L, Kamondi A, Sík A, Freund T, Buzsáki G: GABAergic cells are the major postsynaptic targets of mossy fibers in the rat hippocampus. *J. Neurosci. Off. J. Soc. Neurosci.* 18: 3386–3403 (1998)
3. Amaral DG, Schumann CM, Nordahl CW: Neuroanatomy of autism. *Trends Neurosci.* 31: 137–145 (2008)
4. Andersen P, Bliss TV, Lomo T, Olsen LI, Skrede KK: Lamellar organization of hippocampal excitatory pathways. *Acta Physiol. Scand.* 76: 4A–5A (1969)
5. Antar LN: Metabotropic Glutamate Receptor Activation Regulates Fragile X Mental Retardation Protein and Fmr1 mRNA Localization Differentially in Dendrites and at Synapses. *J. Neurosci.* 24: 2648–2655 (2004)
6. Arakawa H, Blanchard DC, Arakawa K, Dunlap C, Blanchard RJ: Scent marking behavior as an odorant communication in mice. *Neurosci. Biobehav. Rev.* 32: 1236–1248 (2008)
7. Arellano JI, Benavides-Piccione R, Defelipe J, Yuste R: Ultrastructure of dendritic spines: correlation between synaptic and spine morphologies. *Front. Neurosci.* 1: 131–143 (2007)
8. Auerbach BD, Osterweil EK, Bear MF: Mutations causing syndromic autism define an axis of synaptic pathophysiology. *Nature* 480: 63–68 (2011)
9. Bailey A, Bolton P, Butler L, Le Couteur A, Murphy M, Scott S, Webb T, Rutter M: Prevalence of the fragile X anomaly amongst autistic twins and singletons. *J. Child Psychol. Psychiatry* 34: 673–688 (1993)
10. Banerjee A, Castro J, Sur M: Rett Syndrome: Genes, Synapses, Circuits, and Therapeutics. *Front. Psychiatry* 3: (2012)
11. Baron-Cohen S, Lombardo MV, Auyeung B, Ashwin E, Chakrabarti B, Knickmeyer R: Why Are Autism Spectrum Conditions More Prevalent in Males? *PLoS Biol.* 9: e1001081 (2011)
12. Bear MF, Huber KM, Warren ST: The mGluR theory of fragile X mental retardation. *Trends Neurosci.* 27: 370–377 (2004)

13. Belichenko PV, Wright EE, Belichenko NP, Masliah E, Li HH, Mobley WC, Francke U: Widespread changes in dendritic and axonal morphology in *Mecp2* -mutant mouse models of rett syndrome: Evidence for disruption of neuronal networks. *J. Comp. Neurol.* 514: 240–258 (2009)
14. Beversdorf DQ, Manning SE, Hillier A, Anderson SL, Nordgren RE, Walters SE, Nagaraja HN, Cooley WC, Gaelic SE, Bauman ML: Timing of prenatal stressors and autism. *J. Autism Dev. Disord.* 35: 471–478 (2005)
15. Bhakar AL, Dölen G, Bear MF: The Pathophysiology of Fragile X (and What It Teaches Us about Synapses). *Annu. Rev. Neurosci.* 35: 417–443 (2012)
16. Bischofberger J, Engel D, Frotscher M, Jonas P: Timing and efficacy of transmitter release at mossy fiber synapses in the hippocampal network. *Pflüg. Arch. Eur. J. Physiol.* 453: 361–372 (2006)
17. Blackstad TW, Kjaerheim A: Special axo-dendritic synapses in the hippocampal cortex: electron and light microscopic studies on the layer of mossy fibers. *J. Comp. Neurol.* 117: 133–159 (1961)
18. Böckers TM, Winter C, Smalla KH, Kreutz MR, Bockmann J, Seidenbecher C, Garner CC, Gundelfinger ED: Proline-rich synapse-associated proteins ProSAP1 and ProSAP2 interact with synaptic proteins of the SAPAP/GKAP family. *Biochem. Biophys. Res. Commun.* 264: 247–252 (1999)
19. Böckers TM, Kreutz MR, Winter C, Zuschratter W, Smalla KH, Sanmarti-Vila L, Wex H, Langnaese K, Bockmann J, Garner CC, Gundelfinger ED: Proline-rich synapse-associated protein-1/cortactin binding protein 1 (ProSAP1/CortBP1) is a PDZ-domain protein highly enriched in the postsynaptic density. *J. Neurosci. Off. J. Soc. Neurosci.* 19: 6506–6518 (1999)
20. Böckers TM, Segger-Junius M, Iglaue P, Bockmann J, Gundelfinger ED, Kreutz MR, Richter D, Kindler S, Kreienkamp HJ: Differential expression and dendritic transcript localization of Shank family members: identification of a dendritic targeting element in the 3' untranslated region of Shank1 mRNA. *Mol. Cell. Neurosci.* 26: 182–190 (2004)
21. Boeckers TM: The postsynaptic density. *Cell Tissue Res.* 326: 409–422 (2006)

22. Bonaglia MC, Giorda R, Borgatti R, Felisari G, Gagliardi C, Selicorni A, Zuffardi O: Disruption of the ProSAP2 gene in a t(12;22)(q24.1;q13.3) is associated with the 22q13.3 deletion syndrome. *Am. J. Hum. Genet.* 69: 261–268 (2001)
23. Bourgeron T: A synaptic trek to autism. *Curr. Opin. Neurobiol.* 19: 231–234 (2009)
24. Chan-Palay V: On the identification of the afferent axon terminals in the nucleus lateralis of the cerebellum. An electron microscope study. *Z. Für Anat. Entwicklungsgeschichte* 142: 149–186 (1973)
25. Chen X, Nelson CD, Li X, Winters CA, Azzam R, Sousa AA, Leapman RD, Gainer H, Sheng M, Reese TS: PSD-95 Is Required to Sustain the Molecular Organization of the Postsynaptic Density. *J. Neurosci.* 31: 6329–6338 (2011)
26. Chicurel ME, Harris KM: Three-dimensional analysis of the structure and composition of CA3 branched dendritic spines and their synaptic relationships with mossy fiber boutons in the rat hippocampus. *J. Comp. Neurol.* 325: 169–182 (1992)
27. Colonnier M: Synaptic patterns on different cell types in the different laminae of the cat visual cortex. An electron microscope study. *Brain Res.* 9: 268–287 (1968)
28. Costantini F, D'Amato F: Ultrasonic vocalizations in mice and rats: social contexts and functions. *Acta Zool Sin* 52 : 619–633 (2006)
29. Courchesne E: Abnormal early brain development in autism. *Mol. Psychiatry* 7 Suppl 2: S21–23 (2002)
30. Courchesne E, Carper R, Akshoomoff N: Evidence of brain overgrowth in the first year of life in autism. *JAMA J. Am. Med. Assoc.* 290: 337–344 (2003)
31. Dager SR, Wang L, Friedman SD, Shaw DW, Constantino JN, Artru AA, Dawson G, Csernansky JG: Shape mapping of the hippocampus in young children with autism spectrum disorder. *AJNR Am. J. Neuroradiol.* 28: 672–677 (2007)
32. Dawson G, Munson J, Webb SJ, Nalty T, Abbott R, Toth K: Rate of Head Growth Decelerates and Symptoms Worsen in the Second Year of Life in Autism. *Biol. Psychiatry* 61: 458–464 (2007)

33. Delorme R, Ey E, Toro R, Leboyer M, Gillberg C, Bourgeron T: Progress toward treatments for synaptic defects in autism. *Nat. Med.* 19: 685–694 (2013)
34. Devan BD, Hong NS, McDonald RJ: Parallel associative processing in the dorsal striatum: Segregation of stimulus–response and cognitive control subregions. *Neurobiol. Learn. Mem.* 96: 95–120 (2011)
35. Drenckhahn D, Kugler P: *Nervengewebe. In: Drenckhahn D, Benninghoff A. Anatomie: makroskopische Anatomie, Embryologie und Histologie des Menschen 1, 17. Aufl, S. 170-187, Urban & Schwarzenberg.* (2008)
36. Durand CM, Betancur C, Boeckers TM, Bockmann J, Chaste P, Fauchereau F, Nygren G, Rastam M, Gillberg IC, Anckarsäter H, Sponheim E, Goubran-Botros H, Delorme R, Chabane N, Mouren-Simeoni MC, de Mas P, Bieth E, Rogé B, Héron D, Burglen L, Gillberg C, Leboyer M, Bourgeron T: Mutations in the gene encoding the synaptic scaffolding protein SHANK3 are associated with autism spectrum disorders. *Nat. Genet.* 39: 25–27 (2006)
37. Frotscher M, Jonas P, Sloviter RS: Synapses formed by normal and abnormal hippocampal mossy fibers. *Cell Tissue Res.* 326: 361–367 (2006)
38. Frotscher M, Zhao S, Graber W, Drakew A, Studer D: New ways of looking at synapses. *Histochem. Cell Biol.* 128: 91–96 (2007)
39. Gardener H, Spiegelman D, Buka SL: Prenatal risk factors for autism: comprehensive meta-analysis. *Br. J. Psychiatry* 195: 7–14 (2009)
40. Grabrucker AM, Knight MJ, Proepper C, Bockmann J, Joubert M, Rowan M, Nienhaus GU, Garner CC, Bowie JU, Kreutz MR, Gundelfinger ED, Boeckers TM: Concerted action of zinc and ProSAP/Shank in synaptogenesis and synapse maturation. *EMBO J.* 30: 569–581 (2011)
41. Grabrucker AM, Schmeisser MJ, Schoen M, Boeckers TM: Postsynaptic ProSAP/Shank scaffolds in the cross-hair of synaptopathies. *Trends Cell Biol.* 21: 594–603 (2011)
42. Graveland GA, DiFiglia M: The frequency and distribution of medium-sized neurons with indented nuclei in the primate and rodent neostriatum. *Brain Res.* 327: 307–311 (1985)
43. Gray EG: Axo-somatic and axo-dendritic synapses of the cerebral cortex: an electron microscope study. *J. Anat.* 93: 420–433 (1959)

44. Gray EG: Electron microscopy of synaptic contacts on dendrite spines of the cerebral cortex. *Nature* 183: 1592–1593 (1959)
45. Gray EG: The granule cells, mossy synapses and Purkinje spine synapses of the cerebellum: light and electron microscope observations. *J. Anat.* 95: 345–356 (1961)
46. Gray EG, Guillery RW: A note on the dendritic spine apparatus. *J. Anat.* 97: 389–392 (1963)
47. Grzadzinski R, Huerta M, Lord C: DSM-5 and autism spectrum disorders (ASDs): an opportunity for identifying ASD subtypes. *Mol. Autism* 4: 12 (2013)
48. Guy J, Gan J, Selfridge J, Cobb S, Bird A: Reversal of Neurological Defects in a Mouse Model of Rett Syndrome. *Science* 315: 1143–1147 (2007)
49. Hanley JJ, Bolam JP: Synaptology of the nigrostriatal projection in relation to the compartmental organization of the neostriatum in the rat. *Neuroscience* 81: 353–370 (1997)
50. Harris KM, Jensen FE, Tsao B: Three-dimensional structure of dendritic spines and synapses in rat hippocampus (CA1) at postnatal day 15 and adult ages: implications for the maturation of synaptic physiology and long-term potentiation. *J. Neurosci. Off. J. Soc. Neurosci.* 12: 2685–2705 (1992)
51. Harris KM, Landis DM: Membrane structure at synaptic junctions in area CA1 of the rat hippocampus. *Neuroscience* 19: 857–872 (1986)
52. Harris KM, Stevens JK: Dendritic spines of CA 1 pyramidal cells in the rat hippocampus: serial electron microscopy with reference to their biophysical characteristics. *J. Neurosci. Off. J. Soc. Neurosci.* 9: 2982–2997 (1989)
53. Harris KM, Weinberg RJ: Ultrastructure of Synapses in the Mammalian Brain. *Cold Spring Harb. Perspect. Biol.* 4: a005587–a005587 (2012)
54. Hollander E, Anagnostou E, Chaplin W, Esposito K, Haznedar MM, Licalzi E, Wasserman S, Soorya L, Buchsbaum M: Striatal Volume on Magnetic Resonance Imaging and Repetitive Behaviors in Autism. *Biol. Psychiatry* 58: 226–232 (2005)
55. Huguet G, Ey E, Bourgeron T: The Genetic Landscapes of Autism Spectrum Disorders. *Annu. Rev. Genomics Hum. Genet.* 14: 191–213 (2013)

56. Hung AY, Futai K, Sala C, Valtschanoff JG, Ryu J, Woodworth MA, Kidd FL, Sung CC, Miyakawa T, Bear MF, Weinberg RJ, Sheng M: Smaller Dendritic Spines, Weaker Synaptic Transmission, but Enhanced Spatial Learning in Mice Lacking Shank1. *J. Neurosci.* 28: 1697–1708 (2008)
57. Irwin SA: Dendritic Spine Structural Anomalies in Fragile-X Mental Retardation Syndrome. *Cereb. Cortex* 10: 1038–1044 (2000)
58. Ishizuka N, Weber J, Amaral DG: Organization of intrahippocampal projections originating from CA3 pyramidal cells in the rat. *J. Comp. Neurol.* 295: 580–623 (1990)
59. Isshiki M, Tanaka S, Kuriu T, Tabuchi K, Takumi T, Okabe S: Enhanced synapse remodelling as a common phenotype in mouse models of autism. *Nat. Commun.* 5: 4742 (2014)
60. Itzev D, Lolova I, Lolov S, Usunoff KG: Age-related changes in the synapses of the rat's neostriatum. *Arch. Physiol. Biochem.* 109: 80–89 (2001)
61. Jiang Y, Ehlers MD: Modeling Autism by SHANK Gene Mutations in Mice. *Neuron* 78: 8–27 (2013)
62. Jones EG, Powell TP: Morphological variations in the dendritic spines of the neocortex. *J. Cell Sci.* 5: 509–529 (1969)
63. Kanner L: Autistic disturbances of affective contact. *Acta Paedopsychiatr.* 35: 100–136 (1968)
64. Kasai H, Matsuzaki M, Noguchi J, Yasumatsu N, Nakahara H: Structure-stability-function relationships of dendritic spines. *Trends Neurosci.* 26: 360–368 (2003)
65. Kim H-W, Kim N, Kim KW, Rhyu IJ: Three-Dimensional Imaging of Cerebellar Mossy Fiber Rosettes by Ion-Abrasion Scanning Electron Microscopy. *Microsc. Microanal.* 19: 172–177 (2013)
66. Kishi N, Macklis JD: MECP2 is progressively expressed in post-migratory neurons and is involved in neuronal maturation rather than cell fate decisions. *Mol. Cell. Neurosci.* 27: 306–321 (2004)

67. Kouser M, Speed HE, Dewey CM, Reimers JM, Widman AJ, Gupta N, Liu S, Jaramillo TC, Bangash M, Xiao B, Worley PF, Powell CM: Loss of Predominant Shank3 Isoforms Results in Hippocampus-Dependent Impairments in Behavior and Synaptic Transmission. *J. Neurosci.* 33: 18448–18468 (2013)
68. Kreitzer AC: Physiology and Pharmacology of Striatal Neurons. *Annu. Rev. Neurosci.* 32: 127–147 (2009)
69. Krueger DD, Bear MF: Toward Fulfilling the Promise of Molecular Medicine in Fragile X Syndrome. *Annu. Rev. Med.* 62: 411–429 (2011)
70. Landis DM, Reese TS: Cytoplasmic organization in cerebellar dendritic spines. *J. Cell Biol.* 97: 1169–1178 (1983)
71. Lauvin M-A, Martineau J, Destrieux C, Andersson F, Bonnet-Brilhault F, Gomot M, El-Hage W, Cottier JP: Functional morphological imaging of autism spectrum disorders: Current position and theories proposed. *Diagn. Interv. Imaging* 93: 139–147 (2012)
72. Leblond CS, Heinrich J, Delorme R, Proepper C, Betancur C, Huguet G, Konyukh M, Chaste P, Ey E, Rastam M, Anckarsäter H, Nygren G, Gillberg IC, Melke J, Toro R, Regnault B, Fauchereau F, Mercati O, Lemièrre N, Skuse D, Poot M, Holt R, Monaco AP, Järvelä I, Kantojärvi K, Vanhala R, Curran S, Collier DA, Bolton P, Chiochetti A, Klauck SM, Poustka F, Freitag CM, Waltes R, Kopp M, Duketis E, Bacchelli E, Minopoli F, Ruta L, Battaglia A, Mazzone L, Maestrini E, Sequeira AF, Oliveira B, Vicente A, Oliveira G, Pinto D, Scherer SW, Zelenika D, Delepine M, Lathrop M, Bonneau D, Guinchat V, Devillard F, Assouline B, Mouren MC, Leboyer M, Gillberg C, Boeckers TM, Bourgeron T: Genetic and Functional Analyses of SHANK2 Mutations Suggest a Multiple Hit Model of Autism Spectrum Disorders. *PLoS Genet.* 8: e1002521 (2012)

73. Leblond CS, Nava C, Polge A, Gauthier J, Huguet G, Lumbroso S, Giuliano F, Stordeur C, Depienne C, Mouzat K, Pinto D, Howe J, Lemi re N, Durand CM, Guibert J, Ey E, Toro R, Peyre H, Mathieu A, Amsellem F, Rastam M, Gillberg IC, Rappold GA, Holt R, Monaco AP, Maestrini E, Galan P, Heron D, Jacquette A, Afenjar A, Rastetter A, Brice A, Devillard F, Assouline B, Laffargue F, Lespinasse J, Chiesa J, Rivier F, Bonneau D, Regnault B, Zelenika D, Delepine M, Lathrop M, Sanlaville D, Schluth-Bolard C, Edery P, Perrin L, Tabet AC, Schmeisser MJ, Boeckers TM, Coleman M, Sato D, Szatmari P, Scherer SW, Rouleau GA, Betancur C, Leboyer M, Gillberg C, Delorme R, Bourgeron T: Meta-analysis of SHANK Mutations in Autism Spectrum Disorders: a gradient of severity in cognitive impairments. *PLoS Genet.* 10: e1004580 (2014)
74. Lisman JE, Harris KM: Quantal analysis and synaptic anatomy--integrating two views of hippocampal plasticity. *Trends Neurosci.* 16: 141–147 (1993)
75. Miyazaki M: Electron microscopic study on the synaptic glomeruli of rat cerebellum: quantitative and qualitative analyses using the ethanol-phosphotungstic acid (E-PTA) procedure. *Neuropediatrics* 20: 73–78 (1989)
76. Mugnaini E, Atluri RL, Houk JC: Fine structure of granular layer in turtle cerebellum with emphasis on large glomeruli. *J. Neurophysiol.* 37: 1–29 (1974)
77. Nadler JV, Perry BW, Cotman CW: Intraventricular kainic acid preferentially destroys hippocampal pyramidal cells. *Nature* 271: 676–677 (1978)
78. Naisbitt S, Kim E, Tu JC, Xiao B, Sala C, Valtschanoff J, Weinberg RJ, Worley PF, Sheng M: Shank, a novel family of postsynaptic density proteins that binds to the NMDA receptor/PSD-95/GKAP complex and cortactin. *Neuron* 23: 569–582 (1999)
79. Nusser Z, Lujan R, Laube G, Roberts JD, Molnar E, Somogyi P: Cell type and pathway dependence of synaptic AMPA receptor number and variability in the hippocampus. *Neuron* 21: 545–559 (1998)
80. Palay SL: Synapses in the central nervous system. *J. Biophys. Biochem. Cytol.* 2: 193–202 (1956)
81. Palay SL: The electron microscopy of the glomeruli cerebellosi. In: Cytology of the nervous tissue. *Proc Anat Soc G. B. Irel.* 82–84 (1961)

82. Palay SL, Palade GE: The fine structure of neurons. *J. Biophys. Biochem. Cytol.* 1: 69–88 (1955)
83. Pappas GD, Purpura DP: Fine structure of dendrites in the superficial neocortical neuropil. *Exp. Neurol.* 4: 507–530 (1961)
84. Patterson PH: Immune involvement in schizophrenia and autism: etiology, pathology and animal models. *Behav. Brain Res.* 204: 313–321 (2009)
85. Peça J, Feliciano C, Ting JT, Wang W, Wells MF, Venkatraman TN, Lascola CD, Fu Z, Feng G: Shank3 mutant mice display autistic-like behaviours and striatal dysfunction. *Nature* 472: 437–442 (2011)
86. Peça J, Feng G: Cellular and synaptic network defects in autism. *Curr. Opin. Neurobiol.* 22: 866–872 (2012)
87. Peters A: Golgi, Cajal, and the fine structure of the nervous system. *Brain Res. Rev.* 55: 256–263 (2007)
88. Peters A, Kaiserman-Abramof IR: The small pyramidal neuron of the rat cerebral cortex. The perikaryon, dendrites and spines. *Am. J. Anat.* 127: 321–355 (1970)
89. Phelan K, McDermid HE: The 22q13.3 Deletion Syndrome (Phelan-McDermid Syndrome). *Mol. Syndromol.* 2: 186–201 (2012)
90. Raab M, Boeckers TM, Neuhuber WL: Proline-rich synapse-associated protein-1 and 2 (ProSAP1/Shank2 and ProSAP2/Shank3)—scaffolding proteins are also present in postsynaptic specializations of the peripheral nervous system. *Neuroscience* 171: 421–433 (2010)
91. Ramón y Cajal S: *Histology of the nervous system of man and vertebrates.* Oxford University Press, New York, S. 74-77. (1995)
92. Rosenbluth J: Subsurface cisterns and their relationship to the neuronal plasma membrane. *J. Cell Biol.* 13: 405–421 (1962)
93. Rossi DJ, Alford S, Mugnaini E, Slater NT: Properties of transmission at a giant glutamatergic synapse in cerebellum: the mossy fiber-unipolar brush cell synapse. *J. Neurophysiol.* 74: 24–42 (1995)
94. Roussignol G: Shank Expression Is Sufficient to Induce Functional Dendritic Spine Synapses in Aspinous Neurons. *J. Neurosci.* 25: 3560–3570 (2005)
95. Sala C, Piëch V, Wilson NR, Passafaro M, Liu G, Sheng M: Regulation of dendritic spine morphology and synaptic function by Shank and Homer. *Neuron* 31: 115–130 (2001)

96. Sato D, Lionel AC, Leblond CS, Prasad A, Pinto D, Walker S, O'Connor I, Russell C, Drmic IE, Hamdan FF, Michaud JL, Endris V, Roeth R, Delorme R, Huguet G, Leboyer M, Rastam M, Gillberg C, Lathrop M, Stavropoulos DJ, Anagnostou E, Weksberg R, Fombonne E, Zwaigenbaum L, Fernandez BA, Roberts W, Rappold GA, Marshall CR, Bourgeron T, Szatmari P, Scherer SW: SHANK1 Deletions in Males with Autism Spectrum Disorder. *Am. J. Hum. Genet.* 90: 879–887 (2012)
97. Schikorski T, Stevens CF: Quantitative fine-structural analysis of olfactory cortical synapses. *Proc. Natl. Acad. Sci. U. S. A.* 96: 4107–4112 (1999)
98. Schmeisser MJ, Ey E, Wegener S, Bockmann J, Stempel AV, Kuebler A, Janssen AL, Udvardi PT, Shiban E, Spilker C, Balschun D, Skryabin BV, Dieck St, Smalla KH, Montag D, Leblond CS, Faure P, Torquet N, Le Sourd AM, Toro R, Grabrucker AM, Shoichet SA, Schmitz D, Kreutz MR, Bourgeron T, Gundelfinger ED, Boeckers TM: Autistic-like behaviours and hyperactivity in mice lacking ProSAP1/Shank2. *Nature* 486: 256–260 (2012)
99. Schumann CM, Hamstra J, Goodlin-Jones BL, Lotspeich LJ, Kwon H, Buonocore MH, Lammers CR, Reiss AL, Amaral DG: The amygdala is enlarged in children but not adolescents with autism; the hippocampus is enlarged at all ages. *J. Neurosci. Off. J. Soc. Neurosci.* 24: 6392–6401 (2004)
100. Sharpe NA, Tepper JM: Postnatal development of excitatory synaptic input to the rat neostriatum: an electron microscopic study. *Neuroscience* 84: 1163–1175 (1998)
101. Sheng M, Hoogenraad CC: The Postsynaptic Architecture of Excitatory Synapses: A More Quantitative View. *Annu. Rev. Biochem.* 76: 823–847 (2007)
102. Sheng M, Kim E: The Postsynaptic Organization of Synapses. *Cold Spring Harb. Perspect. Biol.* 3: a005678–a005678 (2011)
103. Sheng M, Kim E: The Shank family of scaffold proteins. *J. Cell Sci.* 113 (Pt 11): 1851–1856 (2000)
104. Silverman JL, Turner SM, Barkan CL, Tolu SS, Saxena R, Hung AY, Sheng M, Crawley JN: Sociability and motor functions in Shank1 mutant mice. *Brain Res.* 1380: 120–137 (2011)

105. Smith CU: Sherrington's legacy: evolution of the synapse concept, 1890s-1990s. *J. Hist. Neurosci.* 5: 43–55 (1996)
106. Südhof TC: Neuroligins and neuexins link synaptic function to cognitive disease. *Nature* 455: 903–911 (2008)
107. Tarrant SB, Routtenberg A: Postsynaptic membrane and spine apparatus: proximity in dendritic spines. *Neurosci. Lett.* 11: 289–294 (1979)
108. Ting JT, Peça J, Feng G: Functional Consequences of Mutations in Postsynaptic Scaffolding Proteins and Relevance to Psychiatric Disorders. *Annu. Rev. Neurosci.* 35: 49–71 (2012)
109. Tuchman R, Rapin I: Epilepsy in autism. *Lancet Neurol.* 1: 352–358 (2002)
110. Vanderlos H: Fine structure of synapses in the cerebral cortex. *Z. Für Zellforsch. Mikrosk. Anat. Vienna Austria 1948* 60: 815–825 (1963)
111. Veenman CL, Reiner A: Ultrastructural morphology of synapses formed by corticostriatal terminals in the avian striatum. *Brain Res.* 707: 1–12 (1996)
112. Verpelli C, Schmeisser MJ, Sala C, Boeckers TM: in *Synaptic Plast.* (Kreutz, M. R. & Sala, C.) 970: 29–61 (Springer Vienna, 2012)
113. Wang X, McCoy PA, Rodriguiz RM, Pan Y, Je HS, Roberts AC, Kim CJ, Berrios J, Colvin JS, Bousquet-Moore D, Lorenzo I, Wu G, Weinberg RJ, Ehlers MD, Philpot BD, Beaudet AL, Wetsel WC, Jiang YH: Synaptic dysfunction and abnormal behaviors in mice lacking major isoforms of Shank3. *Hum. Mol. Genet.* 20: 3093–3108 (2011)
114. Westrum LE, Jones DH, Gray EG, Barron J: Microtubules, dendritic spines and spine apparatuses. *Cell Tissue Res.* 208: 171–181 (1980)
115. Whittaker VP, Gray EG: The synapse: biology and morphology. *Br. Med. Bull.* 18: 223–228 (1962)
116. Wilson CJ, Groves PM, Kitai ST, Linder JC: Three-dimensional structure of dendritic spines in the rat neostriatum. *J. Neurosci. Off. J. Soc. Neurosci.* 3: 383–388 (1983)
117. Wöhr M, Roulet FI, Hung AY, Sheng M, Crawley JN: Communication impairments in mice lacking Shank1: reduced levels of ultrasonic vocalizations and scent marking behavior. *PLoS One* 6: e20631 (2011)

118. Won H, Lee HR, Gee HY, Mah W, Kim JI, Lee J, Ha S, Chung C, Jung ES, Cho YS, Park SG, Lee JS, Lee K, Kim D, Bae YC, Kaang BK, Lee MG, Kim E: Autistic-like social behaviour in Shank2-mutant mice improved by restoring NMDA receptor function. *Nature* 486: 261–265 (2012)
119. Won H, Mah W, Kim E: Autism spectrum disorder causes, mechanisms, and treatments: focus on neuronal synapses. *Front. Mol. Neurosci.* 6: (2013)
120. Xu-Friedman MA, Regehr WG: Ultrastructural contributions to desensitization at cerebellar mossy fiber to granule cell synapses. *J. Neurosci. Off. J. Soc. Neurosci.* 23: 2182–2192 (2003)
121. Yang M, Bozdagi O, Scattoni ML, Wöhr M, Rouillet FI, Katz AM, Abrams DN, Kalikhman D, Simon H, Woldeyohannes L, Zhang JY, Harris MJ, Saxena R, Silverman JL, Buxbaum JD, Crawley JN: Reduced excitatory neurotransmission and mild autism-relevant phenotypes in adolescent Shank3 null mutant mice. *J. Neurosci. Off. J. Soc. Neurosci.* 32: 6525–6541 (2012)
122. Yan QJ, Rammal M, Tranfaglia M, Bauchwitz RP: Suppression of two major Fragile X Syndrome mouse model phenotypes by the mGluR5 antagonist MPEP. *Neuropharmacology* 49: 1053–1066 (2005)
123. Zoghbi HY, Bear MF: Synaptic Dysfunction in Neurodevelopmental Disorders Associated with Autism and Intellectual Disabilities. *Cold Spring Harb. Perspect. Biol.* 4: a009886–a009886 (2012)

7. Acknowledgements

Aus Datenschutzgründen entfernt

Lebenslauf

Aus Datenschutzgründen entfernt